

## Review

## Neutron star equation of state: Quark mean-field (QMF) modeling and applications

A. Li<sup>a,\*</sup>, Z.-Y. Zhu<sup>a,b</sup>, E.-P. Zhou<sup>c</sup>, J.-M. Dong<sup>d</sup>, J.-N. Hu<sup>e,f</sup>, C.-J. Xia<sup>g,h</sup><sup>a</sup> Department of Astronomy, Xiamen University, Xiamen 361005, China<sup>b</sup> Institute for Theoretical Physics, Frankfurt am Main 60438, Germany<sup>c</sup> Max Planck Institute for Gravitational Physics (Albert Einstein Institute), Am Mühlenberg 1, Potsdam-Golm, 14476, Germany<sup>d</sup> Institute of Modern Physics, Chinese Academy of Sciences, Lanzhou 730000, China<sup>e</sup> School of Physics, Nankai University, Tianjin 300071, China<sup>f</sup> Strangeness Nuclear Physics Laboratory, RIKEN Nishina Center, Wako, 351-0198, Japan<sup>g</sup> School of Information Science and Engineering, Zhejiang University Ningbo Institute of Technology, Ningbo 315100, China<sup>h</sup> Advanced Science Research Center, Japan Atomic Energy Research Institute, Tokai, Ibaraki 319-1195, Japan

## ARTICLE INFO

## Article history:

Received 1 April 2020

Received in revised form 3 July 2020

Accepted 6 July 2020

## ABSTRACT

Because of the development of many-body theories of nuclear matter, the long-standing, open problem of the equation of state (EOS) of dense matter may be understood in the near future through the confrontation of theoretical calculations with laboratory measurements of nuclear properties & reactions and increasingly accurate observations in astronomy. In this review, we focus on the following six aspects: 1) providing a survey of the quark mean-field (QMF) model, which consistently describes a nucleon and many-body nucleonic system from a quark potential; 2) applying QMF to both nuclear matter and neutron stars; 3) extending QMF formalism to the description of hypernuclei and hyperon matter, as well as hyperon stars; 4) exploring the hadron-quark phase transition and hybrid stars by combining the QMF model with the quark matter model characterized by the sound speed; 5) constraining interquark interactions through both the gravitational wave signals and electromagnetic signals of binary merger event GW170817; and 6) discussing further opportunities to study dense matter EOS from compact objects, such as neutron star cooling and pulsar glitches.

© 2020 The Authors. Published by Elsevier B.V. This is an open access article under the CC BY license (<http://creativecommons.org/licenses/by/4.0/>).

## 1. Introduction

The equation of state (EOS) of dense stellar matter is a problem for both nuclear physics and relativistic astrophysics and has been greatly promoted by the detection of gravitational waves from the GW170817 binary neutron star (NS) merger event (Abbott et al., 2017d).<sup>1</sup> Multimessenger observations of NS mergers (Abbott et al., 2017e) can provide information for determining the EOS of supranuclear matter (e.g., Abbott et al., 2017b; Baiotti, 2019; Chirenti et al., 2017) and that can possibly constrain the phase diagram of the quantum chromodynamics (QCD) (e.g., Alford et al., 2008; Baym et al., 2018; Paschalidis et al., 2018; Han et al., 2019).

In NSs, nuclear matter is present in beta equilibrium from very low density to several times the saturation density ( $\rho \approx 0.16 \text{ fm}^{-3}$ ) and is extremely neutron-rich (Shapiro and Teukolsky,

1983; Lattimer and Prakash, 2004; Baldo and Burgio, 2012; Graber et al., 2017). One assumes that there is one theoretical model that can correctly explain the nuclear matter data of different physical situations obtained in both laboratory nuclear experiments (e.g., Mohr et al., 2016; Danielewicz et al., 2002; Wang et al., 2012; Angeli and Marinova, 2013; Feliciello and Nage, 2015) and astronomical observations (e.g., Hessels et al., 2006; Demorest et al., 2010; Antoniadis et al., 2013; Fonseca et al., 2016; Arzoumanian et al., 2018; Cromartie et al., 2020; Özel and Freire, 2016; Miller et al., 2019; Riley et al., 2019; Abbott et al., 2019, 2020b). However, this is a demanding task. It not only requires the theoretical models to extrapolate from lower density/temperature/isospin to unknown regions at high density/temperature/isospin (e.g., Prakash et al., 2001; Burgio and Fantina, 2018; Stone et al., 2019) but also depends on the relevant degrees of freedom of the problem, from nucleons to exotic particles (e.g., Weber, 2005; Li et al., 2008a; Gal et al., 2016; Oertel et al., 2017; Tolos and Fabbietti, 2020), even dark matter particles (e.g., Li et al., 2012; Das et al., 2020).

\* Corresponding author.

E-mail address: liang@xmu.edu.cn (A. Li).

<sup>1</sup> arXiv page: <http://blogs.cornell.edu/arxiv/2017/10/16/gw170817/>.

In this paper, we follow a widely used relativistic mean-field (RMF) approach (Nikšić et al., 2011) based on an effective Lagrangian with meson fields mediating strong interactions between quarks, which we call the quark mean-field (QMF) model (Shen and Toki, 2000; Toki et al., 1998). It self-consistently relates the internal quark structure of a nucleon and a hyperon to the RMFs arising in nuclear and hyperonic matter, respectively, and has been employed extensively in the calculations of finite (hyperon-)nuclei and infinite dense matter (Shen and Toki, 2000, 2002; Zhu et al., 2019; Hu et al., 2014a,b; Hu and Shen, 2017; Xing et al., 2016, 2017; Zhu and Li, 2018; Zhu et al., 2018). We focus on the EOS that have been developed so far, testing the QMF predictions concerning the constraints from experiments. We also illustrate the developments of this approach for applications to open questions in the present multiscale multimessenger gravitational wave era of astronomy. Another complementary approach for nuclear matter is the *ab initio* approach, such as the Brueckner theory (e.g., Baldo, 1999; Sharma et al., 2015), the chiral effective field theory (e.g., Hebeler et al., 2013; Tews et al., 2019), the quantum Monte Carlo method (e.g., Lonardonì et al., 2015; Gandolfi et al., 2020), and the variational method (e.g., Akmal et al., 1998), which starts from microscopic nucleon-nucleon potentials explicitly including many-body forces. As a comparison, we include some results based on these *ab initio* many-body approaches.

The paper is organized as follows. In Sec. 2, we introduce QMF models by introducing the confinement potential of the constituent quarks for a nucleon. Sec. 3 is then devoted to the NS properties based on the QMF EOSs. In Sec. 4, we demonstrate how strange baryons, e.g., hyperons, are incorporated in the QMF model and discuss the hyperon puzzle with the obtained hyperon star maximum mass. We also discuss hybrid stars and strange quark stars (QSs) by introducing quark matter models. This is followed by the discussions of the NS binary in Sec. 5. Other opportunities for studying EOS are given in Sec. 6, including NS cooling and pulsar glitches. Sec. 7 contains the main conclusions and future perspectives of this review.

## 2. EOS models from the quark level within QMF

In 1988, Guichon (Guichon, 1988) developed a novel model for nuclear matter to treat the changes in the nucleon properties of nuclear matter, i.e., the European Muon Collaboration (EMC) effects. This model is similar to the RMF model, but the scalar and the vector meson fields couple not with the nucleons but directly with the quarks. Then, the nucleon properties change according to the strengths of the mean fields acting on the quarks, and the nucleon is dealt with in terms of the MIT bag model (Degrand et al., 1975). The Guichon model was extended by Thomas and his collaborators under the name of the quark-meson coupling (QMC) model. Excellent reviews on the QMC model can be found in the literature (Guichon et al., 2018; Saito et al., 2007); see also, e.g., (Bohr et al., 2016; Stone et al., 2016; Motta et al., 2019, 2020) for some of the latest improvements. Taking an alternative model for the nucleon, the quark potential model (Isgur and Karl, 1978), Toki and his collaborators constructed the QMF model (Toki et al., 1998). For a more detailed comparison of these two models, we refer to (Shen and Toki, 2000; Zhu et al., 2019). Briefly, the bag model assumes the nucleon is constituted by bare quarks in the perturbative vacuum, i.e., current quarks, with a bag constant to account for the energy difference between the perturbative vacuum and the nonperturbative vacuum, while in the potential model, the nucleon is described in terms of the constituent quarks, which couple with the mesons and gluons. We shall first introduce the potential model and then introduce the QMF formalism.

### 2.1. Quark potential model

In the MIT bag model, the quarks inside the nucleon are confined by a bag, which ensures that the quarks can only move freely and independently inside the nucleon through an infinite potential well. In the potential model, quarks are confined by a phenomenological confinement potential, where the polynomial forms are widely used. A harmonic oscillator potential is usually adopted, with which the Dirac equation can be solved analytically,

$$U(r) = \frac{1}{2}(1 + \gamma^0)(ar^2 + V_0), \quad (1)$$

where the scalar-vector form of the Dirac structure is chosen for the quark confinement potential and the parameters  $a$  and  $V_0$  are determined from the vacuum nucleon properties. When the effect of the nuclear medium is considered, the quark field  $\psi_q(\vec{r})$  satisfies the following Dirac equation:

$$[\gamma^0(\epsilon_q - g_{\omega q}\omega - \tau_{3q}g_{\rho q}\rho - \vec{\gamma} \cdot \vec{p} - (m_q - g_{\sigma q}\sigma) - U(r)]\psi_q(\vec{r}) = 0, \quad (2)$$

where  $\sigma$ ,  $\omega$ , and  $\rho$  are the classic meson fields.  $g_{\sigma q}$ ,  $g_{\omega q}$ , and  $g_{\rho q}$  are the coupling constants of  $\sigma$ ,  $\omega$  and  $\rho$  mesons with quarks, respectively.  $\tau_{3q}$  is the third component of the isospin matrix, and  $m_q$  is the constituent quark mass at approximately 300 MeV. The nucleon mass in the nuclear medium can be expressed as the binding energy of three quarks, defined by the zeroth-order term after solving the Dirac equation  $E_N^0 = \sum_q \epsilon_q^*$ . The quarks are simply confined in a two-body confinement potential. Three corrections are taken into account in the zeroth-order nucleon mass in the nuclear medium, including the contribution of the center-of-mass (c.m.) correction  $\epsilon_{c.m.}$ , pionic correction  $\delta M_N^\pi$  and gluonic correction  $(\Delta E_N)_g$ . The pion correction is generated by the chiral symmetry of QCD theory and the gluon correction by the short-range exchange interaction of quarks. Finally, the mass of the nucleon in the nuclear medium becomes

$$M_N^* = E_N^0 - \epsilon_{c.m.} + \delta M_N^\pi + (\Delta E_N)_g. \quad (3)$$

The nucleon radius is written as

$$\langle r_N^2 \rangle = \frac{11\epsilon'_q + m'_q}{(3\epsilon'_q + m'_q)(\epsilon_q'^2 - m_q'^2)}, \quad (4)$$

where  $\epsilon'_q = \epsilon_q^* - V_0/2$ ,  $m'_q = m_q^* + V_0/2$ . The effective single quark energy is given by  $\epsilon_q^* = \epsilon_q - g_{\omega q}\omega - \tau_{3q}g_{\rho q}\rho$ , and the effective quark mass is given by  $m_q^* = m_q - g_{\sigma q}\sigma$ . By reproducing the nucleon mass and radius  $(M_N, r_N)$  in free space, we determine the potential parameters ( $a$  and  $V_0$ ) in Eq. (1). We obtain  $V_0 = -62.257187$  MeV and  $a = 0.534296$  fm<sup>-3</sup> with  $m_q = 300$  MeV by fitting  $M_N = 939$  MeV and  $r_N = 0.87$  fm (Mohr et al., 2016).

### 2.2. Nuclear matter from an RMF Lagrangian

In the above section, we construct the nucleon at the quark level with the confinement potential and the pion and gluon corrections. Next, we would like to connect such nucleons in a nuclear medium with nuclear objects, such as nuclear matter and systems of finite nuclei. A good bridge is the RMF model at the hadron level, which is developed based on the one-boson exchange potential between two nucleons. The effective nucleon mass from the quark model is inserted into the RMF Lagrangian. The nucleon and meson fields are solved self-consistently, and then, the properties of the nuclear many-body system are obtained. We mention here

that the nucleons are treated as point-like particles even though a quark model is used to describe the structure of the nucleon. In many-body calculations, the structure of the nucleon only modifies the effective mass of a nucleon, i.e., Eq. (3).

We consider the  $\sigma$ ,  $\omega$  and  $\rho$  mesons exchanging in the Lagrangian (Zhu et al., 2018, 2019; Zhu and Li, 2018), and the cross-coupling from the  $\omega$  meson and  $\rho$  meson is introduced to achieve a reasonable slope of symmetry energy (see Sec. 2.3) (Horowitz and Piekarewicz, 2001),

$$\begin{aligned} \mathcal{L} = & \bar{\psi} \left( i\gamma_\mu \partial^\mu - M_N^* - g_{\omega N} \omega \gamma^0 - g_{\rho N} \rho \tau_3 \gamma^0 \right) \psi \\ & - \frac{1}{2} (\nabla \sigma)^2 - \frac{1}{2} m_\sigma^2 \sigma^2 - \frac{1}{3} g_2 \sigma^3 - \frac{1}{4} g_3 \sigma^4 \\ & + \frac{1}{2} (\nabla \rho)^2 + \frac{1}{2} m_\rho^2 \rho^2 + \frac{1}{2} g_{\rho N}^2 \rho^2 \Lambda_v g_{\omega N}^2 \omega^2 \\ & + \frac{1}{2} (\nabla \omega)^2 + \frac{1}{2} m_\omega^2 \omega^2, \end{aligned} \quad (5)$$

where  $g_{\omega N}$  and  $g_{\rho N}$  are the nucleon coupling constants for  $\omega$  and  $\rho$  mesons. From the simple quark counting rule, we obtain  $g_{\omega N} = 3g_{\omega q}$  and  $g_{\rho N} = g_{\rho q}$ . The calculation of the confined quarks gives the relation of the effective nucleon mass  $M_N^*$  as a function of the  $\sigma$  field,  $g_{\sigma N} = -\partial M_N^*/\partial \sigma$ , which defines the  $\sigma$  coupling with nucleons (depending on the parameter  $g_{\sigma q}$ ).  $m_\sigma = 510$  MeV,  $m_\omega = 783$  MeV, and  $m_\rho = 770$  MeV are the meson masses. In this Lagrangian, we already consider the static approximation on the mesons so that their time components are neglected. The spatial part of the  $\omega$  meson disappears for the time reversal symmetry. The infinite nuclear matter has translational invariance, which further removes the partial part of the coordinate space.

The equations of motion of nucleons and mesons can be generated by the Euler-Lagrangian equation from the Lagrangian,

$$(i\gamma^\mu \partial_\mu - M_N^* - g_{\omega N} \omega \gamma^0 - g_{\rho N} \rho \tau_3 \gamma^0) \psi = 0, \quad (6)$$

$$m_\sigma^2 \sigma + g_2 \sigma^2 + g_3 \sigma^3 = -\frac{\partial M_N^*}{\partial \sigma} \langle \bar{\psi} \psi \rangle, \quad (7)$$

$$m_\omega^2 \omega + \Lambda_v g_{\omega N}^2 g_{\rho N}^2 \omega \rho^2 = g_{\omega N} \langle \bar{\psi} \gamma^0 \psi \rangle, \quad (8)$$

$$m_\rho^2 \rho + \Lambda_v g_{\rho N}^2 g_{\omega N}^2 \rho \omega^2 = g_{\rho N} \langle \bar{\psi} \tau_3 \gamma^0 \psi \rangle, \quad (9)$$

where

$$\rho_S = \langle \bar{\psi} \psi \rangle = \frac{1}{\pi^2} \sum_{i=n,p} \int_0^{k_F^i} dp p_i^2 \frac{M_N^*}{\sqrt{M_N^{*2} + p_i^2}}, \quad (10)$$

$$E_F^i = \sqrt{M_N^{*2} + (p_F^i)^2}, \quad (11)$$

$$m_\omega^{*2} = m_\omega^2 + \Lambda_v g_{\omega N}^2 g_{\rho N}^2 \rho^2, \quad m_\rho^{*2} = m_\rho^2 + \Lambda_v g_{\rho N}^2 g_{\omega N}^2 \omega^2. \quad (12)$$

$p_F^n$  ( $p_F^p$ ) is the Fermi momentum for a neutron (proton),  $\rho = \langle \bar{\psi} \gamma^0 \psi \rangle = \rho_p + \rho_n$ , and  $\rho_3 = \langle \bar{\psi} \tau_3 \gamma^0 \psi \rangle = \rho_p - \rho_n$ , which equals 0 in symmetric nuclear matter. Then, the energy density and pressure, with arbitrary isospin asymmetry  $\beta = (\rho_n - \rho_p)/\rho$ , can be generated by the energy-momentum tensor,

$$\begin{aligned} \varepsilon = & \frac{1}{\pi^2} \sum_{i=n,p} \int_0^{k_F^i} \sqrt{k^2 + M_N^{*2}} k^2 dk \\ & + \frac{1}{2} m_\sigma^2 \sigma^2 + \frac{1}{3} g_2 \sigma^3 + \frac{1}{4} g_3 \sigma^4 \\ & + \frac{1}{2} m_\omega^2 \omega^2 + \frac{1}{2} m_\rho^2 \rho^2 + \frac{3}{2} \Lambda_v g_{\rho N}^2 g_{\omega N}^2 \rho^2 \omega^2, \end{aligned} \quad (13)$$

$$\begin{aligned} P = & \frac{1}{3\pi^2} \sum_{i=n,p} \int_0^{k_F^i} \frac{k^4}{\sqrt{k^2 + M_N^{*2}}} dk \\ & - \frac{1}{2} m_\sigma^2 \sigma^2 - \frac{1}{3} g_2 \sigma^3 - \frac{1}{4} g_3 \sigma^4 \\ & + \frac{1}{2} m_\omega^2 \omega^2 + \frac{1}{2} m_\rho^2 \rho^2 + \frac{1}{2} \Lambda_v g_{\rho N}^2 g_{\omega N}^2 \rho^2 \omega^2, \end{aligned} \quad (14)$$

where we have written the meson field with their mean-field values denoted by  $\sigma$ ,  $\omega$ , and  $\rho$ .

### 2.3. Symmetry energy

We subtract the nucleon mass from the energy density (Eq. (13)) to study the binding energy per nucleon,  $E/A = \varepsilon/\rho - M_N$ . The parabolic approximation is usually applicable, and the energy per nucleon can be written as

$$E/A(\rho, \beta) = E/A(\rho, \beta = 0) + E_{\text{sym}}(\rho) \beta^2 + \dots \quad (15)$$

and it is sufficient for performing the calculations only for symmetric nuclear matter and pure neutron matter.  $E/A(\rho, \beta = 0)$  can be expanded around the saturation density,

$$E/A(\rho, 0) = E/A(\rho_0) + \frac{1}{18} K \frac{\rho - \rho_0}{\rho_0} + \dots \quad (16)$$

where  $K$  is the incompressibility at the saturation point. The symmetry energy  $E_{\text{sym}}(\rho)$  can be expressed in terms of the difference between the energies per particle of pure neutrons ( $\beta = 1$ ) and symmetric ( $\beta = 0$ ) matter,  $E_{\text{sym}}(\rho) \approx E/A(\rho, 1) - E/A(\rho, 0)$ . To characterize its density dependence,  $E_{\text{sym}}(\rho)$  can be expanded around the saturation density  $\rho_0$  as follows:

$$\begin{aligned} E_{\text{sym}}(\rho) = & E_{\text{sym}}(\rho_0) \\ & + \frac{dE_{\text{sym}}}{d\rho}(\rho - \rho_0) + \frac{1}{2} \frac{d^2 E_{\text{sym}}}{d\rho^2}(\rho - \rho_0)^2 + \dots \end{aligned} \quad (17)$$

and the following parameters can be defined, where all have an energy dimension (MeV),

$$E_{\text{sym}} = E_{\text{sym}}(\rho_0), \quad (18)$$

$$L = 3\rho_0 \left( \frac{dE_{\text{sym}}}{d\rho} \right)_{\rho_0}, \quad (19)$$

$$K_{\text{sym}} = 9\rho_0^2 \left( \frac{d^2 E_{\text{sym}}}{d\rho^2} \right)_{\rho_0}. \quad (20)$$

$E_{\text{sym}}(\rho)$  can also be written as

$$E_{\text{sym}}(\rho) = E_{\text{sym}} + \frac{1}{3} L \frac{\rho - \rho_0}{\rho_0} + \frac{1}{18} K_{\text{sym}} \left( \frac{\rho - \rho_0}{\rho_0} \right)^2 + \dots \quad (21)$$

In laboratory experiments, the symmetry energy  $E_{\text{sym}}(\rho)$  can be studied by analyzing the neutron skin (e.g., Tagami et al., 2020), the different isovector nuclear excitations (e.g., Danielewicz and Lee, 2014), and the data on heavy-ion collisions such as isospin diffusion and the isotopic distribution in multifragmentation processes (e.g., Li et al., 2008). The large amount of novel exotic nuclei produced in the laboratory and the development of radioactive ion beams have greatly stimulated new research projects on symmetry energy (Oertel et al., 2017; Li et al., 2014; Baldo and Burgio, 2016; Zhang et al., 2020). We mention here that in the following discussion, we only discuss up to the second expansion terms in both the binding energy (Eq. (15)) and the symmetry energy (Eq. (17)); see, e.g., (Dutra et al., 2012, 2014) for detailed discussions on the higher order terms and the suitability of a nuclear EOS for up to

**Table 1**

Properties of nuclear matter at saturation predicted by the EOSs employed in this study, in a comparison with the empirical ranges. The BCPM EoS, named after the Barcelona-Catania-Paris-Madrid energy density functional (Sharma et al., 2015), is based on the microscopic Brueckner-Hartree-Fock (BHF) theory (Baldo, 1999). The BSk20 and BSk21 EoS belong to the family of Skyrme nuclear effective forces derived by the Brussels-Montreal group (Potekhin et al., 2013). The high-density part of the BSk20 EoS is adjusted to fit the result of the neutron matter APR EOS (Akmal et al., 1998), whereas the high-density part of the BSk21 EoS is adjusted to the result of the BHF calculations using the Argonne v18 potential plus a microscopic nucleonic three-body force. The TM1 EOS is based on a phenomenological nuclear RMF model with the TM1 parameter set (Shen et al., 1998), as well as the GM1 EOS, which uses a different parameter set (Glendenning and Moszkowski, 1991). The number density  $n_0$  is in  $\text{fm}^{-3}$ . The energy per baryon  $E/A$  and the compressibility  $K$ , as well as the symmetry energy  $E_{\text{sym}}$  and its slope  $L$  at saturation, are in MeV. The empirical values are taken from (Wang et al., 2012; Angeli and Marinova, 2013; Oertel et al., 2017; Shlomo et al., 2006).

EoS	$\rho_0$ ( $\text{fm}^{-3}$ )	$E/A$ (MeV)	$K$ (MeV)	$E_{\text{sym}}$ (MeV)	$L$ (MeV)
QMF	0.16	-16.00	240.00	31.00	40.0
BCPM	0.16	-16.00	213.75	31.92	53.0
TM1	0.145	-16.26	281.14	36.89	110.8
BSk20	0.159	-16.08	241.4	30.0	37.4
BSk21	0.158	-16.05	245.8	30.0	46.6
APR	0.16	-16.00	247.3	33.9	53.8
GM1	0.153	-16.32	299.2	32.4	93.9
Empirical	$0.16 \pm 0.01$	$-16.0 \pm 0.1$	$240 \pm 20$	$31.7 \pm 3.2$	$58.7 \pm 28.1$

the high density matter possible in NSs. Some of the latest constraints on higher order terms are also discussed in, e.g., (Malik et al., 2018; Zhang and Li, 2019b,a; Zimmerman et al., 2020).

#### 2.4. Results and discussion

There are six parameters ( $g_{\sigma q}$ ,  $g_{\omega q}$ ,  $g_{\rho q}$ ,  $g_3$ ,  $c_3$ ,  $\Lambda_\nu$ ) in this Lagrangian (Eq. (1)) to be determined by fitting the saturation density  $\rho_0$  and the corresponding values at the saturation point of the binding energy  $E/A$ , the incompressibility  $K$ , the symmetry energy  $E_{\text{sym}}$ , the symmetry energy slope  $L$  and the effective (Landau) mass  $M_N^*$  ( $\approx 0.74M_N$ ). In particular, we use the most preferred values for ( $K$ ,  $E_{\text{sym}}$ ,  $L$ ) as recently suggested by (Oertel et al., 2017; Shlomo et al., 2006), namely,  $K = 240 \pm 20$  MeV,  $E_{\text{sym}} = 31.7 \pm 3.2$  MeV, and  $L = 58.7 \pm 28.1$  MeV. A recent fitting of finite nuclei data in the same model yielded  $K = 328$  MeV (Xing et al., 2016), and we choose this case as well for a comparison. To study the effect of  $r_N$ , we varied this parameter from the intermediate value 0.87 fm (Mohr et al., 2016) by approximately 10% according to our model capability:  $r_N = 0.80, 0.87$ , and 1.00 fm. This covers both of the most recent experimental analyses of the *rms*-radius of the proton charge distribution:  $0.879 \pm 0.009$  fm (Arrington and Sick, 2015) from electron-proton scattering and  $0.8409 \pm 0.0004$  fm (Pohl et al., 2010) from the Lamb shift measurement in muonic hydrogen. For each nucleon radius, we first determine the potential parameters ( $a$  and  $V_0$ ) by reproducing ( $m_N, r_N$ ) and then determine QMF many-body parameters by reproducing the saturation properties of nuclear matter ( $\rho_0, E/A, E_{\text{sym}}, K, L, M_N^*/M_N$ ), which is shown in the first line of Table 1. Six EOS models from other theoretical frameworks are also listed, together with the empirical ranges in the last row.

The binding energy and pressure from the QMF are displayed in Fig. 1 for symmetric nuclear matter and pure neutron matter with different nucleon radii. The EOS results within the QMF fulfill the flow constraints from heavy-ion collisions for both symmetric nuclear matter and pure neutron matter. The nucleon radius has a weak effect on the nuclear matter even at high density.

We address other important aspects before closing this section:

- **Temperature:** The above discussions are only for the zero-temperature case, below  $\sim 1$  MeV for cold NSs, lower than the characteristic nuclear Fermi energy, while dense matter is usually hot in heavy-ion collisions and proto-neutron stars, with a

temperature as high as  $\sim 50$  MeV. Although the matter is expected to cool down on timescales of  $10^{-22} - 10^{-24}$  seconds and 1 – 10 seconds, respectively, the thermal effects cannot be ignored, especially in the study of dynamic processes (e.g., Li and Liu, 2013; Li et al., 2015a). However, for the equilibrium configurations of cold NSs, the EOSs are not affected much by finite temperature. For example, the temperature influence on the maximum mass is very limited, and there is an increase in the NS radius for a fixed amount of gravitational mass (e.g., Li et al., 2010b).

- **Meson-coupling parameters:** The present calculations are structured to be renormalizable to fix the coupling constants and the mass parameters by the empirical properties of nuclear matter at saturation. They can also be determined by fitting the ground-state properties of closed-shell nuclei. In the latter case, a substantial stiff EOS with an extremely high incompressibility is usually obtained,  $\sim 328$  MeV, which is not consistent with recent experimental results (Shlomo et al., 2006) (as seen in Table 1). An alternatively low compressibility usually cannot describe the finite nuclei with a proper spin-orbit coupling.
- **Beyond mean-field:** As a starting point, we choose the mean-field approximation, which should be reasonably good at very high densities (a few times the nuclear matter density). There have been studies that demonstrate that the isoscalar Fock terms could be important for the prediction of NS properties (see, e.g., Zhu et al. (2016) for a study based on relativistic Hartree-Fock theory). In such models, the Lorentz covariant structure is kept in full rigor, which guarantees all well-conserved relativistic symmetries. Additionally, the attractive Fock term introduced in the framework of QMC could effectively decrease the incompressibility at the saturation point (Stone et al., 2007).

### 3. Neutron star

NSs with typical masses  $M \approx 1 - 3 M_\odot$  (where  $M_\odot$  is the mass of the sun,  $M_\odot = 1.99 \times 10^{33}$  g) and radii on the order of  $R \approx 10$  km have many extreme features that are unique in the universe (Shapiro and Teukolsky, 1983; Lattimer and Prakash, 2004; Baldo and Burgio, 2012; Graber et al., 2017) and lie outside the realm of terrestrial laboratories, such as rapid rotation, extremely

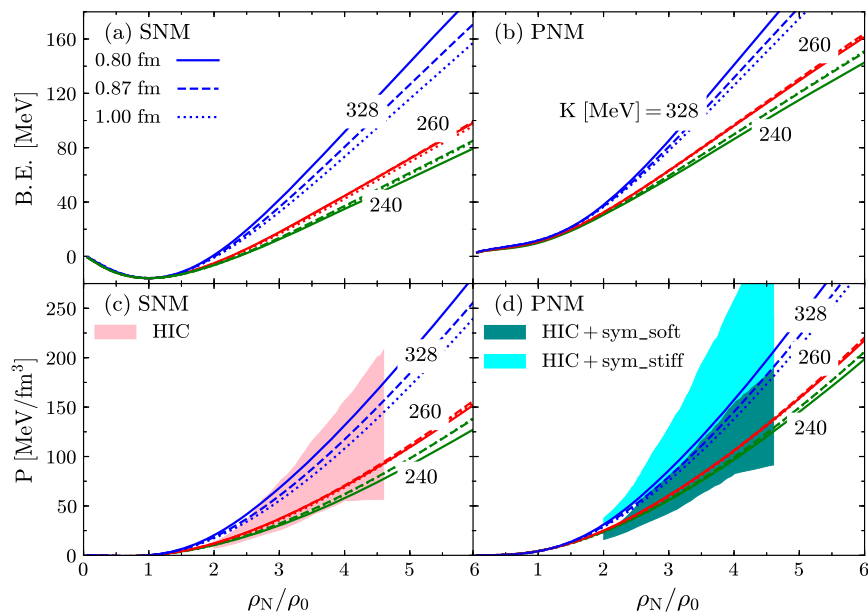


**Fig. 1.** Binding energy (B.E.) and pressure as a function of the number density for symmetric nuclear matter (SNM) and pure neutron matter (PNM). The calculations are performed for fixed symmetry parameters  $E_{\text{sym}} = 31$  and  $L = 60$  MeV and different cases of incompressibility  $K$  at saturation:  $K = 240, 260, 328$  MeV. The results with different nucleon radii of 0.80, 0.87, and 1.00 fm, chosen from the CODATA values and two recent experiments (Mohr et al., 2016; Arrington and Sick, 2015; Pohl et al., 2010), are shown by the solid, dashed, and dotted curves, respectively. Heavy-ion collisions (HIC) are expected to go through a quark–gluon plasma (QGP) phase, where matter is strongly interacting, resulting in the development of collective motion. The EOS results for SNM and PNM lie inside the boundaries obtained from the analysis of the collective flow in HIC (Danielewicz et al., 2002), which are shown with two density-dependent cases of symmetry energy (light blue for the stiff case and dark blue for the soft case). The radius of the nucleon is shown to have limited effects on the nuclear matter EOSs even at high density. Taken from Zhu and Li (2018). (For interpretation of the colors in the figure(s), the reader is referred to the web version of this article.)

strong magnetic fields, superstrong gravitation, interior superfluidity and superconductivity, and superprecise spin period. These intriguing features have aroused much interest from researchers of many branches of contemporary physics as well as astronomy because of their importance to fundamental physics. However, information regarding the NS interior has not yet been sufficiently revealed through the current observations due to the complexity of the NS system and many uncertain factors (Lattimer and Prakash, 2007). It is time to combine the efforts from different communities and discuss mutual interests and problems. In this section, we introduce the basic insights into NSs, in particular the global properties such as the mass, radius, and tidal deformability of the star, which have a one-to-one correspondence to its underlying EOS and are usually used as a tool to connect nuclear physics to astrophysics for the study of dense matter above the nuclear saturation density (e.g., Zhu et al., 2018; Zimmerman et al., 2020; Motta et al., 2019; Lattimer, 2012; Bauswein et al., 2017; Annala et al., 2018; Lim and Holt, 2018; Most et al., 2018; Nandi and Char, 2018; Zhao and Lattimer, 2018; Zhou et al., 2018b; Han and Steiner, 2019; Raithel et al., 2018; Tsang et al., 2019; Wang et al., 2019; Zhou and Chen, 2019; Essick et al., 2020; Ferreira et al., 2020; Güven et al., 2020; Lourenço et al., 2020a,b; Traversi et al., 2020).

A wide range of matter density from  $\sim 0.1 \text{ g cm}^{-3}$  in the star atmosphere to values larger than  $\sim 10^{14} \text{ g cm}^{-3}$  in the star core is encountered in these objects. Theoretically, the global properties are studied by using the overall EOSs as basic input and ignoring their thin atmosphere ( $\sim 0.1 - 10$ ) cm, where hot X-rays originate. The observations of massive NSs (Demorest et al., 2010; Antoniadis et al., 2013; Fonseca et al., 2016; Arzoumanian et al., 2018; Cromartie et al., 2020) have already ruled out soft EOSs that cannot reach  $2M_{\odot}$ . Here, this serves as a criterion for the selection of the NS (core) EOSs. The saturation properties of the employed core EOSs are collected in Table 1, with the empirical ranges listed in the last row. The determination of the EOS above the saturation density represents one of the main problems in NS study because

first principle QCD calculations are difficult to perform in such a many-body system. In most of the model calculations available in the literature, a central density as high as  $(2 - 10)\rho_0$  is found for the maximum mass, and one or more types of strangeness-driven phase transitions (hyperons, kaons, Delta isobars or quarks) may take place in the NSs' innermost parts, e.g., (Hu et al., 2014b; Li et al., 2006, 2007, 2008b, 2009, 2010b, 2015b; Zhu et al., 2016; Burgio et al., 2011; Zuo et al., 2004; Peng et al., 2008). NSs with exotic phases are discussed in Sec. 4. In this section, we restrict ourselves to normal nuclear matter.

### 3.1. Neutron star crust

In the outer crust, at densities below  $\sim 10^7 \text{ g cm}^{-3}$ , nuclei arrange themselves in a Coulomb lattice mainly populated by  $^{56}\text{Fe}$  nuclei. At higher densities ( $10^7 \text{ g cm}^{-3} - 4 \times 10^{11} \text{ g cm}^{-3}$ ), the nuclei are stabilized against beta decay by the filled Fermi sea of electrons and become increasingly neutron-rich. The composition of the outer crust is mainly determined by the nuclear masses, which are experimentally measured close to stability, whereas the masses of the very neutron-rich nuclei are not known, and they have to be calculated using nuclear models.

The inner crust is a nonuniform system of more exotic neutron-rich nuclei, degenerate electrons, and superfluid neutrons. The density range extends from  $\sim 4 \times 10^{11} \text{ g cm}^{-3}$  to the nuclear saturation density  $2.8 \times 10^{14} \text{ g cm}^{-3}$ , at which point the nuclei begin to dissolve and merge together. Nonspherical nuclear structures, generically known as nuclear “pasta”, may appear at the bottom layers of the inner crust. In fact, one of NSs' irregular behaviors, the *glitch*, is closely related to the inner crust EOS and the crust-core transition properties (e.g., Chamel and Haensel, 2008; Piekarewicz et al., 2014; Li, 2015; Li et al., 2016a). The crust is also crucial for NS cooling (Chamel and Haensel, 2008).

It may be necessary to calculate all EOS segments (outer crust, inner crust, and liquid core) using the same nuclear interaction, the so-called “unified” EOS (e.g., Fantina et al., 2013; Potekhin et

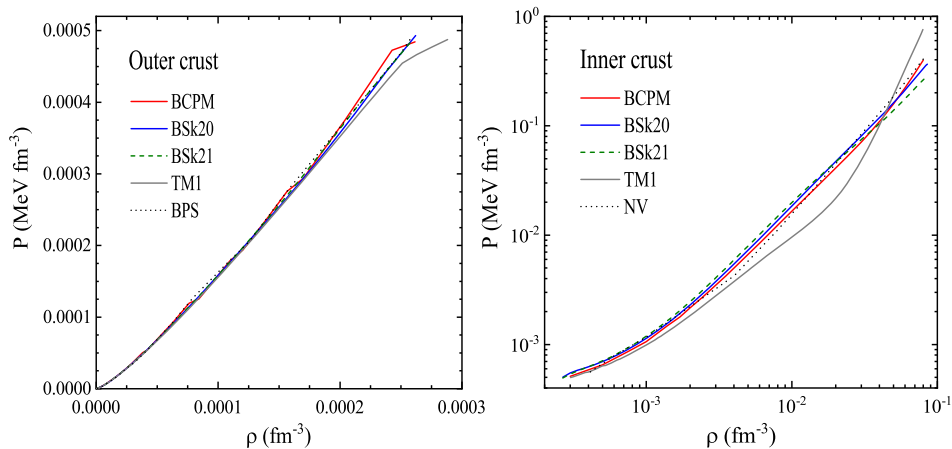


**Fig. 2.** Various EOSs for the outer crust (left) and inner crust (right). Among them, BCPM, TM1, BSk20, and BSk21 are unified NS EOSs, namely, all EOS segments (outer crust, inner crust, liquid core) are calculated using the same nuclear interaction. The BPS (NV) EOS for the outer (inner) crust part is indicated by the black dotted line. The BPS outer crust EOS is based on a semi-empirical mass formula for matter from  $10^7 \text{ g cm}^{-3}$  to  $3.4 \times 10^{11} \text{ g cm}^{-3}$  (Baym et al., 1971), whereas the NV inner crust EOS is based on quantal Hartree-Fock calculations for spherical Wigner-Seitz cells (Negele and Vautherin, 1973).

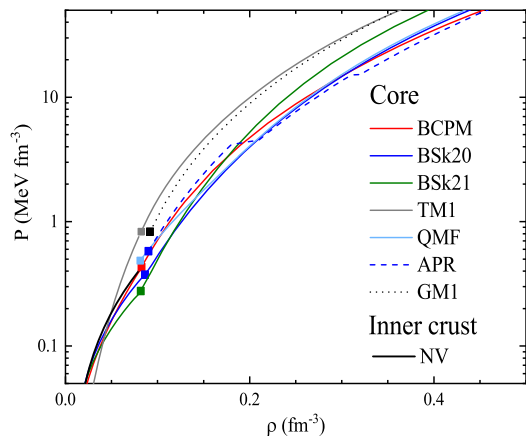


**Fig. 3.** Various EOSs for the NS core from the low-density inner crust indicated with symbols. In addition to the models in Fig. 2, we include another model within the RMF, the GM1 EOS (Glendenning and Moszkowski, 1991), as well as the present QMF model. The inner crust EOS of NV is also included.

al., 2013; Sharma et al., 2015; Antic et al., 2019), since matching problems in nonunified EOS could cause nontrivial conflicts in the predictions of the stars' properties (Fortin et al., 2016). Fig. 2 shows the crust EOS for the different theoretical approaches in Table 1. We observe that all outer crust EOSs display a similar pattern, with some differences around the densities where the composition changes from one nucleus to the next one. Only the TM1 EOS, based on an RMF model, shows a slightly different trend due to the semiclassical-type mass calculations, in which  $A$  and  $Z$  vary in a continuous way, without jumps at the densities associated with a change in the nucleus in the crust.  $A$  is the number of nucleons in the nucleus, and  $Z$  is the atomic number. On the other hand, the energy in the inner crust is largely determined by the properties of the neutron gas; hence, the neutron matter EOS plays an important role. Moreover, the treatment of complicated nuclear shapes, in a range of average baryon densities between the crust and the core, produces some uncertainties in the EOS of the inner crust, where some differences are visible.

In Fig. 3, we show the above discussed EOSs, with the full symbols indicating the transition point from the inner crust to the core for each chosen EOS. The APR, GM1 and QMF EOSs have to be matched with an inner crust EOS, which is at variance with the unified EOSs (BCPM, TM1, BSk20, and BSk21), and we achieve this by imposing that the pressure is an increasing function of the

energy density. It is evident that the matching of the GM1 core (dotted black line) to the TM1 crust (solid gray line) shows non-smooth behavior in the  $dP/d\rho$  slope compared to the matching to the BCPM and NV crust. Since the crust effects were shown to be more important for distorted fast-rotating stars than for static stars (Stergioulas, 2003), later in Sec. 3.4 on rotating NSs, we discuss three widely used crust EOSs (TM1, BCPM, NV + BPS) that are matched with one core EOS (GM1).

Note that the above crust is based on the ground state approximation for zero-temperature matter, which can only be applied to an isolated NS born in a core-collapse supernova explosion. It is assumed that during the process of cooling and crystallization, the plasma maintains nuclear equilibrium. Consequently, when the matter becomes strongly degenerate, the structure and EOS of the crust can be approximated well via cold-catalyzed matter. For an NS crust formed by accreted plasma from the companion star in a low-mass X-ray binary, the outermost layer of the accreted plasma undergoes thermonuclear flashes, observed as X-ray bursts, during the active stages. The layers deeper than a few meters are at  $T < 5 \times 10^8 \text{ K}$ , becoming increasingly neutron-rich due to electron capture and neutrino emissions and finally dissolving in the liquid core. After the fully accreted crust is formed, the layered structure of the crust ceases to evolve and becomes quasistationary, with matter elements moving inwards due to compression and undergoing exothermic nuclear transformations (Fortin et al., 2018). There is a microscopic model for a fully accreted crust (Haensel and Zdunik, 2008) that calculates the EOS and distribution of deep crustal heating sources by following the nuclear evolution of an element of matter consisting initially of X-ray ashes under quasistatic compression from  $10^7 \text{ g cm}^{-3}$  to  $10^{14} \text{ g cm}^{-3}$  (crust-core interface).

### 3.2. Mass-radius relation

To study the structure of NSs, we have to calculate the composition and EOS of cold, neutrino-free, catalyzed matter. We require that the NS contains charge-neutral matter consisting of neutrons, protons, and leptons ( $e^-$ ,  $\mu^-$ ) in beta equilibrium. Additionally, since we are looking at NSs after neutrinos have escaped, we set the neutrino chemical potentials equal to zero. The energy density of NS matter can be written as a function of the different partial densities,

$$\varepsilon(\rho_n, \rho_p, \rho_e, \rho_\mu) = \rho M_N + \rho E(\rho_n, \rho_p) / A$$

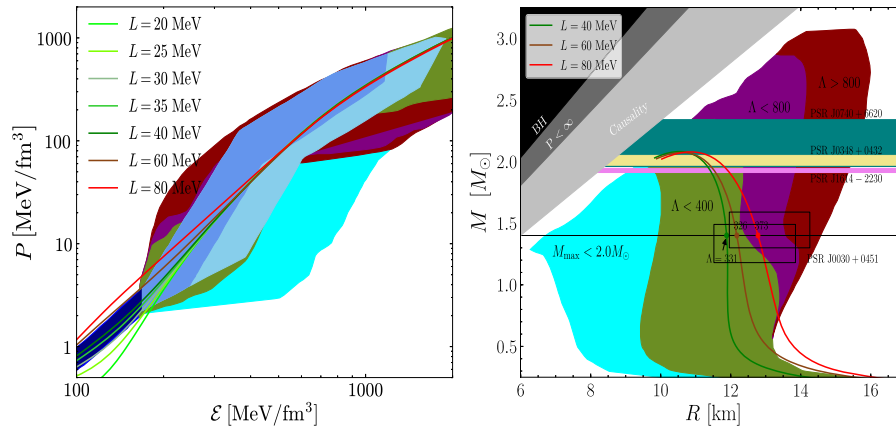


**Fig. 4.** (Left) NS EOSs and (right) mass-radius relation within QMF with different values of symmetry energy slope  $L$ , with more  $L$  cases shown in the left panel than in the right panel. The shaded region is the favored region from *ab initio* calculations at the subsaturation density in chiral effective field theory (Hebeler et al., 2013) and from (Annala et al., 2018). They are causal and fulfill the 2-solar-mass constraint of heavy pulsars ( $M_{\text{TOV}} > 2 M_{\odot}$ ) and the tidal deformability constraint of binary merger event GW170817 ( $\Lambda_{1.4} \leq 800$ ) for a  $1.4 M_{\odot}$  star. Also shown are the latest NICER measurements from the pulse-profile modeling of the accretion hot spots of the isolated millisecond pulsar PSR J0030+0451 (Miller et al., 2019; Riley et al., 2019). The general constraints from the black hole limit, the Buchdahl limit and the causality limit are also included. The figure shows that the radius sensitively depends on the symmetry energy slope with the maximum mass only slightly modified. A smaller  $L$  (softer symmetry energy) leads to a smaller radius. All cases of  $L = 20 - 80$  MeV lie within the  $\Lambda \leq 800$  boundary (Abbott et al., 2017d) and fulfill the updated limit  $\Lambda_{1.4} = 190_{-120}^{+390}$  (Abbott et al., 2018) using the PhenomPNRT waveform model at a 90% confidence level.

$$+\rho_{\mu}m_{\mu} + \frac{1}{2m_{\mu}} \frac{(3\pi^2\rho_{\mu})^{5/3}}{5\pi^2} + \frac{(3\pi^2\rho_e)^{4/3}}{4\pi^2} \quad (22)$$

where we use ultrarelativistic and nonrelativistic approximations for the electrons and muons, respectively, from textbooks (Shapiro and Teukolsky, 1983). Then, the various chemical potentials  $\mu_i$  of the species ( $i = n, p, e, \mu$ ) can be computed,

$$\mu_i = \partial\varepsilon/\partial\rho_i, \quad (23)$$

which fulfills beta-equilibrium,

$$\mu_i = b_i\mu_n - q_i\mu_e \quad (24)$$

( $b_i$  and  $q_i$  denote the baryon number and charge of species  $i$ ). Supplemented with the charge neutrality condition,

$$\sum_i \rho_i q_i = 0 \quad (25)$$

the equilibrium composition  $\rho_i(\rho)$  can be determined at the given baryon density  $\rho$ , and finally, the EOS is

$$P(\rho) = \rho^2 \frac{d(\varepsilon/\rho)}{d\rho} = \rho \frac{d\varepsilon}{d\rho} - \varepsilon = \rho\mu_n - \varepsilon \quad (26)$$

for the interior of NSs.

The NS stable configuration in hydrostatic equilibrium can be obtained by solving the Tolman-Oppenheimer-Volkoff (TOV) equation (Tolman, 1939; Oppenheimer and Volkoff, 1939) for the pressure  $P$  and the enclosed mass  $m$ ,

$$\frac{dP(r)}{dr} = -\frac{Gm(r)\varepsilon(r)}{r^2} \frac{\left[1 + \frac{P(r)}{\varepsilon(r)}\right] \left[1 + \frac{4\pi r^3 P(r)}{m(r)}\right]}{1 - \frac{2Gm(r)}{r}}, \quad (27)$$

$$\frac{dm(r)}{dr} = 4\pi r^2 \varepsilon(r). \quad (28)$$

$G$  is the gravitational constant. Starting with a central mass density  $\varepsilon(r=0) = \varepsilon_c$ , we integrate out until the pressure on the surface equals that corresponding to the density of iron. This gives the stellar radius  $R$ , and the gravitational mass is then

$$m(R) = 4\pi \int_0^R dr r^2 \varepsilon(r) \quad (29)$$

For the description of the NS crust, we usually join the EOS  $P(\varepsilon)$  with the NV EOSs of Negele and Vautherin in the medium-density regime (Negele and Vautherin, 1973) and those of Baym-Pethick-Sutherland for the outer crust (Baym et al., 1971). After solving the TOV equations, we can obtain the maximum mass  $M_{\text{TOV}}$  and the mass-radius relation for comparison with astrophysical observations.

### 3.3. Symmetry energy effects on neutron star structure

Currently, the EOS of SNM ( $\beta = 0$ ) is constrained relatively well. Matter with nonzero isospin asymmetry remains unknown, largely due to the uncertainty in the symmetry energy. Conflicts remain for the symmetry energy (especially its slope) despite significant progress in constraining the symmetry energy around and below the nuclear matter saturation density (Li et al., 2014; Baldo and Burgio, 2016). The symmetry energy slope characterizes the density dependence of the symmetry energy and largely dominates the ambiguity and stiffness of the EOS in NSs' high-density cores in the case of no strangeness phase transition.

Fig. 4 shows our EOSs and the corresponding mass-radius relation under different symmetry energy slopes  $L$  in the range of 20 – 80 MeV. The QMF parameters are fitted to reproduce the saturation properties in Table 1, with the other five parameters ( $\rho_0, E/A, K, E_{\text{sym}}$ ) unchanged (Zhu et al., 2018). The TOV mass of the star hardly changes with changing  $L$  and fulfills the recent observational constraints of three massive pulsars for which the masses are precisely measured (Demorest et al., 2010; Antoniadis et al., 2013; Fonseca et al., 2016; Arzoumanian et al., 2018; Cromartie et al., 2020). There is a strong positive correlation between the slope parameter and the radius of a  $1.4 M_{\odot}$  star (for more discussion, see, e.g., Lim and Holt, 2018; Hornick et al., 2018). However, a small dependence is found in Hornick et al. (2018). The cases of  $L \approx 30 - 60$  MeV in our QMF model may be more compatible with the neutron matter constraint (Hebeler et al., 2013). Capano et al. (2020) found that the radius of a  $1.4 M_{\odot}$  NS is  $R_{1.4} = 11.0_{-0.6}^{+0.9}$  km (90% credible interval), assuming a description in terms of nuclear degrees of freedom remains valid up to  $2\rho_0$ .

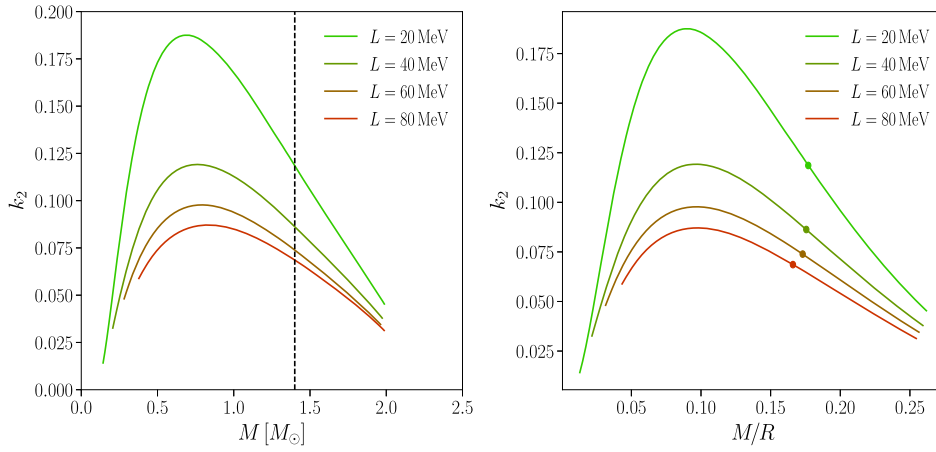


**Fig. 5.** Love numbers as a function of the mass (left) and compactness (right) for four EOSs with different values for the symmetry energy slope  $L$  (20, 40, 60, 80 MeV).  $k_2$  first increases and then decreases with mass and compactness. The increase in  $k_2$  (below  $\sim 1.0 M_\odot$ ) is due to large radii and a large portion of soft crust matter. The vertical line and colorful dots indicate  $M = 1.4 M_\odot$ . Taken from Zhu et al. (2018).

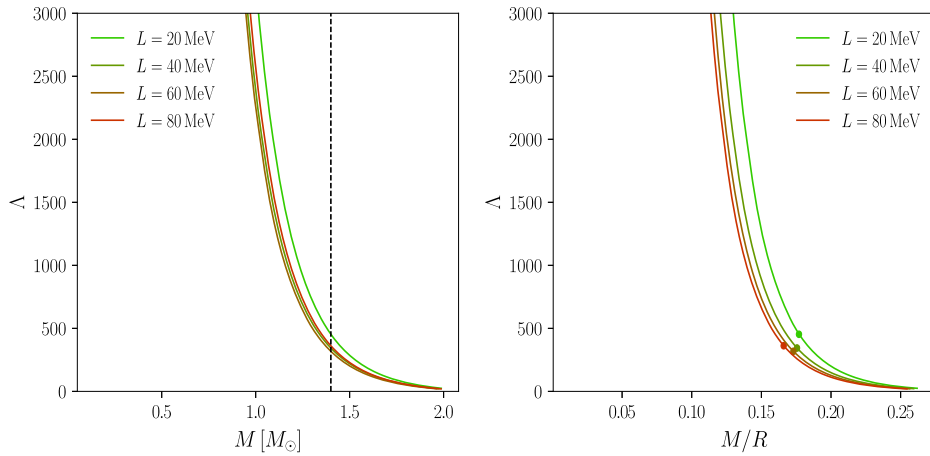


**Fig. 6.** Same as Fig. 5 but for the tidal deformabilities.  $\Lambda$  monotonously decreases with the mass and compactness. Similar to Fig. 5, the large values of  $\Lambda$  for small masses (below  $\sim 1.0 M_\odot$ ) are due to large radii and a large portion of soft crust matter. Taken from Zhu et al. (2018).

The recent NICER measurements of PSR J0030+0451 (Miller et al., 2019; Riley et al., 2019) might indicate  $L \gtrsim 40$  MeV.

The EOS governs not only the stable configuration of a single star but also the dynamics of NS mergers. During the inspiral phase, the influence of the EOS is evident on the tidal polarizability (Postnikov et al., 2010; Read et al., 2013). In Fig. 4, we also include the calculated results of the tidal deformability  $\Lambda$  and the constraining region from binary merger event GW170817, namely,  $\Lambda_{1.4} \leq 800$  for a  $1.4 M_\odot$  star (Abbott et al., 2017d). The tidal deformability describes the magnitude of the induced mass quadrupole moment when reacting to a certain external tidal field. It is zero in the black hole case. The dimensionless tidal deformability  $\Lambda$  is related to the compactness  $M/R$  and the Love number  $k_2$  through  $\Lambda = \frac{2}{3}k_2(M/R)^{-5}$  (see more discussion later in Sec. 5.1).

To study the effects of the symmetry energy slope  $L$  in more detail, we present the resulting Love numbers (tidal deformabilities) as a function of the mass and the compactness for different  $L$  in Fig. 5 (Fig. 6). In Fig. 5,  $k_2$  first increases and then decreases with mass and compactness. In Fig. 6,  $\Lambda$  monotonously decreases with the mass and compactness. The increase in  $k_2$  and large values of  $\Lambda$  for small masses (below  $\sim 1.0 M_\odot$ ) are due to large radii and a large portion of soft crust matter. If no crust is considered (e.g., an EOS described by a pure polytropic function),  $k_2$  still decreases monotonously with mass and compactness. Further loud gravitational-wave measurements from merging binary NSs would

provide data with good precision for learning more about the slope parameter as well as the NS structure. Moreover, the final fate of the merger, i.e., prompt or delayed collapse to a black hole or a single NS star, depends on the EOS, as well as the amount of ejected matter that undergoes nucleosynthesis of heavy elements. These discussions are presented in Sec. 5.

### 3.4. Rotating neutron star

NSs are usually rotating, and the rotational frequency of rapidly rotating NSs (pulsars) could provide restrictions on the EOSs and their evolution processes when combined with the mass constraint. When rapidly rotating, an NS is flattened by the centrifugal force, and the TOV equation, suitable for a static and spherically symmetric situation, cannot correctly describe the rotating stellar structure. We assume NSs are steadily rotating and have an axisymmetric structure. Based on the axial symmetry, the space-time metric used to model a rotating star can be expressed as

$$ds^2 = -e^\nu dt^2 + e^\alpha dr^2 + e^\beta r^2 d\theta^2 + e^\beta r^2 \sin^2 \theta (d\phi - \omega dt)^2, \quad (30)$$

where  $\nu, \alpha, \beta$  and  $\omega$  is the function of  $r, \theta$ . The matter inside the star is approximated by a perfect fluid, and the energy-momentum tensor is given by

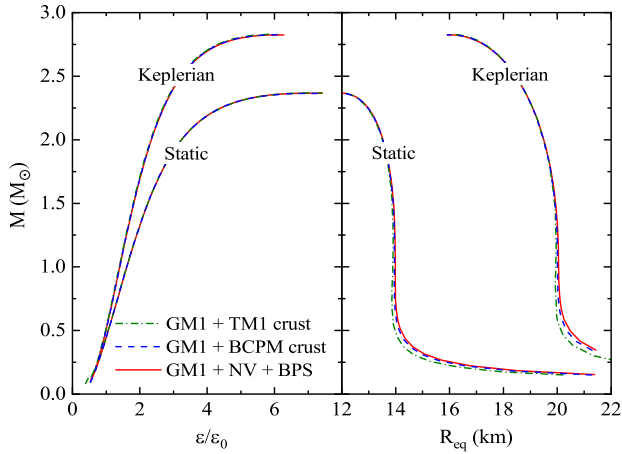


**Fig. 7.** NSs' masses as a function of central energy density (left) and radius (right) for three cases of crust EOSs (TM1, BCPM, NV + BPS) matching one GM1 core EOS, with the detailed EOS matching data shown in Table 1. The calculations are performed for both the static case and Keplerian rotating case. The maximum masses and radii, as well as the central densities, hardly depend on how the inner crusts are described for NSs heavier than  $1.0 M_{\odot}$ .

$$T^{\mu\nu} = (\varepsilon + p)u^{\mu}u^{\nu} - pg^{\mu\nu}, \quad (31)$$

where  $\varepsilon$ ,  $p$  and  $u^{\mu}$  are the energy density, pressure and four-velocity, respectively. To solve Einstein's field equation for potentials  $\nu$ ,  $\alpha$ ,  $\beta$  and  $\omega$ , Komatsu et al. (1989) transformed the Einstein equation from differential equations to integrals by using the Green function method. In this form, the asymptotic flatness condition, which is the boundary condition of the Einstein equation, can be satisfied automatically. This method for solving the Einstein equation is written as a standard code. This is the well-tested RNS code.<sup>2</sup> Using tabulated EOSs, the stationary and equilibrium sequences of rapidly rotating, relativistic stars can then be computed in general relativity (see more detail about the code in, e.g., Komatsu et al., 1989; Cook et al., 1994; Stergioulas and Friedman, 1995).

The Keplerian (mass-shedding) frequency  $f_K$  is one of the most studied physical quantities for rotating stars. An EOS that predicts Kepler frequencies that are smaller than the observed rotational frequencies is to be rejected, as it is not compatible with observation. An empirical formula was proposed in Lattimer and Prakash (2004),

$$f_K = f_0 \left( \frac{M}{M_{\odot}} \right)^{\frac{1}{2}} \left( \frac{R}{10 \text{ km}} \right)^{-\frac{3}{2}}, \quad (32)$$

where  $M$  is the gravitational mass of the Keplerian configuration,  $R$  is the radius of the nonrotating configuration of mass  $M$ , and  $f_0$  is a constant that does not depend on the EOS. An optimal prefactor  $f_0 = 1080$  Hz was found in (Haensel et al., 2009; Wei et al., 2017) for NSs as well as hybrid stars. See more discussion in (Haensel et al., 2009; Wei et al., 2017) regarding the justification of the functional form of Eq. (32) and its valid range. The calculated highest spin frequencies  $f_K$  are all higher than 1000 Hz, while the current observed maximum is  $f = 716$  Hz (Hessels et al., 2006) for PSR J1748-2446a in the globular cluster Terzan 5. A possible reason for this discrepancy is that the star fluid is suffering from  $r$ -mode instability (Andersson and Kokkotas, 2001). A simple estimation showed that this would lower the maximum frequency by  $\sim 37\%$ , which might satisfactorily explain the observations to date.

Fig. 7 shows the crust effects on the star's mass-radius relations in nonunified EOSs, where three widely used crust EOSs (TM1,

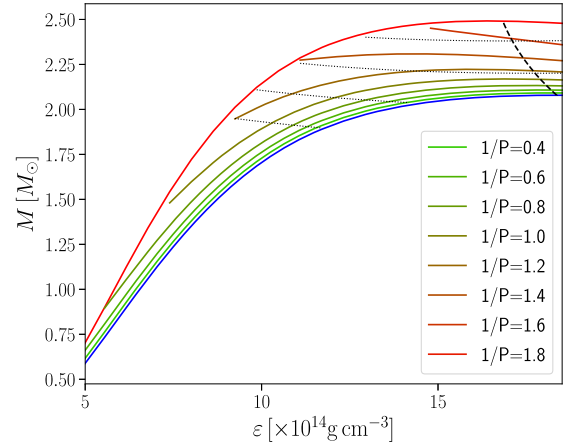


**Fig. 8.** NSs' masses as a function of the central energy density with the QMF EOS at various fixed rotation frequencies  $1/P=0.4-1.8$  kHz. The lower blue curve is the static case, and the upper red curve corresponds to the Keplerian frequencies at different rotating cases. The change in the maximum mass  $M_{\text{crit}}$  with frequency is indicated with a dashed black curve. In static stars, QMF gives  $M_{\text{TOV}} = 2.08 M_{\odot}$  at a central density  $\rho_c = 6.92\rho_0$  with a corresponding radius 10.5 km. At Keplerian frequency  $f_K = 1699$  Hz, the maximum mass and corresponding radius with QMF are  $2.50 M_{\odot}$  and 14.0 km at a central density  $\rho_c = 8.21\rho_0$ . Curves with a fixed baryonic mass of  $M_b = 2.2, 2.4, 2.6, 2.8 M_{\odot}$  are also shown with nearly horizontal gray curves.

BCPM, NV + BPS) are matched with one core EOS (GM1). It is clear that for both the static case and Keplerian rotating case, the results hardly depend on how the inner crusts are described. This is true not only for the maximum mass and central densities but also for the radii. For less massive stars, crust-core matching has a slightly larger effect on the radii, and the TM1 curve deviates slightly from the other two due to the relatively larger difference in the crust-core interface for TM1 mentioned before. This deviation may be relevant only for NSs' masses smaller than  $1.0 M_{\odot}$ .

Generally, rotation increases both the gravitational mass and the radius. Based on the EOSs collected in Table 1, rotation can increase the star's gravitational mass up to  $\sim 18-19\%$ , and the star can be as massive as  $\sim 2.61 M_{\odot}$  in the APR case. Additionally, the star becomes flattened, and the corresponding circumferential radius is increased up to  $\sim 3-4$  km, i.e.,  $\sim 29-36\%$ . For lighter stars such as  $1.4 M_{\odot}$ , the radius increase is more pronounced, reaching  $\sim 5-6$  km, i.e.,  $\sim 41-43\%$ . Additionally, rotation lowers the central density from  $\sim 7-10\rho_0$  to  $\sim 6-9\rho_0$ , which is due to the effect of the centrifugal force, effectively stiffening the EOS. We show in Fig. 8 the gravitational mass as a function of the central density at various fixed rotation frequencies based on the QMF EOS. In static stars, QMF gives  $M_{\text{TOV}} = 2.08 M_{\odot}$  at a central density  $\rho_c = 6.92\rho_0$  with a corresponding radius of 10.5 km. At Keplerian frequency  $f_K = 1699$  Hz and with QMF, the maximum mass is  $2.50 M_{\odot}$  with a corresponding radius of 14.0 km at a central density of  $\rho_c = 8.21\rho_0$ .

One of the most interesting rotating stars is the so-called "supramassive" star, which exists only by virtue of rotation. It is well known that the onset of the instability of the static sequence is determined by the condition  $dM/d\rho_c = 0$ , i.e., the curve should stop at the maximum value of gravitational mass  $M$ . In the rotating case, the above criteria have to be generalized, i.e., a stellar configuration is stable if its mass  $M$  increases with increasing central density for a fixed angular momentum  $J$ . Therefore, the onset of the instability, which is called the secular axisymmetric instability, is expressed by

$$\left( \frac{\partial M}{\partial \rho_c} \right)_J = 0. \quad (33)$$

<sup>2</sup> <http://www.gravity.phys.uwm.edu/rns/>.

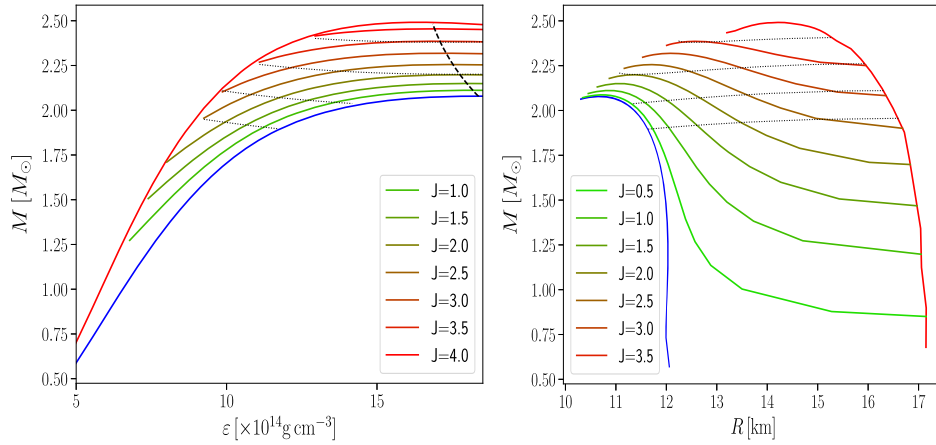


**Fig. 9.** (Left) NS masses as a function of the central energy density and (right) mass-radius relations with the QMF EOS at various fixed angular momenta  $J$ . The lower blue curve is the static case, and the upper red curve corresponds to the Keplerian frequencies in different rotating cases. In the left panel, the change in the maximum mass  $M_{\text{crit}}$  with the angular momentum is indicated with a dashed black curve. A spin-down star, losing angular momentum over its evolution, follows the lines with fixed baryonic mass  $M_b$ , shown by the nearly horizontal gray curves for  $M_b = 2.2, 2.4, 2.6, 2.8 M_\odot$ .

Since rotation increases the mass  $M$  that a star of a given central density can support, the static configuration with the baryon mass  $M_b > M_b^{\text{TOV}}$  (the baryon mass of a TOV mass star) does not exist. Such sequences are supramassive stars that are doomed to collapse as they lose energy and angular momentum during their spin-down, following the nearly horizontal line of fixed baryonic mass  $M_b$ .

We show in Fig. 9 the NS mass as a function of the central energy density as well as the mass-radius relations with the QMF EOS at various fixed angular momenta  $J$ . The lower blue curve is the static case, and the upper red curve corresponds to the Keplerian frequencies in different rotating cases. In the left panel, the change in the maximum mass  $M_{\text{crit}}$  with the angular momentum is indicated with a dashed black curve. There may be a universal relation between  $M_{\text{crit}}/M_{\text{TOV}}$  and  $j/j_K$  (e.g., Breu and Rezzolla, 2016; Urbanec et al., 2013; Yagi and Yunes, 2013a,b; Haskell et al., 2014; Pappas and Apostolatos, 2014) that does not depend on the specific choice of EOS or the  $f_K$  value,

$$\frac{M_{\text{crit}}}{M_{\text{TOV}}} = 1 + a_2 \left(\frac{j}{j_K}\right)^2 + a_4 \left(\frac{j}{j_K}\right)^4 \quad (34)$$

where  $j = J/M^2$  is the dimensionless angular momentum and the coefficients are  $a_2 = 1.316 \times 10^{-1}$  and  $a_4 = 7.111 \times 10^{-2}$  (Breu and Rezzolla, 2016).

Note that the above discussions focus only on the case of rigid rotation, while differential rotation can be much more efficient in increasing the maximum allowed mass. In differentially rotating stars, the high-density inner part may rotate faster than the low-density outer part, so the inner part can be supported by rapid rotation without the equator having to exceed the Keplerian limit (e.g., Zhou et al., 2019). While both rigid and differential rotation follow axisymmetry, there are cases when a rotating NS breaks its axial symmetry if the rotational kinetic energy to gravitational binding energy ratio,  $T/|W|$ , exceeds a critical value. The abovementioned  $r$ -mode instability could also trigger NSs' motion with off-axis symmetry. It is presently unclear whether such configurations of NSs can actually be realized in practice (e.g., Zhou et al., 2018a). Overall, it is especially important to calculate models of rotating stars to better understand the observations of binary merger events (see details in Sec. 5.2).

## 4. EOS with exotic particles

### 4.1. Hyperon star and hyperon puzzle

While around the saturation densities  $\rho = \rho_0$ , the matter inside an NS consists only of nucleons and leptons, at higher densities, several other species of particles may appear due to the fast increase in the baryon chemical potentials with density (e.g., Weber, 2005; Gal et al., 2016; Tolos and Fabbietti, 2020), just because their appearance is able to lower the ground state energy of the dense nuclear matter phase. Among these new particles are strange baryons, namely, the  $\Lambda$ ,  $\Sigma^{0,\pm}$ ,  $\Xi^{0,-}$  hyperons. Other species (such as kaons and Delta isobars) might also appear in stellar matter, which the present paper does not cover. Generally, the presence of one species of strange particle is found to push the onset of other species of strange particles to higher densities, even out of the physically relevant density regime (e.g., Motta et al., 2020; Li et al., 2007).

It is necessary to generalize the QMF study of the nuclear EOS with the inclusion of hyperons (e.g., Shen and Toki, 2002; Hu et al., 2014a,b; Xing et al., 2016, 2017; Hu and Shen, 2017). The density thresholds of hyperons are essentially determined by the masses and their interaction. The mass of  $\Lambda(uds)$  is 1116 MeV. The masses of  $\Sigma^+(uus)$ ,  $\Sigma^0(uds)$ ,  $\Sigma^-(dds)$  are 1189, 1193, and 1197 MeV, respectively. The masses of  $\Xi^0(uss)$  and  $\Xi^-(dss)$  are 1315 and 1321 MeV, respectively. From hypernuclei experiments in the laboratory (Felicciello and Nage, 2015), we know that  $\Lambda$ -nucleus and  $\Lambda\Lambda$  interactions are attractive, while  $\Sigma$ -nucleus interactions are repulsive. Additionally, the nature of the  $\Xi$ -nucleus interaction has been suggested to be attractive (Khaustov et al., 2000). Theoretically, any effective many-body theories should respect the available hypernuclei data before proceeding with other sophisticated studies (Gal et al., 2016; Tolos and Fabbietti, 2020). The adopted hyperon-meson couplings need to at least reproduce unambiguous hypernuclear data.

At the mean-field level, the single  $\Lambda$ ,  $\Sigma$ ,  $\Xi$  potential well depths in symmetric nuclear matter are  $U_{\Lambda,\Sigma,\Xi}^{(N)} \sim -30, 30, -14$  MeV at the saturation density, respectively. In the extended QMF model (Hu et al., 2014a,b), we introduce different confining strengths for the  $s$  quarks and the  $u, d$  quarks in the corresponding Dirac equations (under the influence of the meson mean fields). The confining strength of the  $u, d$  quarks is constrained by finite nuclei properties, and that of the  $s$  quarks is constrained by the well-established empirical value of  $U_{\Lambda}^{(N)} \sim -30$  MeV. The mass difference among baryons is generated by taking into account the

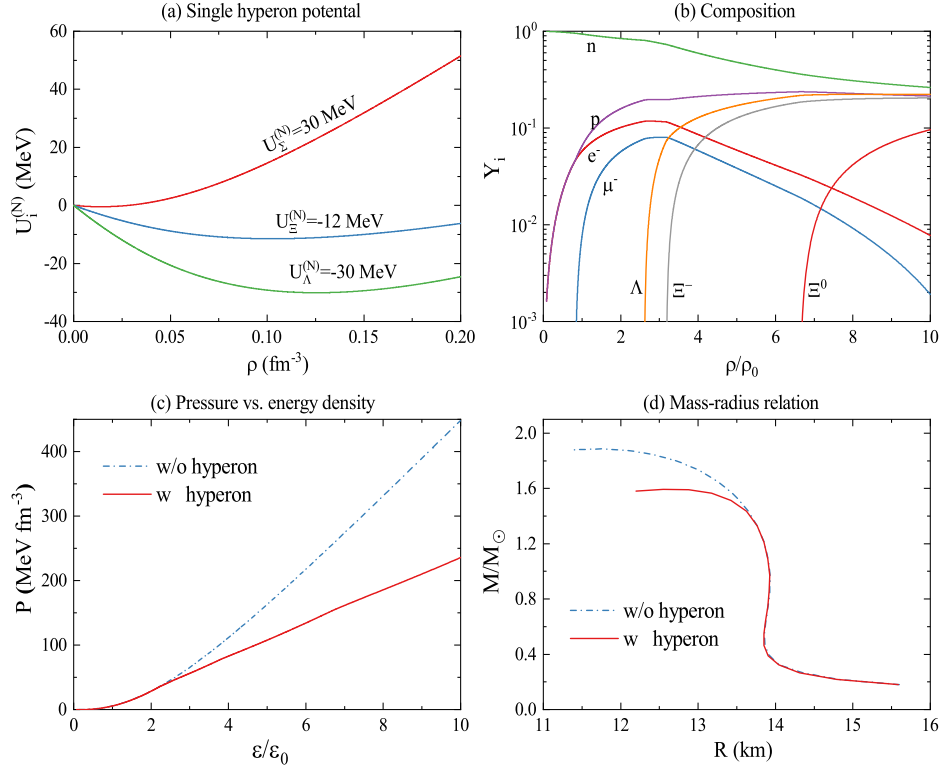


**Fig. 10.** (a) Single hyperon potential, (b) fractions of leptons and baryons, (c) EOS, and (d) mass-radius relations for NSs with hyperons within QMF. The cases without hyperons in the star's core are also shown in the lower panels. The maximum mass of QMF EOS without hyperons is slightly lower than  $2 M_\odot$  due to the absence of a high-order vector coupling term for effective nuclear interaction from an earlier work (Hu et al., 2014b). When hyperons are included, the mass is largely reduced and well below the observational 2-solar-mass limit. The hyperon puzzle is also present in many microscopic studies based on developed realistic baryon-baryon interactions (e.g., Lonardoni et al., 2015; Burgio et al., 2011; Rijken and Schulze, 2016; Bombaci, 2017). Adapted from Hu et al. (2014b).

spin correlations  $E_B^* = \sum_i e_i^* + E_{\text{spin}}^B$ , and the spin correlations of the baryons are fixed by fitting the baryon masses in free space. In addition, the spurious c.m. motion is removed through the usual square root method as  $M_B^* = \sqrt{E_B^{*2} - \langle p_{\text{cm}}^2 \rangle}$ . The contribution of the  $\sigma$  meson is contained in the effective mass  $M_{\Lambda, \Sigma, \Xi}^*$ , and the  $\omega$  and  $\rho$  mesons couple to the baryons with the following coupling constants:

$$g_{\omega N} = 3g_\omega^q, \quad g_{\omega \Lambda} = cg_{\omega \Sigma} = 2g_\omega^q, \quad g_{\omega \Xi} = g_\omega^q \quad (35)$$

$$g_{\rho N} = g_\rho^q, \quad g_{\rho \Lambda} = 0, \quad g_{\rho \Sigma} = 2g_\rho^q, \quad g_{\rho \Xi} = g_\rho^q \quad (36)$$

where a factor  $c$  is introduced before  $g_{\omega \Sigma}$  for a large  $\Sigma\omega$  coupling, in contrast with the  $\Lambda - \omega$  coupling, to simulate the additional repulsion on the  $\Sigma$ -nucleon channel, and  $U_\Sigma^{(N)} = 30$  MeV at the nuclear saturation density. The basic parameters are the quark-meson couplings ( $g_\sigma^q$ ,  $g_\omega^q$ , and  $g_\rho^q$ ), the nonlinear self-coupling constants ( $g_3$  and  $c_3$ ), and the mass of the  $\sigma$  meson ( $m_\sigma$ ) (for more detail regarding the formalism and the parameters, see Shen and Toki, 2000; Hu et al., 2014b). With such a parameter set, the saturation properties of nuclear matter can be described (Hu et al., 2014b). The values of a single  $\Xi$  hyperon in nuclear matter are obtained as  $U_\Xi^{(N)} = -12$  MeV, consistent with the BNL-E885 experiments (Khaustov et al., 2000). The density dependences of the single hyperon ( $\Lambda$ ,  $\Sigma$ ,  $\Xi$ ) potentials are shown in Fig. 10(a).

Regarding the EOS of hyperonic matter, the baryon contributions can be obtained through the mean-field ansatz from the Lagrangian (including hyperons) (Shen and Toki, 2000; Hu et al., 2014b). Electrons are again treated as a free ultrarelativistic gas, whereas the muons are relativistic, as in Eq. (22). The total EOS can be calculated for a given composition of baryon components. This allows the determination of the chemical potentials of all species,

which are the fundamental input for the equations of chemical equilibrium:

$$\mu_n = \mu_\Lambda = \mu_{\Sigma^0} = \mu_{\Xi^0} \quad (37)$$

$$\mu_e = \mu_\mu \quad (38)$$

$$\mu_n - \mu_e = \mu_p = \mu_{\Sigma^+} \quad (39)$$

$$\mu_n + \mu_e = \mu_{\Sigma^-} = \mu_{\Xi^-} \quad (40)$$

The above equations must be supplemented with two other conditions, i.e., charge neutrality and baryon number conservation. These are

$$\rho_p + \rho_{\Sigma^+} = \rho_e + \rho_\mu + \rho_{\Sigma^-} + \rho_{\Xi^-}, \quad (41)$$

$$\rho = \rho_n + \rho_p + \rho_\Lambda + \rho_\Sigma + \rho_{\Sigma^+} + \rho_{\Sigma^-} + \rho_{\Xi^-} + \rho_{\Xi^0}. \quad (42)$$

Finally, the actual detailed fraction  $Y_i = \rho_i(\rho)$  of the dense matter is determined for each fixed baryon density  $\rho$ , as shown in Fig. 10 (b). In the low-density region (until  $\rho < 0.21 \text{ fm}^{-3}$ ), the proton fraction  $\rho_p/\rho$  is well below  $1/9$ , which fulfills the astrophysical observation that direct URCA cooling might not occur at too low densities (Yakovlev et al., 2001). With the properly chosen  $\Lambda$ ,  $\Sigma$  and  $\Xi$  hyperon potentials,  $\Lambda$  is the first hyperon appearing at  $\sim 2 - 3\rho_0$ . Then,  $\Xi^-$  hyperons appear at  $\sim 3\rho_0$  followed by  $\Xi^0$  hyperons at  $\sim 7\rho_0$ . The fractions of hyperons increase with density. At densities above  $\sim 10\rho_0$ , the fractions of  $\Lambda$  and  $\Xi^-$  are almost the same as the fractions of protons and neutrons.  $\Sigma^-$ , however, does not appear until very high density of  $2.0 \text{ fm}^{-3}$ .

In Fig. 10 (c), we show the pressure of beta-equilibrated matter as a function of the energy density. The solid curve represents the EOS including the hyperons, and the dot-dashed curve is the EOS without hyperons. The EOS becomes softer with the presence of

strangeness freedom. The NS properties are calculated by using the EOSs with/without hyperons obtained from the QMF model, and the NS mass-radius relations are plotted in Fig. 10 (d). It is found that the maximum mass of the NSs including hyperons is approximately  $1.6 M_{\odot}$ , much lower than that without hyperons, which is below the observational limit. This is the so-called hyperon puzzle, which is also found in many microscopic studies based on developed realistic baryon-baryon interactions (e.g., Lonardonì et al., 2015; Burgio et al., 2011; Rijken and Schulze, 2016; Bombaci, 2017).

Since hyperons are not present in nuclear matter, they cannot be determined from the nuclear matter properties. Moreover, the analysis of experimental data on hypernuclei shows that we cannot fix these parameters in a unique way. How can a sufficiently stiff high-density EOS generate a heavy hyperon star with properly reproduced nuclear matter properties at the saturation density? There may be three approaches forward:

1. Three-body hyperon interactions can be introduced in microscopic studies or high-order meson fields in effective calculations. If they are repulsive, a stiff enough hyperon star EOS can be obtained by increasing the repulsion as the density increases, and there is a possibility of massive hyperon stars with a central density  $> \sim 5\rho_0$ , (e.g., Stone et al., 2007; Yamamoto et al., 2014; Haidenbauer et al., 2017; Logoteta et al., 2019). This is a natural solution based on the known importance of three-body nucleon forces in nuclear physics;
2. Larger maximum masses can be produced through a transition to another phase of dense (quark) matter in the stellar core at high densities (e.g., Li et al., 2009, 2015b; Peng et al., 2008). This approach is presented in Sec. 4.2;
3. A separate branch of pulsar-like objects can be introduced to account for the heavy ones, for example, QSs made of free quarks (e.g., Li et al., 2010a, 2011; Haensel et al., 1986). Unlike NSs, which are bound by gravity, QSs are bound by strong interactions; therefore, they have opposite M-R dependence. This is the so-called two-branch scenario (e.g., Wiktorowicz et al., 2017; Drago and Pagliara, 2018), which is discussed in Sec. 4.3.

#### 4.2. Strange quark matter and hybrid stars

The matter inside the NS core possesses densities ranging from a few times  $\rho_0$  to one order of magnitude higher. At such densities, the hadronic matter might undergo a phase transition to quark matter, and a hybrid NS with a quark matter or mixed core can be formed. However, the exact value of the transition density to quark matter is unknown and still a matter of recent debate not only in astrophysics but also within the theory of high energy heavy-ion collisions. Additionally, it is not obvious whether the information on the nuclear EOS from high energy heavy-ion collisions can be related to the physics of NS interiors. The possible quark-gluon plasma produced in heavy-ion collisions is expected to be characterized by low baryon density and high temperature, while the possible quark phase in NSs appears at high baryon density and low temperature. Nevertheless, we must be careful that the transition cannot occur at too low of density (below the nuclear saturation density  $\rho_0$ ) to maintain consistency with the current experimental data of heavy-ion collisions.

The possibility of the existence of strange quark matter in NS high-density cores is of special interest in the present era of GW astronomy (e.g., Han et al., 2019; Han and Steiner, 2019; Alford et al., 2019; Aloy et al., 2019; Bauswein et al., 2019; Most et al., 2019; Xia et al., 2019a; Gomes et al., 2019; Chatzioannou and Han, 2020; Fischer et al., 2020; Tonetto and Lugones, 2020; Nunna et al., 2020; Weih et al., 2020). Presently, we have no unified models to address the hadron phase and the quark phase,

and it is still not clear whether the change in the hadron phase corresponding to that in the quark phase is a crossover or a first-order transition. Here, we analyze a specific example in the context of a first-order transition (at transition pressure  $P_{\text{trans}}$ ) to express the experimental constraints in model-independent terms. For the hadronic sector, we use the above QMF model. For the high-density quark phase, we utilize the CSS parametrization (Alford et al., 2013), exploiting the fact that for a considerable class of microscopic quark matter models, the speed of sound is weakly density-dependent, e.g., (Zdunik and Haensel, 2013; Alford et al., 2015; Ranea-Sandoval et al., 2016). The present scheme can only discuss the transition that occurs at a sharp interface (Maxwell construction) between bulk hadronic matter and quark matter, i.e., the quark-hadron surface tension is high enough to disfavor mixed phases (Gibbs construction). It has been shown that a strong first-order phase transition with a sharp interface is the most promising scenario to be tested or distinguished from pure hadronic matter by future observations (e.g., Han et al., 2019; Han and Steiner, 2019; Chatzioannou and Han, 2020; Miao et al., 2020). We tend to find that the observation of a 2-solar-mass star and the accurate measurement of the typical NS radius constrain the CSS parameters, including the squared speed of sound in the high-density phase  $c_{\text{QM}}^2$ , the hadron-quark phase transition density  $\rho_{\text{trans}}$ , and the discontinuity in the energy density at the transition  $\Delta\varepsilon/\varepsilon_{\text{trans}}$ , where  $\rho_{\text{trans}} \equiv \rho_{\text{NM}}(P_{\text{trans}})$ ,  $\varepsilon_{\text{trans}} \equiv \varepsilon_{\text{NM}}(P_{\text{trans}})$ . For a given nuclear matter EOS  $\varepsilon_{\text{NM}}(P)$ , the full CSS EOS is

$$\varepsilon(P) = \begin{cases} \varepsilon_{\text{NM}}(P) & P < P_{\text{trans}} \\ \varepsilon_{\text{NM}}(P_{\text{trans}}) + \Delta\varepsilon + c_{\text{QM}}^{-2}(P - P_{\text{trans}}) & P > P_{\text{trans}} \end{cases}$$

We perform the calculation by varying  $c_{\text{QM}}^2$  from the causality limit ( $c_{\text{QM}}^2 = 1$ ) to the conformal limit ( $c_{\text{QM}}^2 = 1/3$ , the value for systems with conformal symmetry that may be applicable to relativistic quarks). It is worth mentioning that perturbative QCD calculations exhibit quark matter with  $c_{\text{QM}}^2$  values of approximately 0.2 to 0.3 (Kurkela et al., 2010). We use units where  $\hbar = c = 1$ . In Fig. 11, we show representative EOSs  $P(\varepsilon)$  for dense matter with a sharp first-order phase transition and the corresponding mass-radius relations. The 2-solar-mass lower limit for maximum gravitational mass is explicitly indicated in the mass vs. radius plot. We include the curves with increasing transition density from  $1.25\rho_0$  to  $6\rho_0$  at a fixed energy density discontinuity and speed of sound in quark matter, and the nuclear matter EOS is chosen to be the QMF model result with the symmetry energy slope  $L = 60$  MeV. We mention here that  $L \sim 30 - 60$  MeV is the preferred range within QMF as indicated by the *ab initio* calculations (shown in Fig. 4). We see that a lower transition density (pressure), therefore a stiffer EOS, leads to a heavier hybrid star. The smallest hybrid star is typically the heaviest.

Systematically, we carry out calculations for the mass-radius of hybrid stars spanning the whole parameter space of the speed of sound in a domain with a transition density up to  $\rho_{\text{trans}} = 6\rho_0$  and an energy density discontinuity up to  $\Delta\varepsilon = 1.5\varepsilon_{\text{trans}}$ . The calculations are performed using two values for the symmetry energy slope parameter of  $L = 30$  MeV and  $L = 60$  MeV. Fig. 12 displays the correlation of the radius of a  $1.4 M_{\odot}$  hybrid star  $R_{1.4}$  with the transition density  $\rho_{\text{trans}}/\rho_0$  (upper panels) and the maximum mass  $M_{\text{TOV}}$  (lower panels). In general, there exists an anticorrelation between  $R_{1.4}$  and  $\rho_{\text{trans}}/\rho_0$  and a correlation between  $R_{1.4}$  and  $M_{\text{TOV}}$ . A conservative upper limit of 13.6 km for  $R_{1.4}$  can be obtained with different analyses (e.g., Bauswein et al., 2017; Annala et al., 2018; Most et al., 2018; Fortin et al., 2016; Abbott et al., 2018; Montaña et al., 2019; Burgio et al., 2018; De et al., 2018). In the upper panel, the upper limit of 13.6 km for  $R_{1.4}$  corresponds to  $\approx 1.3\rho_0$  for  $L = 30$  MeV and  $\approx 1.5\rho_0$  for  $L = 60$  MeV. The

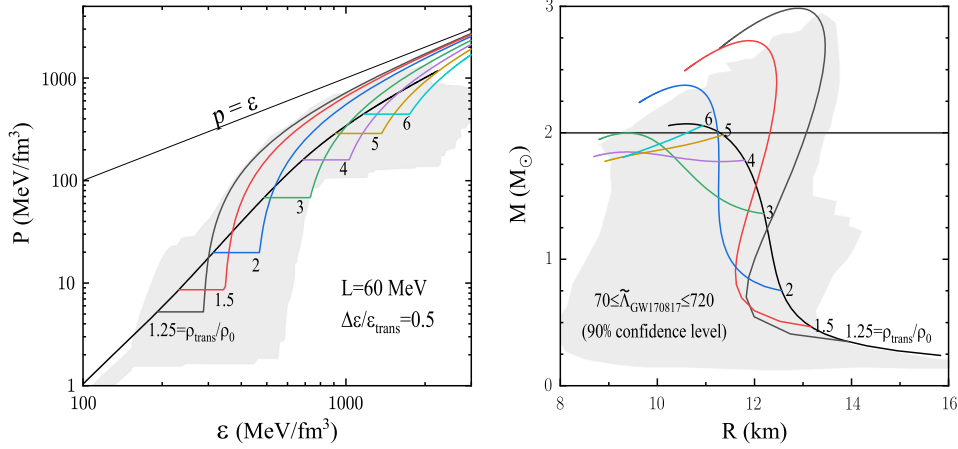


**Fig. 11.** EOSs (left) and mass-radius relations (right) for hybrid stars (colorful curves) at a fixed discontinuity in energy density at the transition  $\Delta\varepsilon/\varepsilon_{\text{trans}} = 0.5$  for different transition densities  $\rho_{\text{trans}}/\rho_0 = 1.25, 1.5, 2, 3, 4, 5, 6$ , with the symmetry energy slope 60 MeV. The squared speed of sound is fixed at  $c_{\text{QM}}^2 = 1$  in the quark matter. The corresponding NS results within the QMF are shown for comparison (black curves). The shaded region is the favored region from the maximal model (Tews et al., 2019), with the underlying EOSs constrained at low densities from EFT, facilitating the complete allowed parameter space for the speed of sound above the saturation density  $n_0$  and enforcing the LIGO/Virgo constraint from GW170817 ( $70 \leq \tilde{\lambda} \leq 720$ ) (Abbott et al., 2019).

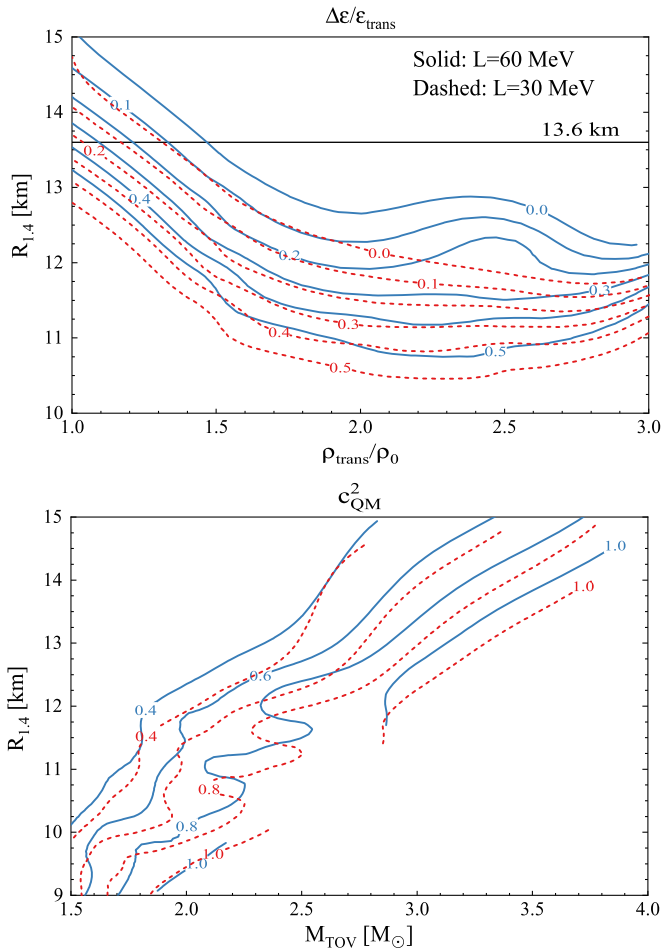


**Fig. 12.** Upper: Radius of a  $1.4 M_{\odot}$  star vs. the transition density, with the energy density discontinuity explicitly indicated; Lower: Radius of a  $1.4 M_{\odot}$  star vs. the maximum mass, with the sound speed explicitly indicated. The results are shown for two kinds of symmetry energy slopes 60 MeV (solid lines) and  $L = 30$  MeV (dashed lines). The horizontal line represents a conservative upper limit of 13.6 km for a  $1.4 M_{\odot}$  star with or without a phase transition (e.g., Bauswein et al., 2017; Annala et al., 2018; Most et al., 2018; Fortin et al., 2016; Abbott et al., 2018; Montaña et al., 2019; Burgio et al., 2018; De et al., 2018). The vertical line in the lower panel represents the 2-solar-mass constraint. There are cases when no  $1.4 M_{\odot}$  star is possible, shown by breaks in the curves. Taken from Miao et al. (2020).

possible onset of a first-order phase transition below such densities might be strongly disfavored. From the mass measurement of heavy pulsars, we can put lower limits on  $R_{1.4}$  by making use of the  $R_{1.4} - M_{\text{TOV}}$  correlation in the lower panel. The 2-solar-mass constraint leads to a lower limit of  $\approx 9.6$  km, in good accordance with other analyses in the literature based on X-ray observations or LIGO/Virgo measurements (e.g., Bauswein et al., 2017; Most et al., 2018; Abbott et al., 2018; Montaña et al., 2019). An upper limit on the maximum mass can also be indicated from  $R_{1.4} < 13.6$  km of  $M_{\text{TOV}} < 3.6 M_{\odot}$ .

We conclude this section by further discussing the following aspects:

- **Submillisecond rotation:** It is commonly believed that only self-bound stable Qs may rotate rapidly with a submillisecond period (Glendenning, 1990). However, it is suggested that pulsars rotating with approximately half a millisecond period could also be interpreted as hybrid stars (Burgio et al., 2003), with NSs containing a metastable deconfined quark phase at their centers. This conclusion does not depend on the quark matter EOS models. Therefore, very rapidly rotating pulsars may be interpreted as either Qs or NSs with deconfined quark matter interiors.
- **Mixed phase:** In the present work, we adopt the simple Maxwell construction. The Gibbs construction provides a realistic model of the phase transition between the hadronic and quark phases inside the star (Glendenning, 1992), yielding a range of baryon densities where both phases coexist, which provides an EOS containing a pure hadronic phase, a mixed phase, and a pure QM region (e.g., Li et al., 2015b; Maruyama et al., 2007). The pressure is the same in the two phases to ensure mechanical stability, while the chemical potentials of the different species are related to each other, satisfying chemical and beta stability. Both the hadron and quark phases are separately charged while preserving total charge neutrality (Glendenning, 1992). As a consequence, the pressure is a monotonically increasing function of the density. The realization of the mixed phase depends on the nuclear surface tension, which is currently an unknown parameter (Xia et al., 2019b). The Gibbs treatment is the zero surface tension limit of the calculations, including finite-size effects. It was demonstrated that the influence of different constructs on the maximum mass value is rather small (Maruyama et al., 2007).

### 4.3. Quark stars and two-branch scenario

We now turn to the description of the bulk properties of uniform quark matter. The strange quark matter is composed of up ( $u$ ), down ( $d$ ) and strange ( $s$ ) quarks with charge neutrality maintained by the inclusion of electrons (hereafter muons as well if present):

$$\frac{2}{3}\rho_u - \frac{1}{3}\rho_d - \frac{1}{3}\rho_s - \rho_e = 0. \quad (43)$$

The baryon number conservation,

$$\frac{1}{3}(\rho_u + \rho_d + \rho_s) = \rho, \quad (44)$$

is also satisfied with  $n$  being the baryon number density. Due to the weak interactions between quarks and leptons,

$$d \rightarrow u + e + \tilde{\nu}_e, \quad u + e \rightarrow d + \nu_e;$$

$$s \rightarrow u + e + \tilde{\nu}_e, \quad u + e \rightarrow s + \nu_e;$$

$$s + u \leftrightarrow d + u.$$

The  $\beta$ -stable conditions  $\mu_s = \mu_d = \mu_u + \mu_e$  should be fulfilled in neutrino-free matter. The energy density and pressure include both contributions from quarks and leptons, and those of leptons can be easily calculated by the model of an ideal Fermi gas such as in the NS matter case.

In the density regime achieved inside compact stars, the dense matter properties cannot be calculated directly from the first principle lattice QCD or perturbative QCD. The latter is only applicable at ultrahigh densities beyond the range of compact stars. The current theoretical description of quark matter is based on phenomenological models (e.g., Li et al., 2010a, 2011) and burdened with large uncertainties. In the following, we consider the non-perturbative contributions from perturbative QCD (Kurkela et al., 2014). For simplicity, we use the pQCD thermodynamic potential density to the order of  $\alpha_s$  (Fraga and Romatschke, 2005),

$$\Omega^{\text{pt}} = \Omega_0 + \Omega_1 \alpha_s, \quad (45)$$

with

$$\Omega_1 = \sum_{i=u,d,s} \frac{g_i m_i^4}{12\pi^3} \left\{ \left[ 6 \ln \left( \frac{\bar{\Lambda}}{m_i} \right) + 4 \right] [u_i v_i - \ln(u_i + v_i)] + 3 [u_i v_i - \ln(u_i + v_i)]^2 - 2v_i^4 \right\}, \quad (46)$$

where  $u_i \equiv \mu_i/m_i$  and  $v_i \equiv \sqrt{u_i^2 - 1}$ . The coupling constant  $\alpha_s$  and quark masses  $m_i$  run with the energy scale and can be determined by (Fraga and Romatschke, 2005),

$$\alpha_s(\bar{\Lambda}) = \frac{1}{\beta_0 L} \left( 1 - \frac{\beta_1 \ln L}{\beta_0^2 L} \right), \quad (47)$$

$$m_i(\bar{\Lambda}) = \hat{m}_i \alpha_s^{\frac{\gamma_0}{\beta_0}} \left[ 1 + \left( \frac{\gamma_1}{\beta_0} - \frac{\beta_1 \gamma_0}{\beta_0^2} \right) \alpha_s \right]. \quad (48)$$

Here,  $L \equiv \ln \left( \frac{\bar{\Lambda}^2}{\Lambda_{\overline{\text{MS}}}^2} \right)$ , and we take the  $\overline{\text{MS}}$  renormalization point  $\Lambda_{\overline{\text{MS}}} = 376.9$  MeV based on the latest results for the strong coupling constant (Olive, 2014). Following Eq. (48), the invariant quark masses are  $\hat{m}_u = 3.8$  MeV,  $\hat{m}_d = 8$  MeV, and  $\hat{m}_s = 158$  MeV. The parameters for the  $\beta$ -function and  $\gamma$ -function are  $\beta_0 = \frac{1}{4\pi} (11 - \frac{2}{3}N_f)$ ,  $\beta_1 = \frac{1}{16\pi^2} (102 - \frac{38}{3}N_f)$ ,  $\gamma_0 = 1/\pi$ , and  $\gamma_1 = \frac{1}{16\pi^2} (\frac{202}{3} -$

$\frac{20}{9}N_f)$  (Vermaseren et al., 1997) (the formulas are for arbitrary  $N_f$ , and in this study,  $N_f = 3$ ). It is not clear how the renormalization scale evolves with the chemical potentials of quarks, and we use  $\bar{\Lambda} = \frac{C_1}{3} \sum_i \mu_i$ , with  $C_1 = 1 - 4$  (Kurkela et al., 2014).

We also introduce the bag mechanism to account for the energy difference between the physical vacuum and perturbative vacuum, and the bag parameter is dynamically scaled (e.g., Burgio et al., 2002; Maieron et al., 2004). The total thermodynamic potential density for strange quark matter can be written as (Xia et al., 2019b),

$$\begin{aligned} \Omega &= \Omega^{\text{pt}} + B \\ &\equiv \Omega^{\text{pt}} + B_{\text{QCD}} + (B_0 - B_{\text{QCD}}) \exp \left[ - \left( \frac{\sum_i \mu_i - 930}{\Delta\mu} \right)^4 \right] \end{aligned} \quad (49)$$

where we take  $B_0 = 40, 50$  MeV/fm<sup>3</sup> (Degrand et al., 1975) for the calculations and  $\Delta\mu = \infty$  indicates no medium effect for the bag parameter. If  $\alpha_s$  and  $m_{u,d,s}$  run with the energy scale as reported by the particle data group (Olive, 2014), the maximum mass of Qs does not reach  $\sim 2 M_\odot$ . In such cases, the dynamic rescaling of the bag constant with finite  $\Delta\mu$  is essential, which basically originates from nonperturbative effects such as chiral symmetry breaking and color superconductivity (Alford et al., 2008; Baym et al., 2018; Buballa, 2005).  $B_{\text{QCD}} = 400$  MeV/fm<sup>3</sup> is demanded by the dynamic equilibrium condition at the critical temperature of the deconfinement phase transition and is obtained by equating the pressures of the QGP ( $-B_{\text{QCD}} + 37\pi^2 T^4/90$ ) and pion gas ( $\pi^2 T^4/30$ ) at  $T = T_c$  ( $\sim 170$  MeV).

At given chemical potentials  $\mu_i$ , the pressure  $P$ , particle number density  $\rho_i$ , and energy density  $\varepsilon$  are determined by:

$$P = -\Omega, \quad (50)$$

$$\rho_i = \frac{g_i}{6\pi^2} (\mu_i^2 - m_i^2)^3 - \frac{\partial \Omega_1}{\partial \mu_i} \alpha_s + \rho_0, \quad (51)$$

$$\varepsilon = \Omega + \sum_i \mu_i \rho_i. \quad (52)$$

The common term for the particle number density in Eq. (51) is obtained with

$$\begin{aligned} \rho_0 &= -\frac{C_1}{3} \sum_i \left( \frac{\partial \Omega_0}{\partial m_i} + \frac{\partial \Omega_1}{\partial m_i} \alpha_s \right) \frac{dm_i}{d\bar{\Lambda}} \\ &\quad + \frac{C_1}{3} \frac{\partial \Omega_1}{\partial \bar{\Lambda}} \alpha_s + \frac{C_1}{3} \Omega_1 \frac{d\alpha_s}{d\bar{\Lambda}} - \frac{\partial B}{\partial \mu_i}. \end{aligned} \quad (53)$$

In Fig. 13, we show the EOSs generated in the perturbation model, which fulfill the available astrophysical constraints of mass (Demorest et al., 2010; Antoniadis et al., 2013; Fonseca et al., 2016; Arzoumanian et al., 2018; Cromartie et al., 2020), radius (Miller et al., 2019; Riley et al., 2019) and tidal deformability (Abbott et al., 2019) for Qs. They are compared with the results of pQCD without nonperturbative corrections, taking  $C_1 = 1 - 4$  and  $B = 0$ . The EOSs for the nuclear matter obtained with the QMF models are also shown. (Bedaque and Steiner, 2015) pointed out that if the 2-solar-mass constraint is combined with the hadronic matter EOS below and around the nuclear saturation density,  $c_{\text{QM}}$  might first increase then decrease after reaching a maximum (maybe even up to 0.9c) and finally approach the conformal limit  $c/\sqrt{3}$  from below. This peculiar shape resembles the analysis of the case of crossover EOS (Baym et al., 2019). To ensure a large mass for Qs above  $2 M_\odot$ , the obtained peak value ( $c_{\text{QM}}^{\text{max}}$ ) ranges from 0.68c to c, similar to previous results for NSs (Kurkela et al., 2014; Alsing et al., 2018; Tews et al., 2018; McLerran and Reddy, 2019).

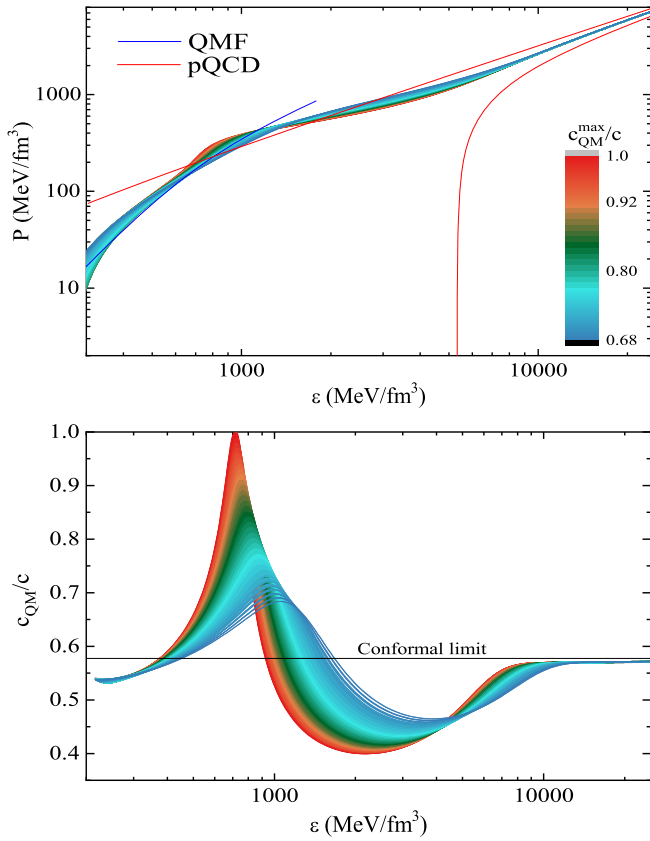


**Fig. 13.** EOSs (left) and sound speed  $c_{QM}$  (right) of SQM. The EOSs are generated in the perturbation model, fulfilling the available astrophysical constraints of mass (Demorest et al., 2010; Antoniadis et al., 2013; Fonseca et al., 2016; Arzoumanian et al., 2018; Cromartie et al., 2020), radius (Miller et al., 2019; Riley et al., 2019) and tidal deformability (Abbott et al., 2019) for QSs. They are compared with the results of the perturbative QCD (red curve) without nonperturbative corrections. The EOS of the nuclear matter obtained with the QMF (blue curve) is shown in the left panel. The maximum sound speeds  $c_{QM}^{\max}$  are explicitly indicated. The horizontal lines in the  $c_{QM}$  plot show the conformal limit. To ensure a large mass for QSs above  $2 M_{\odot}$ , the sound speed is necessarily large,  $c_{QM}/c > 0.68$ . Taken from (Xia et al., 2019a).

We show in Fig. 14 the various properties of strange quark matter based on the perturbation model using the exemplary parameters of  $C_1 = 3.5$ ,  $B_0 = 40$  MeV/fm<sup>3</sup>, and  $\Delta\mu = 800$  MeV. The composition, binding energy, pressure, sound velocity, and scaled bag parameter are shown as functions of the baryon density or chemical potential. Note that in the binding energy plot, the condition that the strange quark matter be the absolute stable strong-interaction system, requiring that at  $P = 0$ ,  $E/A \leq M(^{56}\text{Fe}/56) = 930$  MeV, is fulfilled. Fig. 15 shows the predicted properties of the QSs, including the mass, Love number, and tidal deformability.

Previously, although the quark star EOS models could reach  $2 M_{\odot}$ , they required a too small surface density (not much larger than the nuclear saturation density) in some cases, and a larger maximum mass meant an even smaller surface density (because of the anticorrelation between the two (Li et al., 2017)), for example, the CDDM2 model (Li et al., 2016c) and the PMQS3 model (Li et al., 2017). Then, the radius (and the tidal deformability) exceeded the observational values (Abbott et al., 2017d, 2019; Miller et al., 2019; Riley et al., 2019). These models were not welcomed by particle physicists studying hadrons (for which experiments have been established studying the nonperturbative effects) because in such a density realm, the quarks are thought to be very dilute and are very possibly confined inside hadrons. In the real world, we do

obtain nuclear matter rather than quark matter around the nuclear saturation density. The present perturbative model with an in-medium bag can achieve both a reasonable surface density and a maximum mass as large as  $2.2 M_{\odot}$ . The predicted properties of dense matter ( $c_{QM}, \Gamma$ ) and quark stars ( $R, M$ ), as well as the EOS of Fig. 14, are collected in Table 2.

We conclude this section by further discussing the following aspects:

- *QS vs. hybrid stars:* Although it is known that the degree of freedom is hadronic around the nuclear saturation density, the QCD phase state for cold, dense matter of intermediate densities is unfortunately unknown, and a great deal of effort is being applied in the communities of astrophysics, nuclear physics, and particle physics due to the crucial importance of this aspect. One key point is still not clear: Does the matter go through a phase transition from hadron matter to quark matter at some densities (which is relevant to compact star physics) or is quark matter the absolute ground state of strongly interacting matter (the conjecture of Bodmer-Witten (Bodmer, 1971; Witten, 1984))? Therefore, there remains the problem of how to verify QSs or distinguish them from NSs or hybrid stars (e.g., Alford et al., 2005; Wei et al., 2019). For a fixed gravitational mass, hybrid stars are characterized by a smaller radius than their hadronic counterparts and could be as compact as QSs for masses above  $1.0 M_{\odot}$ . The similarity of the sound speed of the hadron-quark mixed phase with that of the pure quark matter in the intermediate density region of  $\sim 3 - 8\rho_0$ , a particular shape with a peak, further complicates the distinguishing of QS from hybrid stars (Xia et al., 2019a).
- *Two branch scenario:* Because of the tension of a low tidal deformability ( $190^{+390}_{-120}$  (Abbott et al., 2018)) and a high maximum mass ( $2.14^{+0.20}_{-0.18} M_{\odot}$  for the presently heaviest pulsar (Cromartie et al., 2020) and  $\leq 2.35 M_{\odot}$  based on the numerical simulation studies on NS binary mergers (Rezzolla et al., 2018; Ruiz et al., 2018; Shibata et al., 2019)) for a certain EOS in the NS model, binary QSs have been proposed as the possible scenario for the GW170817 event (Zhou et al., 2018b; Lai et al., 2018a). A binary QS merger for some binary configurations could eject amounts of matter (comparable to the binary NS case) to account for the electromagnetic observations in the optical/infrared/UV bands (namely, kilonova) (Bauswein et al., 2009). A magnetar with QS EOS is preferred as the post-merger remnant for explaining some groups of short gamma-ray burst (SGRB) observations (Li et al., 2016c, 2017). It has been suggested that because of this discrepancy (if confirmed), small and large stars of the same mass could coexist as hadronic and quark matter stars (Wiktorowicz et al., 2017; Drago and Pagliara, 2018).
- *Comments on the maximum mass of NS/QS:* Various microscopic calculations of NS matter (without strangeness) indicate a possible upper limit of  $\sim 2.3 - 2.4 M_{\odot}$  for the NS maximum mass, for example, Brueckner theory calculations (Rijken and Schulze, 2016) and quantum Monte Carlo calculations (Gandolfi et al., 2020). Exotic particles, if they are present, usually lower the limit as a result of the extra degrees of freedom during the phase transition (while the appearance of quarks might increase the limit in the case of crossover (Wang et al., 2019; Baym et al., 2019)). The quark-hadron crossover EOS gives a maximum mass of  $2.35 M_{\odot}$  (Baym et al., 2019). The bound of  $M_{TOV} \lesssim 2.3 - 2.4 M_{\odot}$  may be applicable to QSs. For example, the maximum mass of QSs is  $2.18 M_{\odot}$  ( $2.32 M_{\odot}$  with color-flavor-locked (CFL) superfluidity (Alford et al., 1999)) within the MIT bag model (Zhou et al., 2018b). A more updated analysis has found that, for CFL quark stars,  $M_{TOV}$  is in the range

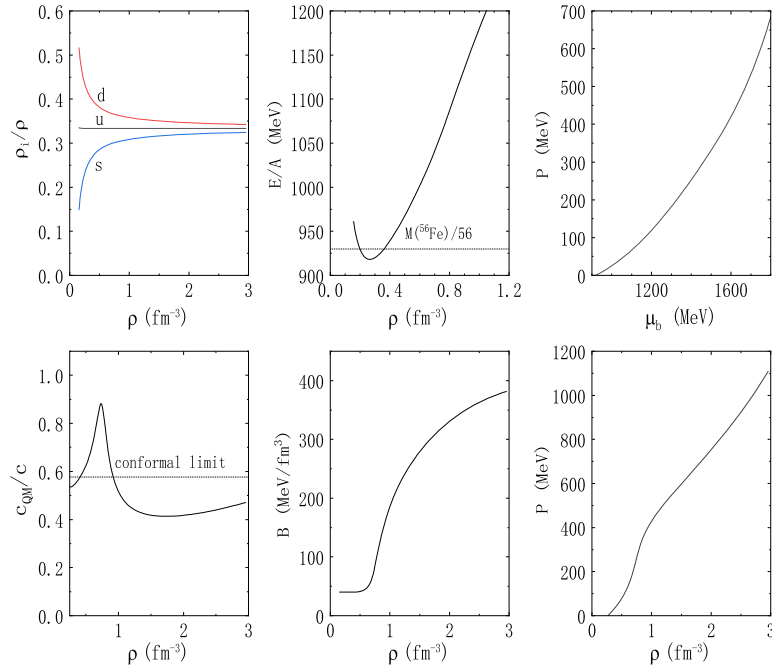


**Fig. 14.** Various properties of betastable strange quark matter, including the quark fractions, the binding energy, the pressure, the sound velocity, and the scaled bag parameter, which are plotted as a function of the baryon density or chemical potential. The calculations are performed based on the perturbation model using the parameters  $C_1 = 3.5$ ,  $B_0 = 40 \text{ MeV/fm}^3$ , and  $\Delta\mu = 800 \text{ MeV}$ . The horizontal line in the  $E/A$  plot indicates that of the most stable  $^{56}\text{Fe}$  nucleus. The horizontal line in the  $c_{\text{QM}}$  plot shows the conformal limit.

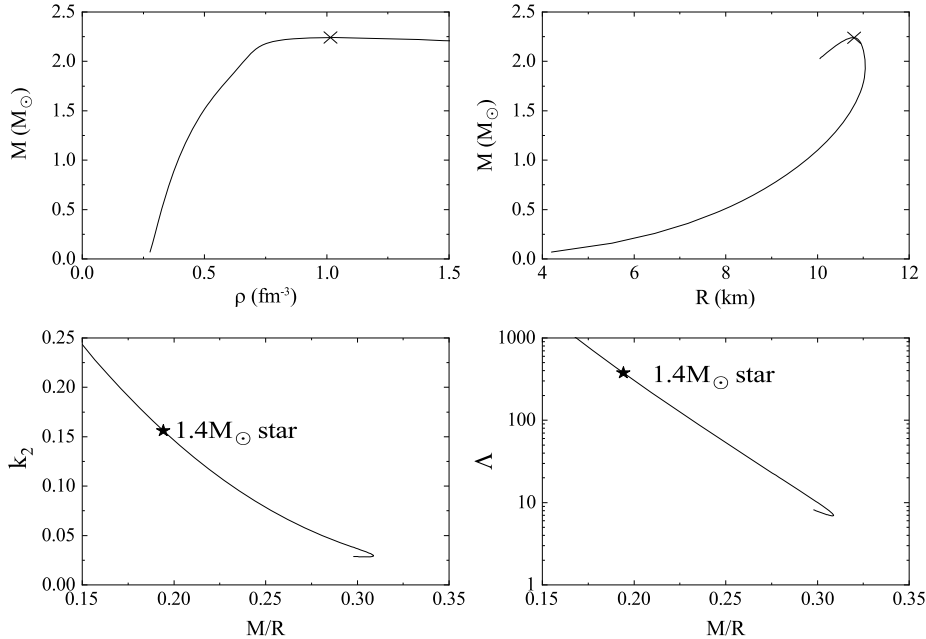


**Fig. 15.** Various properties of Qs based on the EOS in Fig. 14, including the gravitational mass, the Love number, and the tidal deformability, which are plotted as a function of central density, radius, or compactness. The crosses in the upper two panels show where the maximum mass is reached. The locations of a  $1.4 M_\odot$  star are explicitly indicated in the lower two panels.

of  $2.03 - 2.31 M_\odot$  (Li et al., 2020), to the 90% credibility interval. The present perturbation model yields  $2.24 M_\odot$  with the peak sound speed ( $c_{\text{QM}}^{\text{max}}$ ) approaching the speed of sound (we expect an increase in the value including the uncertain superfluity of  $\sim 0.1 M_\odot$ ). These high theoretical limits on the maximum mass are higher than (but close to) the observational bound of pulsars of approximately  $2.14 M_\odot$  (Cromartie et al., 2020). A looser upper limit based on extreme causal EOSs may be in the range of  $M_{\text{TOV}} < 3.6 - 4.8 M_\odot$  (Tews et al., 2019;

Kalogera and Baym, 1996; Rhoades and Ruffini, 1974; Brecher and Caporaso, 1976). The observations of accreting black holes, on the other hand, revealed a paucity of sources with masses below  $5 M_\odot$  (e.g., Bailyn et al., 1998; Özel et al., 2010; Farr et al., 2011; Kreidberg et al., 2012). Presently, binary mergers involving one or two companions have masses that fall into the so-called mass gap range ( $3 - 5 M_\odot$ ) that are hard to distinguish (e.g., Wyrzykowski and Mandel, 2020; Tsokaros et al., 2020; Abbott et al., 2020a).

**Table 2**

QS EOS with proper sound velocity behavior and the predicted properties of dense matter ( $c_{\text{QM}}, \Gamma$ ) and quark stars ( $R, M$ ). The calculations are done based on the perturbation model using the parameters  $C_1 = 3.5$ ,  $B_0 = 40$  MeV/fm<sup>3</sup>, and  $\Delta\mu = 800$  MeV. See Sec. 4.3 for details.

$\rho$ (fm <sup>-3</sup> )	$\varepsilon$ (MeV/fm <sup>3</sup> )	$P$ (MeV/fm <sup>3</sup> )	$c_{\text{QM}}/c$	$\Gamma$	$R$ (km)	$M/M_{\odot}$
0.277	254.68	3.22	0.5365	23.053	3.834	0.0530
0.288	264.47	6.04	0.5380	12.954	5.256	0.1384
0.298	274.56	8.98	0.5400	9.2107	6.241	0.2350
0.309	284.94	12.01	0.5423	7.2695	6.991	0.3350
0.320	295.59	15.16	0.5450	6.0880	7.589	0.4348
0.332	306.51	18.42	0.5481	5.2979	8.078	0.5320
0.343	317.66	21.79	0.5514	4.7358	8.486	0.6256
0.354	329.05	25.28	0.5551	4.3183	8.831	0.7148
0.366	340.66	28.88	0.5590	3.9983	9.123	0.7994
0.378	352.47	32.60	0.5632	3.7473	9.375	0.8793
0.389	364.46	36.43	0.5677	3.5469	9.591	0.9546
0.401	376.61	40.38	0.5725	3.3848	9.778	1.0253
0.413	388.91	44.45	0.5776	3.2525	9.941	1.0918
0.425	401.35	48.64	0.5829	3.1440	10.082	1.1541
0.436	413.89	52.94	0.5886	3.0548	10.205	1.2125
0.448	426.53	57.36	0.5945	2.9814	10.313	1.2673
0.460	439.24	61.90	0.6007	2.9215	10.406	1.3187
0.471	452.00	66.56	0.6073	2.8730	10.488	1.3669
0.483	464.80	71.33	0.6141	2.8345	10.559	1.4122
0.494	477.61	76.22	0.6213	2.8047	10.621	1.4546
0.506	490.42	81.22	0.6288	2.7826	10.675	1.4945
0.517	503.19	86.34	0.6366	2.7676	10.721	1.5320
0.528	515.93	91.56	0.6449	2.7590	10.761	1.5672
0.539	528.59	96.90	0.6535	2.7564	10.796	1.6004
0.550	541.18	102.35	0.6624	2.7592	10.825	1.6317
0.561	553.65	107.90	0.6718	2.7673	10.850	1.6612
0.571	566.01	113.56	0.6816	2.7802	10.871	1.6890
0.581	578.23	119.32	0.6918	2.7978	10.888	1.7153
0.591	590.30	125.18	0.7024	2.8198	10.902	1.7402
0.601	602.20	131.15	0.7134	2.8460	10.914	1.7638
0.611	613.92	137.20	0.7248	2.8760	10.922	1.7861
0.620	625.44	143.36	0.7366	2.9097	10.929	1.8073
0.629	636.77	149.60	0.7487	2.9465	10.933	1.8274
0.638	647.89	155.94	0.7611	2.9862	10.936	1.8465
0.647	658.79	162.36	0.7738	3.0280	10.937	1.8647
0.655	669.49	168.87	0.7865	3.0713	10.936	1.8821
0.663	679.97	175.46	0.7994	3.1152	10.934	1.8986
0.671	690.25	182.13	0.8121	3.1586	10.931	1.9144
0.679	700.32	188.88	0.8245	3.2002	10.928	1.9295
0.686	710.22	195.71	0.8364	3.2383	10.923	1.9439
0.694	719.95	202.61	0.8476	3.2711	10.917	1.9577
0.701	729.54	209.58	0.8577	3.2966	10.911	1.9710
0.708	739.02	216.62	0.8665	3.3126	10.904	1.9837
0.715	748.41	223.74	0.8737	3.3169	10.896	1.9958
0.722	757.76	230.92	0.8789	3.3073	10.888	2.0075
0.728	767.11	238.17	0.8818	3.2818	10.879	2.0186
0.735	776.51	245.49	0.8821	3.2391	10.870	2.0294
0.742	786.03	252.88	0.8796	3.1783	10.861	2.0396
0.749	795.72	260.33	0.8741	3.0995	10.851	2.0495
0.756	805.66	267.85	0.8657	3.0037	10.841	2.0589
0.763	815.92	275.45	0.8544	2.8926	10.830	2.0679
0.771	826.60	283.12	0.8405	2.7687	10.819	2.0766
0.778	837.77	290.86	0.8241	2.6351	10.808	2.0848
0.786	849.55	298.69	0.8056	2.4952	10.797	2.0926
0.795	862.04	306.60	0.7856	2.3523	10.785	2.1000
0.804	875.36	314.59	0.7643	2.2095	10.773	2.1071
0.814	889.61	322.68	0.7422	2.0696	10.761	2.1137
0.824	904.94	330.86	0.7197	1.9348	10.749	2.1199
0.835	921.47	339.16	0.6972	1.8069	10.736	2.1257
0.847	939.33	347.56	0.6750	1.6869	10.723	2.1311
0.859	958.68	356.09	0.6532	1.5756	10.710	2.1360
0.873	979.66	364.75	0.6322	1.4734	10.696	2.1406
0.888	1002.41	373.56	0.6121	1.3802	10.682	2.1446
0.904	1027.09	382.51	0.5930	1.2958	10.668	2.1483
0.921	1053.86	391.63	0.5749	1.2199	10.653	2.1515
0.939	1082.86	400.93	0.5579	1.1520	10.638	2.1542
0.959	1114.25	410.42	0.5421	1.0915	10.623	2.1565
0.980	1148.18	420.11	0.5273	1.0380	10.607	2.1583
1.003	1184.80	430.03	0.5137	0.9909	10.591	2.1596
1.054	1266.67	450.58	0.4896	0.9136	10.558	2.1609

## 5. Neutron star binary

The gravitational waves (GWs) detected from binary neutron star (BNS) merger event GW170817 (Abbott et al., 2017a), as well as its electromagnetic (EM) counterparts (Abbott et al., 2017f), announced the beginning of the multimessenger astronomy era. In addition to hinting at the origin of SGRB (Abbott et al., 2017d; Narayan et al., 1992) and revealing the site of r-process nucleosynthesis (Abbott et al., 2017e; Eichler et al., 1989), our knowledge of the EOS of cold dense matter at supranuclear densities has been greatly enriched. In the past year, various studies have been performed to constrain the EOS of dense matter, either by putting constraints on observable characteristics of NSs (i.e., radius or tidal deformability; see e.g., Annala et al., 2018; Most et al., 2018; Abbott et al., 2018) or by connecting the constraint with model parameters in nuclear physics (i.e., symmetry energy slope or neutron skin parameter; see e.g., Zhu et al., 2018; Fattoyev et al., 2018), which could be tested by nuclear physics experiments. Some studies also go beyond the conventional NS scenario and put constraints on compact star models involving strong interaction phase transitions (e.g., Most et al., 2018; Zhou et al., 2018b; Chatziioannou and Han, 2020; Montaña et al., 2019).

Those constraints mainly come from 3 aspects from a BNS merger event. First, during the inspiral stage, unlike binary black hole (BBH) mergers, deformation is induced for each NS due to the tidal field of the companion, providing additional dissipation of the orbital energy and angular momentum and hence accelerating coalescence (Abbott et al., 2017a). This deformation therefore leaves a detectable signature in the GW signal of the late inspiral stage, from which we can learn about the tidal deformability of the NS EOSs (Flanagan and Hinderer, 2008). Second, the detection of SGRB hints at a delayed collapse to a BH for the merger remnant (Lawrence et al., 2015; Murguia-Berthier et al., 2014). This interpretation of the SGRB observation provides information on the maximum mass of a nonrotating configuration for the NS EOS (namely,  $M_{\text{TOV}}$ ). For instance, the EOS should not be too stiff; otherwise, the remnant supramassive NS lives much longer (Ai et al., 2018) in the magnetar central engine model (Dai et al., 2006; Metzger et al., 2008b). However, if the EOS is too soft, the merger might result in a prompt collapse to a BH. In such occasions, the magnetic field might not be enhanced sufficiently (by a differentially rotating NS remnant) and thus not able to launch a jet (Ruiz et al., 2018). Third, the features of the transient optical/infrared/UV observations (namely, the kilonova) powered by the radio activity of the neutron-rich elements in the ejecta depend directly on the mass, velocity and electron fraction in the ejecta, which is related to the properties of the EOS for the merging NS.

In this section, we briefly review the information we have learned about the EOS of NSs from the BNS merger events GW170817 and GRB170817A as well as AT2017gfo.

### 5.1. GW170817 and tidal deformability

The finite size effects of NSs alter the late inspiral GW signal compared with that of the BBH case (Flanagan and Hinderer, 2008; Hinderer, 2008). Through the leading order, the GW observations constrained a combination of the tidal deformability for each NS in the binary ( $\Lambda_1$  and  $\Lambda_2$ ) (Abbott et al., 2017a).

$$\tilde{\Lambda} = \frac{16}{13} \frac{(12q + 1)\Lambda_1 + (12 + q)q^4\Lambda_2}{(1 + q)^5}, \quad (54)$$

in which  $q = M_2/M_1$  is the mass ratio of the binary. The dimensionless tidal deformability of each star is

$$\Lambda = \frac{2}{3} k_2 \left(\frac{R}{M}\right)^5, \quad (55)$$

where  $k_2$  is the tidal Love number describing the fraction between the induced quadrupole moment of a star and the external tidal field and  $R$  and  $M$  are the radius and mass of the star, respectively. On the other hand,  $k_2$  can be obtained for a given EOS for any given mass and hence can be tested with the observation of GW170817.

Practically, the tidal deformability is fitted to the GW observation together with other parameters (Abbott et al., 2019). For instance, in the Taylor F2 post-Newtonian aligned-spin model, 13 parameters need to be fitted, including 7 extrinsic parameters (sky location, distance of the source, polarization angle, inclination angle and coalescence phase and time) and 6 intrinsic parameters (mass of each NS, tidal deformability of each NS and the aligned spin of each NS). Therefore, the uncertainties in the estimation of other parameters weakly correlate with the determination of the tidal deformability. Hence, the constraint on the tidal deformability is normally made with certain assumptions.

For instance, as seen in (Abbott et al., 2017a), the assumption in the spin parameter of the NS could significantly affect the interpretation of the mass of each NS, thus further affecting the constraint on the tidal deformability. Through the assumption that the  $\Lambda$  of each NS vary independently, the first constraint on  $\Lambda_1$  and  $\Lambda_2$  could be obtained under different spin priors. The result favors the softer EOS, i.e., the EOS that predicts more compact stars. Another analysis assumes a uniform prior for  $\tilde{\Lambda}$ , which sets an upper limit of 800 on  $\tilde{\Lambda}$  in the low-spin case and 700 in the high spin case. Alternatively, through the expansion of  $\Lambda(M)$  around a certain  $M$ , constraints can be directly placed on the tidal deformability of a certain mass star. This constraint is  $\Lambda(1.4) \leq 1400$  in the high-spin case and  $\Lambda(1.4) \leq 800$  in the low-spin case.

Follow-up analysis further improves these constraints under more assumptions. For example, in (Abbott et al., 2018), instead of assuming an independent and uniform prior for the tidal deformability of each star, the EOS of each star in the merging binary is assumed to be the same. Consequently, the area of the 90% confidence region in the  $\Lambda_1$ - $\Lambda_2$  parameter space shrinks by a factor of 3. This also improves the determination of  $\Lambda(1.4)$  to  $190^{+390}_{-120}$ . In (Abbott et al., 2019), a lower cut-off frequency of 23 Hz is used instead of the 30 Hz in the original analysis. Although the tidal effects mainly affect the GW signals above several hundred Hz, a lower frequency cut off allows for the better determination of other parameters, hence improving the measurement of the tidal deformability. In (De et al., 2018), it was pointed out that under the assumption that two stars in a binary system have a common EOS, there is an approximate relation between the tidal deformability of each star, i.e.,  $\Lambda_1/\Lambda_2 = q^6$ , where  $q$  is the mass ratio. With the aid of this relation, once the assumption in the mass ratio of the binary is made, the tidal deformability can be further constrained. In (De et al., 2018), the improved analysis shows that  $\tilde{\Lambda}$  is  $222^{+420}_{-138}$  for a uniform mass prior and  $245^{+453}_{-151}$  for a mass prior inferred from observed double neutron star systems and  $233^{+448}_{-144}$  for a mass prior informed by all galactic neutron star masses within the 90% credibility level.

We can directly test existing EOS models by simply calculating the tidal deformability and comparing it with the observational constraint. Nevertheless, more insight could be gained regarding the EOS of neutron-rich matter by more systematically studying the impact of the EOS (i.e.,  $p$  as a function of  $\varepsilon$ , where  $p$  and  $\varepsilon$  are the pressure and rest mass density of the matter) on the tidal deformability. Such interpretations are presented in (e.g., Annala et al., 2018; Most et al., 2018; Abbott et al., 2018). For instance, in (Abbott et al., 2018), the logarithm of the adiabatic index of the EOSs is treated as a polynomial of the pressure for the high density EOS, namely,  $\Gamma = \Gamma(p; \gamma_i)$  and  $\gamma_i = (\gamma_0, \gamma_1, \gamma_2, \gamma_3)$  are free parameters. For densities below half the nuclear saturation density, the EOS is connected to the SLy EOS (Douchin and Haensel, 2001).

The sampling of the EOS then consists of uniformly sampling  $\gamma_i$  in certain intervals. For each of the EOS samples, the mass radius relation and tidal deformability could be theoretically obtained and constrained by the observation of both the tidal deformability and  $2 M_\odot$  pulsars (Demorest et al., 2010; Antoniadis et al., 2013; Fonseca et al., 2016; Arzoumanian et al., 2018; Cromartie et al., 2020). The constraint on the neutron star radius is  $R = 11.9^{+1.4}_{-1.4}$  km for the merging binary of GW170817. Similar analysis can be found in, e.g., (Annala et al., 2018), which shows that the radius of a 1.4 solar mass NS is in the range of [9.9, 13.8] km. However, it is worth noting that such analysis might be affected by the choice of EOS priors. In (Most et al., 2018), it was pointed out that when the prior for possible twin star (for which there is a hadron-quark phase transition inside the star) branch EOSs is considered, the radius becomes less constrained, i.e.,  $R_{1.4} \in [8.53, 13.74]$  km.

In addition to systematic studies on parameterized EOS priors, phenomenological models can be applied to interpret tidal deformability constraints. According to (Fattoyev et al., 2018), a better upper limit for neutron skin effects is obtained compared with that of the experiment done by PREX, and better results could be achieved with future GW observations and terrestrial nuclear physics experiments. Both the symmetry energy parameter and the symmetry energy slope are better constrained with respect to previous nuclear physics studies (Zhu et al., 2018). Under the assumption that GW170817 originates from a binary quark star (BQS) merger, the quark interaction parameters are studied in (Zhou et al., 2018b). Fig. 16 shows the results of both normal and superfluid QSs. It is worth noting that due to the finite surface density of QSs, a surface correction needs to be taken into account when calculating  $\Lambda$  of a QS (Damour and Nagar, 2009). Therefore, a QS could have a larger TOV maximum mass without violating the tidal deformability constraint compared with those of NSs (Lai et al., 2019).

## 5.2. GRB170817A and merger remnant

BNS mergers have long been proposed as the central engine of SGRBs (Narayan et al., 1992). This suggestion has been verified by GRB170817A detected by Fermi/GBM and INTEGRAL/SPI-ACS, which accompanies the detection of GW170817. According to the time of the merger implied from the chirp signal, there is a  $1.74 \pm 0.05$  s delay for the onset of the SGRB (Abbott et al., 2017e). The detection of GRB170817A not only helps the determination of the location of the source, which allows for abundant follow-up observations in other bands, but also provides useful information about the post-merger evolution of the merger event, thus providing constraints on the EOSs (e.g., Gao et al., 2016; Ma et al., 2018; Gao et al., 2020). Exemplary fractions of the outcome of the binary are shown in Fig. 17 using both NS and QS EOSs. The dependence on the EOS, as well as the initial period, is evident (Li et al., 2017). It is found that the fraction of stable star (panel (a)) is determined by the static maximum mass  $M_{\text{TOV}}$ . The fractions of supermassive star (panel (b)) and black hole (panel (c)) are further sensitive to the initial period since the fast-rotating configurations of the star have to be taken into account for them (Li et al., 2016c).

Depending on the TOV maximum mass of the NS EOS and the total mass of the merging binary, there could be 4 different outcomes after the merger:

- if the total mass of the binary system ( $M_{\text{tot}}$ ) is much larger than  $M_{\text{TOV}}$ , the direct formation of a black hole (BH) on a dynamic time scale, namely, prompt collapse, occurs. The total binary mass, above which prompt collapse can occur, is denoted as the threshold mass ( $M_{\text{thres}}$ );
- if  $M_{\text{tot}}$  is smaller than  $M_{\text{thres}}$  but larger than the maximum mass that can be reached by uniformly rotating NSs (denoted

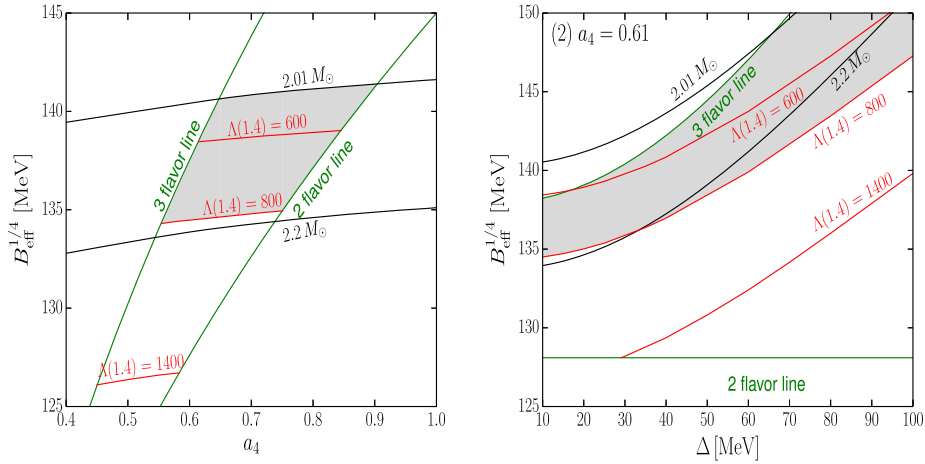


**Fig. 16.** Parameter space for QS EOS models within the MIT bag model ( $B_{\text{eff}}, a_4, \Delta$ ) for normal QSs (left) and superfluid QSs (right) obtained by combining the GW170817 constraint on  $\Lambda(1.4)$ , the 2-solar-mass constraint on  $M_{\text{TOV}}$  and the stability window for quark matter. With the constraint of the “2 flavor” line, we ensure that normal atomic nuclei do not decay into nonstrange quark matter. With the constraint of the “3 flavor” line, we ensure that strange quark matter is more stable than normal matter, namely, Bodmer-Witten’s conjecture (Bodmer, 1971; Witten, 1984). The perturbative QCD correction parameter  $a_4$  characterizes the degree of the quark interaction correction, with  $a_4 = 1$  corresponding to no QCD corrections (Fermi gas approximation).  $a_4 = 0.61$  is chosen to be close to the calculated result with different choices of the renormalization scale (Fraga et al., 2001). The effective bag constant ( $B_{\text{eff}}$ ) also includes a phenomenological representation of nonperturbative QCD effects. Due to the strong correlation between  $M_{\text{TOV}}$  and  $\Lambda(1.4)$ , a lower bound can be inferred for  $\Lambda(1.4)$  from the 2-solar-mass limit, namely,  $\sim 510$  ( $\sim 380$ ) MeV for normal (superfluid) QSs. Taken from Zhou et al. (2018b).

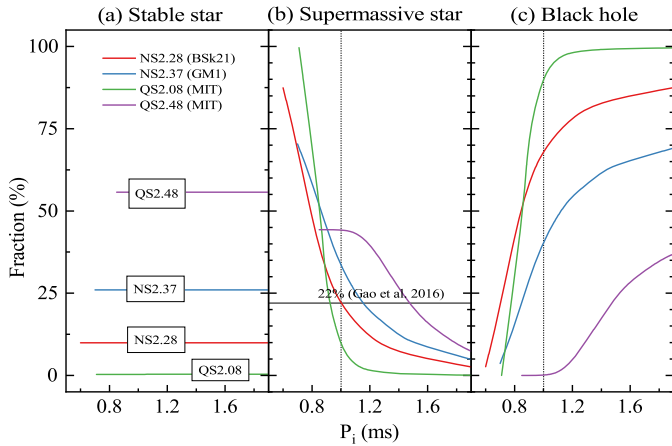


**Fig. 17.** Postmerger product fractions for (a) stable star, (b) supermassive star and (c) black hole for the NS and QS EOS models, labeled with the star type plus the corresponding  $M_{\text{TOV}}$ : Unified BSk21 (red line labeled NS2.28), nonuniform GM1 (blue line labeled NS2.37), and MIT model (green and purple lines labeled QS2.08 and QS2.48). In panel (b), the observed 22% constraint for supermassive stars from Gao et al. (2016) is shown by the horizontal line for comparison. The vertical dotted line in the same panel is for a typical initial period of 1 ms. Taken from Li et al. (2017).

$M_{\text{supra}}$ ), then a short-lived NS could exist as a remnant supported by differential rotation.<sup>3</sup> The differential rotation dissipates due to magnetorotational instabilities as well as viscosity within a timescale of  $\sim 100$  ms, and then the NS collapses to a BH;

- if  $M_{\text{tot}}$  is smaller than  $M_{\text{supra}}$  but larger than  $M_{\text{TOV}}$ , the remnant is a long-lived supramassive NS. The uniformly rotating NS could still lose angular momentum by magnetic dipole radiation, but it takes a much longer time to sufficiently reduce the angular momentum to induce the collapse to a BH;
- if  $M_{\text{tot}}$  is smaller than  $M_{\text{TOV}}$ , a stable NS remnant exists.

The GW observations do not provide any hint to which scenario applies to the case of GW170817 due to the lack of post-

merger GW observations (Abbott et al., 2017a,c). The electromagnetic counterparts, on the other hand, can indicate what happens after the merger of the two NSs.

A very robust interpretation is that scenario 1) should be excluded due to the SGRB detected. According to Ruiz et al. (2018), in the BH central engine model for SGRBs, enhancement in the magnetic field of the merger remnant due to the differential rotation of the hypermassive NS is essential for jet formation. A prompt collapse results in a magnetic field that is too weak to explain the SGRB observations. Hence, the detection of GRB170817A directly implies  $M_{\text{tot}} < M_{\text{thres}}$  for the case of GW170817. The total mass of the binary can be measured by the inspiral GW signal, which places a constraint on  $M_{\text{thres}}$ .

For a given EOS model, the threshold mass can be determined by performing numerical simulations with different total binary masses. This can be extremely time-consuming for full 3-dimensional general relativistic simulations. In Bauswein et al. (2017), the so-called smooth particle hydrodynamics (SPH) method as well as a conformally flat assumption for the spacetime metric is used to reduce the simulation time to make it plausible. According to the results, the threshold mass is related to  $M_{\text{TOV}}$  and  $R_{\text{TOV}}$  (i.e., the radius of the TOV maximum mass configuration) as

$$M_{\text{thres}} = (-3.38 \frac{M_{\text{TOV}}}{R_{\text{TOV}}} + 2.43) M_{\text{TOV}}. \quad (56)$$

Alternatively, the results can be fitted with similar accuracy in terms of the radius of a 1.6 solar mass star ( $R_{1.6}$ ) as

$$M_{\text{thres}} = (-3.606 \frac{M_{\text{TOV}}}{R_{1.6}} + 2.38) M_{\text{TOV}}. \quad (57)$$

Note that this reveals a quadratic relation between  $M_{\text{thres}}$  and  $M_{\text{TOV}}$  once  $R_{\text{TOV}}$  (or  $R_{1.6}$ ) is fixed. Particularly, since the coefficient of the  $M_{\text{TOV}}^2$  term is negative, there exists a maximum value for  $M_{\text{thres}}$ . This maximum possible value of  $M_{\text{thres}}$  must be larger than  $M_{\text{tot}}$  in the case of GW170817; otherwise, there is no parameter space to prevent a prompt collapse. In other words, any choice of  $R_{\text{TOV}}$  (or  $R_{1.6}$ ) that results in a maximum possible value  $M_{\text{thres}}$  smaller than 2.74 solar mass should be excluded by the observations. This requires  $R_{\text{TOV}}$  to be larger than 9.26 km and  $R_{1.6}$  to be larger than 10.30 km.

<sup>3</sup> Such NSs are called hypermassive NSs (HMNS). NSs that can be supported by only uniform rotation are called supramassive NSs (SMNS).

For NS EOS models, scenario 4) can also be excluded. Scenario 4) requires a very large  $M_{\text{TOV}}$ , which results in a large tidal deformability, hence violating the tidal deformability constraint.<sup>4</sup> Distinguishing between scenarios 2) and 3) could indicate more on the TOV maximum mass of NSs; however, this is quite model dependent. Under different SGRB central engine model assumptions, totally opposite conclusions could be drawn. If the SGRB originates from a BH central engine, as assumed in (Ruiz et al., 2018), the delay collapse has to occur within 1.7 s after the merger. Therefore, scenario 2) most likely occurred for the case of GW170817. As shown by previous studies (Breu and Rezzolla, 2016), the ratio between  $M_{\text{supra}}$  and  $M_{\text{TOV}}$  is almost universal for various NS EOS models, and the value is approximately 1.2. Combining the total mass of the merging binary, an upper limit (approximately 2.15–2.25  $M_{\odot}$  according to different studies, e.g., Rezzolla et al., 2018; Ruiz et al., 2018; Margalit and Metzger, 2017; Shibata et al., 2017) could then be obtained for the TOV maximum mass. In addition, it has been pointed out that the merger remnant might collapse to a BH with angular momentum smaller than that of the Keplerian limit due to angular momentum transfer by post-merger GW emission, neutrino and viscous effects, which leads to a different constraint on the TOV maximum mass. With this in mind, Shibata et al. (2019) performed an analysis by considering conservation laws of baryonic mass, energy and angular momentum, and the constraint on the TOV maximum mass is found to be  $2.10 M_{\odot} < M_{\text{TOV}} < 2.35 M_{\odot}$ . It is worth noting that this constraint is valid only under the BH central engine assumption. In fact, it has been pointed out that the multimessenger observation of GW170817 is consistent in a magnetar central engine model (Li et al., 2018b) and could even be favored by an X-ray activity detected very long time after the merger (Piro et al., 2019). In such a magnetar central engine model, in contrast, scenario 3) is favored, and hence, the upper limit of  $M_{\text{TOV}}$  mentioned before becomes a lower limit instead.

### 5.3. AT2017gfo and ejecta properties

It has long been suggested that the BNS merger is an important site for the production of heavy elements in the Universe (Eichler et al., 1989). R-process nucleosynthesis is expected to occur in the neutron-rich matter ejected during the merger. The radioactive decay of such neutron-rich isotopes could power a transient in optical/UV/IR, i.e., a kilonova (Li and Paczyński, 1998; Metzger et al., 2010). Such a transient event (AT2017gfo) was detected several hours after the merger time of GW170817 (Abbott et al., 2017e), the luminosity, spectrum and light curve of which are consistent with the prediction of the kilonova model. Such a kilonova detection not only enriches our knowledge about the abundance of heavy elements in the Universe but also greatly increases our understanding of NS EOSs.

The observational properties, for example, the peak luminosity and peak time, of the kilonova are closely related to the ejecta properties (cf. (Kasen et al., 2017)). The abundance of lanthanides (atomic numbers from 58 to 71) is strongly related to the electron fraction ( $Y_e$ ) of the ejecta. On the other hand, the opacity of the ejecta is mainly determined by the lanthanides in it, and is hence related to the electron fraction of the ejecta. The overall luminosity is related to the amount of radioactive heavy elements and thus the total mass of the ejecta. The ejecta is expanding at a certain velocity and becomes translucent after a period of time. Therefore, the characteristic duration of a kilonova is related to the velocity of the ejecta. To summarize, the mass, velocity and elec-

tron fraction of the ejecta are key parameters for understanding the observations of AT2017gfo.

The ejecta during a BNS merger mainly consists of two components. The first component is the so-called dynamic ejecta, which is normally more neutron-rich (lower  $Y_e$ ). Part of the dynamic ejecta is due to the tidal torque during the inspiral (Ruffert et al., 1997; Rosswog et al., 1999); hence, it has a lower temperature and very low  $Y_e$  (smaller than 0.1–0.2) and is spatially distributed in the equatorial plane of the binary. Another part of the dynamic ejecta results from shock during coalescence (also called shock-driven ejecta) (Oechslin et al., 2007; Hotokezaka et al., 2013). Due to the higher temperature at coalescence, this part of the dynamic ejecta normally has a slightly higher electron fraction ( $Y_e > 0.25$ ) (Wanajo et al., 2014; Sekiguchi et al., 2016) and can expand in the polar direction. In addition to the dynamic ejecta, the neutrino emissions from the remnant before collapsing to BH as well as the viscosity could further drive more ejecta (wind-driven ejecta) from the disc surrounding the remnant (Metzger et al., 2008a; Dessart et al., 2009; Fernández and Metzger, 2013). Due to neutrino irradiation, this part of the ejecta has a broader distribution of  $Y_e$ , which could be as high as 0.5 (Metzger and Fernández, 2014; Perego et al., 2014; Martin et al., 2015). Clearly, the amount of wind-driven ejecta is dependent on the lifetime of the remnant NS. For instance, in the case of a prompt collapse, the wind-driven ejecta could be significantly suppressed.

The kilonova observation following GW170817 has shown clear evidence of two distinct ejecta components (Cowperthwaite et al., 2017; Kasen et al., 2017; Tanaka et al., 2017),<sup>5</sup> an early rising ( $\sim 2$  days after the merger) and bluer component (which indicates a lower opacity and higher velocity) and a more extended redder component. The required amount of ejecta accounting for the “blue” component is approximately 0.01  $M_{\odot}$  with a relatively larger electron fraction  $Y_e > 0.25$  and velocity  $v^{\text{blue}} \sim 0.2 - 0.3c$ . For the red component observed at later times, in total, approximately 0.05  $M_{\odot}$  lanthanide-rich ( $Y_e < 0.25$ ) ejecta is needed, with a lower velocity of  $v^{\text{red}} \sim 0.1 - 0.2c$ . The inferred properties can be used to constrain the EOS of the merged NSs, although this constraint is quite model dependent.

One property we can use to constrain NS EOS models is the mass of the ejecta, as it is related to the properties of the merging binary. As summarized in (Radice et al., 2018b), stiffer EOS models (for which the tidal deformability is larger) typically have a smaller amount of tidal-induced dynamic ejecta than softer EOS models. However, softer EOSs normally eject more dynamic ejecta overall because of a more violent coalescence and hence eject more shock-driven ejecta. The amount of wind-driven ejecta depends on the lifetime of the merger remnant before collapsing to a BH, which is determined again by the  $M_{\text{TOV}}$  of the NS EOS. Ideally, the details of the ejecta property for BNS mergers with different EOS models could be determined through extensive numerical simulations. However, to fully resolve the wind-driven ejecta, a very long-term post-merger simulation with the implementation of viscosity and neutrino cooling is required, which is normally extremely time consuming and not affordable in practice. Nevertheless, conservative estimations can still be made. In (Radice et al., 2018a), it has been found that the total dynamic ejecta plus all the mass in the disc surrounding the remnant has a positive correlation with the  $\tilde{\Lambda}$  parameter of the binary. As not all the matter in the remnant disc is ejected, the dynamic ejecta plus the remnant disc mass has to be larger than the inferred mass of the ejecta to explain the observation of AT2017gfo, which is approximately 0.05 solar mass. This sets up a lower limit for the dynamic ejecta mass plus the

<sup>4</sup> Note that this possibility still remains for QSS, as discussed in (Lai et al., 2019).

<sup>5</sup> Note that there are studies arguing a model with 3 components (cf. (Perego et al., 2017)).

remnant disc mass and hence a lower limit for the binary tidal deformability. In (Radice et al., 2018a), this conservative constraint is  $\tilde{\Lambda} > 400$ . However, in the more systematic study of (Kiuchi et al., 2019), which employs a set of more general parameterized EOS and considers unequal-mass binaries, a contradiction was found. In other words, it was shown that a binary system with  $\tilde{\Lambda} < 400$  could still be consistent with the luminosity of AT2017gfo in terms of the ejecta mass. Therefore, this lower limit must be considered with caution.

Another implication of the observation of AT2017gfo is the fate of the merger remnant (the 4 scenarios mentioned in the previous subsection). This observed “blue” component of the ejecta clearly rules out the possibility of a prompt collapse, in which case there is a negligible amount of high  $Y_e$  shock-driven ejecta and wind-driven ejecta. In such a case, the kilonova observation should be dominated by the tidal ejecta and thus should be red. Distinguishing whether the remnant is long-lived is very uncertain and model dependent. In (Margalit and Metzger, 2017), it was suggested that if a long-lived SMNS is produced, then a significant amount of the rotational kinetic energy of the SMNS is injected into either a collimated relativistic jet or the ejecta within tens of seconds. This extra energy injection is considered to be inconsistent with the observations of GRB170817A and AT2017gfo. Therefore, the authors of (Margalit and Metzger, 2017) believe an HMNS or very short-lived SMNS is produced in the remnant and put a similar upper limit on  $M_{\text{TOV}}$  of  $2.17 M_{\odot}$ . Nevertheless, in (Li et al., 2018b), it was shown that with a long-lived SMNS as the merger remnant, both the early and late emission of AT2017gfo can be explained without requiring an unrealistically low opacity and high ejecta mass. Similar arguments can also be found in (Shibata et al., 2017). A long-lived SMNS remnant is believed to be able to provide strong neutrino emissions to reduce the lanthanide contamination in our line of sight as well as to produce enough ejecta with relatively high speed in the post-merger phase. Particularly, a temporal feature observed 155 d after the merger in the X-ray afterglow provides a more direct hint supporting a long-lived remnant. Considering the possibility of different merger outcomes, the allowed range for the TOV maximum mass for NSs could actually be larger (Ai et al., 2020).

#### 5.4. NS vs. QS in the multimessenger era

We have summarized some of the many studies on NS EOSs in light of GW170817 and its EM counterparts. Nevertheless, it is worth noting that the phase diagram of strong interactions at supranuclear densities is not yet clearly understood due to the nonperturbative nature of QCD at low energy scales. Apart from conventional NS models, other models involving strong interaction phase transitions are suggested, e.g., twin stars or strange stars (Alford et al., 2013; Drago et al., 2014; Alcock et al., 1986). As is summarized below, a binary quark star (BQS) scenario could be totally consistent with the observation of GW170817 and its EM counterparts. Due to the self-bound nature, QSs have a very large surface density. This leads to many significant differences between QSs and NSs. For example, when supported by uniform rotation, QSs can reach an even higher maximum mass with respect to their TOV maximum mass (40% more) than NSs (20% more) (Gondek-Rosińska et al., 2000). The finite surface density leads to a correction when calculating the tidal deformability (Postnikov et al., 2010; Takátsy and Kovács, 2020). QSs could reach a much higher  $T/|W|$  ratio when rotating, which could lead to more significant GW radiation in the post-merger phase (Zhou et al., 2018b). As a result, the above analysis on NS models should not be directly applied to QSs. It is interesting and useful to understand the constraints on QS models from what we have learned from GW170817

and its EM counterparts and how to distinguish between NS/QS models in the multimessenger era.

Qualitatively, the tidal deformability measurement constrains the stiffness of QSs, similar to the case of NSs. Stiffer EOSs normally reach higher  $M_{\text{TOV}}$  but also have larger tidal deformability than a softer EOS due to the larger size of the star described by a stiffer EOS. There is an overall positive correlation between  $M_{\text{TOV}}$  and  $\Lambda$  in NS models (Annala et al., 2018). Investigating QS properties based on the MIT bag model reveals a similar relation between  $M_{\text{TOV}}$  and  $\Lambda(1.4)$  (Zhou et al., 2018a). However, the quantitative results are quite different. In (Annala et al., 2018), creating NS EOS models stiff enough to reach  $M_{\text{TOV}} \sim 2.8 M_{\odot}$  with  $\Lambda(1.4) \leq 800$  was found to be impossible. In (Lai et al., 2019), it was shown that a self-bound strange star model can be stiff enough to reach  $M_{\text{TOV}} > 3 M_{\odot}$  without violating the tidal deformability constraint.

It was suggested that a BQS merger should result in a clean environment with little or no hadronic dynamic ejecta (Haensel et al., 1991). It is not easy to verify this argument with numerical simulations, as the density discontinuity on the QS surface is difficult to handle numerically. Nevertheless, in (Bauswein et al., 2009), several BQS merger simulations were performed with the SPH method, and it was shown that with some binary configurations, a BQS merger could eject a comparable amount of (quark) matter in the case of BNS mergers. According to (Alcock and Farhi, 1985; Madsen et al., 1986), under certain conditions (i.e., if the baryon number of an ejected quark nugget is smaller than a critical value), quark matter could efficiently evaporate into normal nucleon matter and contribute to the kilonova observation (Lai et al., 2018a; Paulucci et al., 2017). In addition, as uniformly rotating QSs can reach a higher maximum mass, the post-merger remnant is likely to be longer lived than the case of the BNS merger. It has been found that a magnetar with QS EOS as the post-merger remnant is better for understanding the internal X-ray plateau observations following SGRBs (Li et al., 2016c). In addition, both differentially rotating and uniformly rotating triaxial QSs are found to be sufficient GW emitters (Zhou et al., 2018b, 2019), which could be tested by future GW observations.

Another interesting possibility is a BNS merger that leads to a conversion of the merger remnant to a QS. In such a case, the inspiral GW signal and dynamic ejecta properties should be exactly the same as the case of a normal BNS merger, whereas the post-merger behavior could be quite different. On the one hand, if the phase transition occurs partially inside the star (i.e., only the high-density core part of the remnant), a softening of the EOS occurs, hence reducing the lifetime of the merger remnant as well as shifting the  $f_2$  peak in the post-merger GW signal to a higher frequency compared with those of the purely nucleonic merger remnant case (Bauswein et al., 2019; Weih et al., 2020). On the other hand, if the entire star could be converted to a QS after merger, which results in a stiffening of the EOS, the lifetime of the remnant is longer, and the  $f_2$  frequency is smaller (De Pietri et al., 2019). In this scenario, the time delay between the merger and the SGRB is believed to be the time needed for converting the surface of the remnant to quark matter, which significantly reduces the baryon load in the environment, thus helping the formation of a collimated jet (Drago et al., 2016).

Overall, the possibilities of a BQS merger or BNS merger with a QS remnant are consistent with the multimessenger observations of GW170817. However, current knowledge of the details of mergers involving QSs is quite limited. More simulations need to be performed for a better and more complete understanding in the future. With the help of numerical results and more future observations, whether QS could be involved or formed in a merger event could be distinguished, particularly according to the post-merger GW signals.

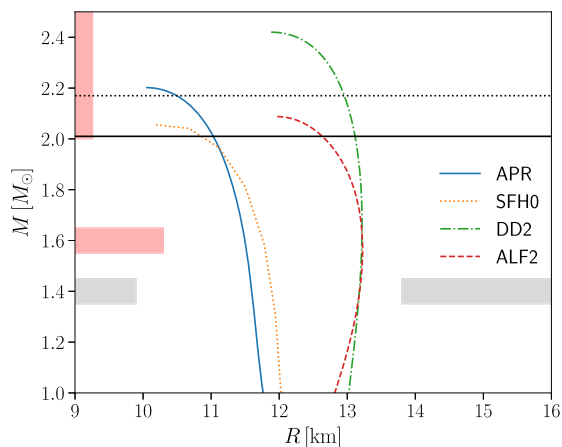


**Fig. 18.** The combined constraints on NS EOSs from the multimessenger observations of GW170817, GRB170817A and AT2017gfo. The gray shaded regions are excluded by the tidal deformability measurement of GW170817 (Abbott et al., 2017c; Annala et al., 2018). The red shaded regions are forbidden because the GRB170817A and AT2017gfo observations exclude a prompt collapse after merger (Bauswein et al., 2017). The solid horizontal line is the 2.01 solar mass lower limit for  $M_{\text{TOV}}$  according to the observation of the massive pulsar (Antoniadis et al., 2013), and the dotted horizontal line is the 2.17 solar mass constraint (Cromartie et al., 2020). Note that if the SGRB is powered by a BH central engine (or magnetar central engine), the dotted horizontal line is an upper limit (or lower limit). The M-R relation of several commonly used NS EOSs is shown in the figure.

### 5.5. Conclusion

To summarize, the multimessenger observation of BNS merger GW170817 has greatly increased our knowledge about the EOS of dense matter. The most robust constraint is from the tidal deformability encoded in the GW signal during the inspiral. Such a tidal deformability measurement could translate into a constraint on the radius of the NS at a given mass. The EM counterparts contain large amounts of information on the EOS models, the most reliable of which is to exclude the prompt collapse scenario. This provides independent constraints on the neutron star radius for a given mass. Other constraints on the lifetime of the remnant NS, however, depend on the central engine model of the SGRB and are not reliable. The constraints could be totally opposite in the BH central engine model and magnetar model, and the current observations could not reliably rule out either possibility for GW170817. We summarized all the constraints mentioned above, which is shown in Fig. 18. Nevertheless, GW170817 is just the beginning of the multimessenger era. As an increasing number of GW signals and EM counterparts from BNS mergers are detected in the future, our knowledge of NS and even QS EOS models will be enriched. In particular, if the time delay between the merger and the collapse to BH could be more robustly determined by future observations (either by post-merger GW signals or by more extensive EM counterpart observations), the TOV maximum mass can be crucially inferred, leading to a much better understanding of the EOS of dense neutron-rich matter.

## 6. Other opportunities from compact objects

### 6.1. Neutron star cooling

With the ever-increasing accuracy of observational instruments, more details of the signals emitted by NSs can be quantitatively monitored. Apart from the measurements of NS masses, radii and tidal deformabilities, high-density NS models can be confronted with the surface temperatures of isolated NSs of known or estimated ages and the thermal photon luminosity of the X-ray transients in quiescence with an estimated time-averaged accretion

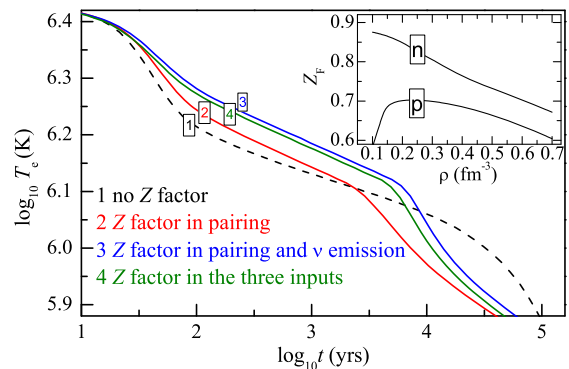


**Fig. 19.** Cooling curves of a canonically isolated NS within the minimal cooling paradigm (Page et al., 2004), without including fast neutrino emissions, charged meson condensate, hyperons, or confinement quarks in canonical NSs. The stellar structure is built with the APR EOS (Akmal et al., 1998). The calculations are carried out in three cases for a comparison: without any Z factors (the Fermi surface depletion due to the SRC), with Z factors only in superfluidity, with Z factors both in superfluidity and neutrino emission and with Z factors. Dong et al. (Dong et al., 2016) found that the SRC effect reduces the neutrino emissivity for the DU, MU, NNB and PBF processes, as well as the heat capacity of the stellar interior (Dong et al., 2016).

rate on the NS (Lattimer and Prakash, 2007; Yakovlev et al., 2001; Page and Reddy, 2006; Page et al., 2006; Potekhin et al., 2015). The NS EOS determines the stellar structure, as well as the effective masses and superfluid gaps of baryons, and is therefore crucial for the heat capacity and neutrino emission rate (e.g., Yakovlev et al., 2001; Li et al., 2016b; Shang et al., 2020).

In the Newtonian framework, the energy balance equation for NS cooling is written as (Page et al., 2006),

$$\frac{dE_{\text{th}}}{dt} = C_V \frac{dT}{dt} = -L_\nu - L_\gamma + H, \quad (58)$$

where  $T$  and  $C_V$  are the stellar internal temperature and the total heat capacity, respectively. The loss of the thermal energy  $E_{\text{th}}$  occurs through neutrino emission (total luminosity  $L_\nu$ ) and photon emission (total luminosity  $L_\gamma$ ).  $H$  represents all possible energy sources to heat the star, such as the decay of the magnetic field energy stored in stars. Current simulations of thermal evolution are usually based on a general relativistic formulation, and some robust codes have already been established,<sup>6</sup> which comprises all the relevant cooling reactions: direct URCA (DU) ( $n \rightarrow p + l + \bar{\nu}_l$ ,  $p + l \rightarrow n + \nu_l$ ), modified URCA (MU) ( $n + N \rightarrow p + N + l + \bar{\nu}_l$ ,  $p + N + l \rightarrow n + N + \nu_l$ ), nucleon-nucleon bremsstrahlung (NNB) ( $N + N \rightarrow N + N + \nu + \bar{\nu}$ ), Cooper pair breaking and formation (PBF) processes ( $N + N \rightarrow [NN] + \nu + \bar{\nu}$ ). Exemplary cooling curves of a 1.4  $M_\odot$  NS (Dong et al., 2016) are displayed in Fig. 19.

In the quiescent state of X-ray transients, the accreted matter sinks gradually in the interior of the NS and undergoes a series of nuclear reactions (Fortin et al., 2018). These reactions release some heat, which propagates into the whole NS, inwardly heating the core and outwardly emitted in the form of photons at the surface. This is the so-called deep crustal heating. The heating curves of X-ray transients can be derived, relating the  $L_\gamma$  in quiescence to the estimated time-averaged accretion rate  $\dot{M}$  (Yakovlev et al., 2003). The relevance of the pasta phase, which is beyond the neutron drip density, to explaining some X-ray transients (if confirmed) might be regarded as smoking-gun evidence of the NS model for pulsar-like objects (e.g., Deibel et al., 2017) and disfavors the alternative QS model.

Above all, a reliable theory for NS cooling, in combination with accurate observations, is indispensable for gaining important infor-

<sup>6</sup> <http://www.astroscu.unam.mx/neutrones/NSCool/>.

mation about the stellar interior. The complexity of NS systems, such as anisotropic magnetic fields and the compositions of the stellar core and envelope, is not controlled well theoretically, currently rendering the task of providing reliable and quantitative predictions extremely difficult, and considerable effort might be achieved in the future.

## 6.2. Pulsar glitch and glitch crisis

A glitch (sudden spin-up)<sup>7</sup> is a common phenomenon in pulsar observations and was discovered during pulsar timing studies in the Vela pulsar (Radhakrishnan and Manchester, 1969). Since then, the number of known glitches has greatly increased, with more than 560 glitches now known in more than 190 pulsars. The observed glitches are collected by the Jodrell Bank Observatory<sup>8</sup> and the ATNF Pulsar Catalogue.<sup>9</sup> During glitches, the pulsar angular velocity  $\Omega$  suddenly increases over a very short time and then usually relaxes to its preglitch rate over a longer time. The glitch size, often defined as the relative increase in the angular velocities during glitches,  $\Delta\Omega_g/\Omega$ , has a bimodal distribution ranging from  $\sim 10^{-10}$  to  $10^{-5}$  with peaks at  $\sim 10^{-9}$  and  $10^{-6}$  (Espinoza et al., 2011; Yu et al., 2013). The glitches in young pulsars, including magnetars, are generally large (Manchester, 2018). However, the youngest pulsars, e.g., the Crab pulsar, tend to have more frequent and smaller glitches. Various authors have used observed glitch properties as a probe to investigate the pulsar inner structure, i.e., the EOS of dense matter (Haskell and Melatos, 2015).

The physical mechanism behind glitches is suggested to be a sudden decrease in the NS moment of inertia, which could result from the coupling and decoupling between the (observed) charged component (rotating slower; labeled as index  $p$ ) and the superfluid component (rotating faster; labeled as index  $n$ ) (Anderson and Itoh, 1975). The fractional moment of inertia  $I_n/I_p$  is related to the glitch activity  $A_g = (1/T)(\sum \Delta\Omega_p)/\Omega_p$  as follows,

$$2\tau_c A_g \lesssim \frac{I_n}{I_p}, \quad (59)$$

where  $T$  is the total data span for glitch monitoring and  $\sum(\Delta\Omega_g)$  is the sum of all observed jumps.  $\tau_c = -\Omega_p/2\dot{\Omega}_p$  is the characteristic age of the pulsar. The glitch activity  $A_g$  can be estimated for systems that have exhibited at least two glitches of similar magnitude, like the Vela pulsar. The glitch observations from the Vela pulsar place a constraint on the fractional moment of inertia, which is  $I_n/I_p \gtrsim 1.6\%$  (Link et al., 1999; Andersson et al., 2012). It has been argued that “entrainment” of the neutron superfluid by the crystalline structure of the crust greatly reduces its mobility, increasing the lower limit from 1.6% to  $\sim 7\%$  and making it very difficult for the nuclear EOSs to fulfill with a normal  $M > 1.0 M_\odot$  NS (Andersson et al., 2012; Chamel, 2013; Li et al., 2016a). This is clearly shown in Fig. 20. Consequently, the unpinning of the crustal superfluid is insufficient to account for large glitches. This is the so-called glitch crisis problem. Other mechanisms, e.g., the unpinning of core superfluid neutrons, may be required. However, the mobility of superfluid neutrons is related to the effective neutron mass, which has been discussed actively in the literature. According to the calculation in Watanabe and Pethick (2017), the constraint for the fractional moment of inertia is  $I_c/I \geq 2.5 - 2.3\%$ . Then, an NS of  $M \lesssim 1.55 M_\odot$  NS would be acceptable, and there is no need to invoke the core superfluid.

<sup>7</sup> An “antiglitch”, i.e., an abrupt spin-down, has also been detected (Archibald et al., 2013).

<sup>8</sup> <http://www.jb.man.ac.uk/pulsar/glitches/gTable.html>.

<sup>9</sup> <http://www.atnf.csiro.au/research/pulsar/psrcat/glitchTbl.html>.

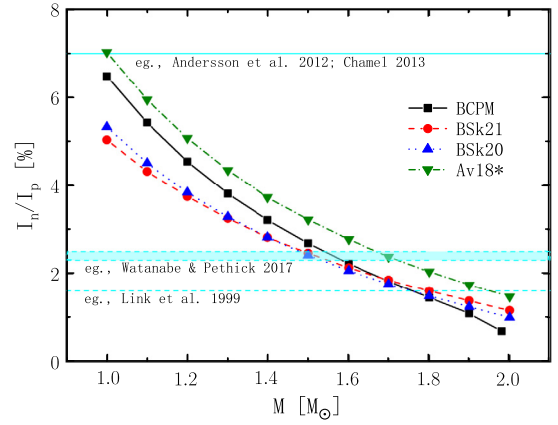


**Fig. 20.** Fractional moments of inertia as a function of the stellar mass for both the charged component  $I_p$  and the (crustal) superfluid component  $I_n$ , with four cases of NS EOSs (BCPM, BSk21, BSk20, Av18\*). Av18\* indicates the nonunified EOS of “Av18 + NV + BPS”. Taken from Li and Wang (2018).

However, this is an open problem, and more detailed work has to be done.

At present, we are still far from a thorough understanding of the general picture of glitches; for example, is there a connection between the stellar interior and the magnetosphere of a star? How can various types of post-glitch behavior be explained? Is there an alternative model besides the superfluid model? The original star-quake model (Baym et al., 1969) suggested that the change in the moment of inertia was due to relaxation in the NS (solid) crust to the current equilibrium oblateness but has difficulty explaining the large glitches observed from the Vela pulsar. In a solid star model, the whole body of the star, rather than only the crust, is in a solid state. In such cases, the glitch amplitude could be explained (Zhou et al., 2014; Lai et al., 2018b). It is a challenge to quantitatively describe glitch behaviors since the related physical processes are complicated. There has been progress in the determination of NS properties in the literature (e.g., Ho et al., 2015; Pizzochero et al., 2017; Ashton et al., 2019; Ge et al., 2019).

## 7. Summary and perspectives

Although NSs were anticipated in the early thirties and discovered as pulsars in the late sixties, the state of their liquid interiors remains unclear due to a lack of a good understanding of QCD at low energy scales. The current and upcoming multimessenger observatories (e.g., Wei et al., 2016; Özel et al., 2016; Li et al., 2018a,c; Ray et al., 2019; Watts et al., 2019) will continue improving the detection of pulsars together with the precise measurements of their masses and radii. Laboratory experiments will provide an emerging understanding of nuclear matter EOS and the transition to deconfined quark matter. Hopefully, the high density behavior of the NS EOS can be determined soon, shedding light on many unsolved problems in nuclear physics and high-energy astrophysics (e.g., Liu et al., 2017; Zhou et al., 2017; Yasin et al., 2018; Lau et al., 2019; Deng et al., 2020; Shen et al., 2020).

Since the compact star EOS is such a demanding problem, it is necessary to combine efforts from different communities and discuss mutual interests and problems (e.g., Capano et al., 2020; Zhang et al., 2018; Dietrich et al., 2020). Additionally, it is important to establish new quantitative results testable by experiments/observations. In this work, the microscopic physics of dense matter are modeled within the QMF, which connects the structure of a nucleon to the EOS of infinite nuclear matter, with a wide range of experimental and observational data available for use. The parameter space of the QMF has been constrained well for describing NSs, following the present robust measurements of mass,

radius, and tidal deformability. The pure NS maximum mass is approximately  $2.1 M_{\odot}$ , with a satisfying reproduction of the nuclear matter properties around the saturation density. The results have a modest dependence on the model parameters. Based on the available hypernuclei data, the hyperon puzzle is present, and we need to understand better how hyperon three-body interaction plays a role to understand more clearly whether hyperons are relevant in NSs (especially the heavy ones). The CSS parametrization allows us to handle the high-density cores of NSs in a model-independent way. After demonstrating how the NSs' mass and radius depend on the CSS parameters for the phase transition of deconfined quark matter, we find a safe upper limit for the hybrid star maximum mass at approximately  $3.6 M_{\odot}$  based on the extreme causality EOS, similar to previous studies. In particular, the NS/QS maximum mass is predicted to be approximately  $2.3 - 2.4 M_{\odot}$  from various model calculations, as well as analysis on the merger remnant of GW170817. Therefore, if more massive pulsars above  $2.4 M_{\odot}$  or fewer massive black holes below  $5 M_{\odot}$  are found, what is their nature? Is there a mass gap between NSs and black holes and why? Such problems are mysteries to be solved. The detailed feature of the sound speed in quark matter is explored in a perturbative model, and an enhancement in the sound speed is necessary to fulfill the 2-solar-mass constraint of pulsars, located at intermediate densities, indicating that the pair of quarks starts to play a nontrivial role at such densities. Quark superfluids should not be ignored in the quark matter relevant to compact stars. This is also consistent with that, in another MIT model, a superfluid QS is more consistent with a lower bound for tidal deformability of GW170817 than in the case without superfluid. In the future, even if we understand the stiffness of the EOS, a further challenge is the particle degree of freedom in cold, dense matter. This could help us understand the nonperturbative properties of low-energy QCD (or the parameters of an effective model). This is work for the future.

### Declaration of competing interest

The authors declare that they have no known competing financial interests or personal relationships that could have appeared to influence the work reported in this paper.

### Acknowledgments

We are grateful to the members of the XMU neutron star group. We are thankful to the anonymous referee for his or her beneficial comments and Hong Shen, Jirina Stone, Anthony Thomas for insightful discussions. This work was supported by the National Natural Science Foundation of China (Grant Nos. 11873040, 11775276, 11705163, and 11775119), the Youth Innovation Promotion Association of the Chinese Academy of Sciences, the Natural Science Foundation of Tianjin, the China Scholarship Council (Grant No. 201906205013), and the Ningbo Natural Science Foundation (Grant No. 2019A610066).

### References

Abbott, B.P., et al., 2017a. Estimating the contribution of dynamical ejecta in the kilonova associated with GW170817. *ApJ* 850 (2), L39.  
 Abbott, B.P., et al., 2017b. Exploring the sensitivity of next generation gravitational wave detectors. *CQGra* 34 (4), 044001.  
 Abbott, B.P., et al., 2017c. Gravitational waves and gamma-rays from a binary neutron star merger: GW170817 and GRB 170817A. *ApJ* 848 (2), L13.  
 Abbott, B.P., et al., 2017d. GW170817: observation of gravitational waves from a binary neutron star inspiral. *PhRvL* 119 (16), 161101.  
 Abbott, B.P., et al., 2017e. Multi-messenger observations of a binary neutron star merger. *ApJ* 848 (2), L12.  
 Abbott, B.P., et al., 2017f. Search for post-merger gravitational waves from the remnant of the binary neutron star merger GW170817. *ApJ* 851 (1), L16.  
 Abbott, B.P., et al., 2018. GW170817: measurements of neutron star radii and equation of state. *PhRvL* 121 (16), 161101.

Abbott, B.P., et al., 2019. Properties of the binary neutron star merger GW170817. *PhRvX* 9 (1), 011001.  
 Abbott, B.P., et al., 2020a. GW190425: observation of a compact binary coalescence with total mass  $\sim 3.4 M_{\odot}$ . *ApJ* 892 (1), L3.  
 Abbott, B.P., et al., 2020b. Model a comparison from LIGO-Virgo data on GW170817's binary components and consequences for the merger remnant. *CQGra* 37 (4), 045006.  
 Ai, S., Gao, H., Dai, Z.-G., Wu, X.-F., Li, A., Zhang, B., Li, M.-Z., 2018. The allowed parameter space of a long-lived neutron star as the merger remnant of GW170817. *ApJ* 860 (1), 57.  
 Ai, S., Gao, H., Zhang, B., 2020. What constraints on the neutron star maximum mass can one pose from GW170817 observations?. *ApJ* 893 (2), 14.  
 Akmal, A., Pandharipande, V.R., Ravenhall, D.G., 1998. Equation of state of nucleon matter and neutron star structure. *PhRvC* 58 (3), 1804–1828.  
 Alcock, C., Farhi, E., 1985. Evaporation of strange matter in the early Universe. *PhRvD* 32 (6), 1273–1279.  
 Alcock, C., Farhi, E., Olinto, A., 1986. Strange stars. *ApJ* 310, 261.  
 Alford, M., Rajagopal, K., Wilczek, F., 1999. Color-flavor locking and chiral symmetry breaking in high density QCD. *NuPhB* 537 (1), 443–458.  
 Alford, M., Braby, M., Paris, M., Reddy, S., 2005. Hybrid stars that masquerade as neutron stars. *ApJ* 629 (2), 969–978.  
 Alford, M., Schmitt, A., Rajagopal, K., Schäfer, T., 2008. Color superconductivity in dense quark matter. *RvMP* 80 (4), 1455–1515.  
 Alford, M., Han, S., Prakash, M., 2013. Generic conditions for stable hybrid stars. *PhRvD* 88 (8), 083013.  
 Alford, M., Burgio, G.F., Han, S., Taranto, G., Zappalà, D., 2015. Constraining and applying a generic high-density equation of state. *PhRvD* 92 (8), 083002.  
 Alford, M., Han, S., Schwenzer, K., 2019. Signatures for quark matter from multi-messenger observations. *JPhG* 46 (11), 114001.  
 Aloy, M.A., Ibáñez, J.M., Sanchis-Gual, N., Obergaulinger, M., Font, J.A., Serna, S., Marquina, A., 2019. Neutron star collapse and gravitational waves with a non-convex equation of state. *MNRAS* 484 (4), 4980–5008.  
 Alsing, J., Silva, H.O., Berti, E., 2018. Evidence for a maximum mass cut-off in the neutron star mass distribution and constraints on the equation of state. *MNRAS* 478 (1), 1377–1391.  
 Anderson, P.W., Itoh, N., 1975. Pulsar glitches and restlessness as a hard superfluidity phenomenon. *Natur* 256 (5512), 25–27.  
 Andersson, N., Kokkotas, K.D., 2001. The R-mode instability in rotating neutron stars. *IJMPD* 10 (4), 381–441.  
 Andersson, N., Glampedakis, K., Ho, W.C.G., Espinoza, C.M., 2012. Pulsar glitches: the crust is not enough. *PhRvL* 109 (24), 241103.  
 Angeli, I., Marinova, K.P., 2013. Table of experimental nuclear ground state charge radii: an update. *ADNDT* 99 (1), 69–95.  
 Annala, E., Gorda, T., Kurkela, A., Vuorinen, A., 2018. Gravitational-wave constraints on the neutron-star-matter equation of state. *PhRvL* 120 (17), 172703.  
 Antic, S., Stone, J.R., Thomas, A.W., 2019. Neutron stars from crust to core within the quark-meson coupling model. Preprint. arXiv:1912.03815.  
 Antoniadis, J., et al., 2013. A massive pulsar in a compact relativistic binary. *Sci* 340 (6131), 448.  
 Archibald, R.F., Kaspi, V.M., Ng, C.Y., Gourgouliatos, K.N., Tsang, D., Scholz, P., Beardmore, A.P., Gehrels, N., Kennea, J.A., 2013. An anti-glitch in a magnetar. *Natur* 497 (7451), 591–593.  
 Arrington, J., Sick, I., 2015. Evaluation of the proton charge radius from electron-proton scattering. *JPhChRD* 44 (3), 031204.  
 Arzoumanian, Z., et al., 2018. The NANOGrav 11-year data set: high-precision timing of 45 millisecond pulsars. *ApJS* 235 (2), 37.  
 Ashton, G., Lasky, P.D., Graber, V., Palfreyman, J., 2019. Rotational evolution of the Vela pulsar during the 2016 glitch. *NatAs* 3, 1143–1148.  
 Bailyn, C.D., Jain, R.K., Coppi, P., Orosz, J.A., 1998. The mass distribution of stellar black holes. *ApJ* 499 (1), 367–374.  
 Baiotti, L., 2019. Gravitational waves from neutron star mergers and their relation to the nuclear equation of state. *PrPNP* 109, 103714.  
 Baldo, M., 1999. Nuclear methods and the nuclear equation of state. In: Baldo, M. (Ed.), Series: International Review of Nuclear Physics, vol. 8. World Scientific Publishing Co. Pte. Ltd.  
 Baldo, M., Burgio, G.F., 2012. Properties of the nuclear medium. *RPPH* 75 (2), 026301.  
 Baldo, M., Burgio, G.F., 2016. The nuclear symmetry energy. *PrPNP* 91, 203–258.  
 Bauswein, A., Janka, H.T., Oechslin, R., Pagliara, G., Sagert, I., Schaffner-Bielich, J., Hohle, M.M., Neuhäuser, R., 2009. Mass ejection by strange star mergers and observational implications. *PhRvL* 103 (1), 011101.  
 Bauswein, A., Just, O., Janka, H.-T., Stergioulas, N., 2017. Neutron-star radius constraints from GW170817 and future detections. *ApJ* 850 (2), L34.  
 Bauswein, A., Bastian, N.-U.F., Blaschke, D.B., Chatziioannou, K., Clark, J.A., Fischer, T., Oertel, M., 2019. Identifying a first-order phase transition in neutron-star mergers through gravitational waves. *PhRvL* 122 (6), 061102.  
 Baym, G., Pethick, C., Pines, D., Ruderman, M., 1969. Spin up in neutron stars: the future of the Vela pulsar. *Natur* 224 (5222), 872–874.  
 Baym, G., Pethick, C., Sutherland, P., 1971. The ground state of matter at high densities: equation of state and stellar models. *ApJ* 170, 299.  
 Baym, G., Hatsuda, T., Kojo, T., Powell, P.D., Song, Y., Takatsuka, T., 2018. From hadrons to quarks in neutron stars: a review. *RPPH* 81 (5), 056902.

- Baym, G., Furusawa, S., Hatsuda, T., Kojo, T., Togashi, H., 2019. New neutron star equation of state with quark-hadron crossover. *ApJ* 885 (1), 42.
- Bedaque, P., Steiner, A.W., 2015. Sound velocity bound and neutron stars. *PhRvL* 114 (3), 031103.
- Bodmer, A.R., 1971. Collapsed nuclei. *PhRvD* 4 (6), 1601–1606.
- Bohr, H., Moszkowski, S.A., Panda, P.K., Providência, C., da Providência, J., 2016. QMC approach based on the Bogoliubov independent quark model of the nucleon. *IJMP* 25 (2), 1650007.
- Bombaci, I., 2017. The hyperon puzzle in neutron stars. In: Proceedings of the 12th International Conference on Hypernuclear and Strange Particle Physics, p. 101002.
- Brecher, K., Caporaso, G., 1976. Obese ‘neutron’ stars. *Natur* 259 (5542), 377–378.
- Breu, C., Rezzolla, L., 2016. Maximum mass, moment of inertia and compactness of relativistic stars. *MNRAS* 459 (1), 646–656.
- Buballa, M., 2005. NJL-model analysis of dense quark matter [review article]. *PhR* 407 (4–6), 205–376.
- Burgio, G.F., Fantina, A.F., 2018. Nuclear equation of state for compact stars and supernovae. *ASSL* 457, 255.
- Burgio, G.F., Baldo, M., Sahu, P.K., Santra, A.B., Schulze, H.J., 2002. Maximum mass of neutron stars with a quark core. *PhLB* 526 (1–2), 19–26.
- Burgio, G.F., Schulze, H.J., Weber, F., 2003. On the maximum rotational frequency of neutron and hybrid stars. *A&A* 408, 675–680.
- Burgio, G.F., Schulze, H.J., Li, A., 2011. Hyperon stars at finite temperature in the Brueckner theory. *PhRvC* 83 (2), 025804.
- Burgio, G.F., Drago, A., Pagliara, G., Schulze, H.J., Wei, J.B., 2018. Are small radii of compact stars ruled out by GW170817/AT2017gfo? *ApJ* 860 (2), 139.
- Capano, C.D., Tews, I., Brown, S.M., Margalit, B., De, S., Kumar, S., Brown, D.A., Krishnan, B., Reddy, S., 2020. Stringent constraints on neutron-star radii from multimessenger observations and nuclear theory. *NatAs*, 1–8.
- Chamel, N., 2013. Crustal entrainment and pulsar glitches. *PhRvL* 110 (1), 011101.
- Chamel, N., Haensel, P., 2008. Physics of neutron star crusts. *LRR* 11 (1), 10.
- Chatziioannou, K., Han, S., 2020. Studying strong phase transitions in neutron stars with gravitational waves. *PhRvD* 101 (4), 044019.
- Chirenti, C., Gold, R., Miller, M.C., 2017. Gravitational waves from F-modes excited by the inspiral of highly eccentric neutron star binaries. *ApJ* 837 (1), 67.
- Cook, G.B., Shapiro, S.L., Teukolsky, S.A., 1994. Rapidly rotating polytropes in general relativity. *ApJ* 422, 227.
- Cowperthwaite, P.S., et al., 2017. The electromagnetic counterpart of the binary neutron star merger LIGO/Virgo GW170817. II. UV, optical, and near-infrared light curves and a comparison to kilonova models. *ApJ* 848 (2), L17.
- Cromartie, H.T., et al., 2020. Relativistic Shapiro delay measurements of an extremely massive millisecond pulsar. *NatAs* 4, 72–76.
- Dai, Z.G., Wang, X.Y., Wu, X.F., Zhang, B., 2006. X-ray flares from postmerger millisecond pulsars. *Sci* 311 (5764), 1127–1129.
- Damour, T., Nagar, A., 2009. Relativistic tidal properties of neutron stars. *PhRvD* 80 (8), 084035.
- Danielewicz, P., Lee, J., 2014. Symmetry energy II: isobaric analog states. *NuPhA* 922, 1–70.
- Danielewicz, P., Lacey, R., Lynch, W.G., 2002. Determination of the equation of state of dense matter. *Sci* 298 (5598), 1592–1596.
- Das, H.C., Kumar, A., Kumar, B., Biswal, S.K., Nakatsukasa, T., Li, A., Patra, S.K., 2020. Effects of dark matter on nuclear and neutron star matter. *MNRAS* 495 (4), 4893–4903.
- De Pietri, R., Drago, A., Feo, A., Pagliara, G., Pasquali, M., Traversi, S., Wiktorowicz, G., 2019. Merger of compact stars in the two-families scenario. *ApJ* 881 (2), 122.
- De, S., Finstad, D., Lattimer, J.M., Brown, D.A., Berger, E., Biwer, C.M., 2018. Tidal deformabilities and radii of neutron stars from the observation of GW170817. *PhRvL* 121 (9), 091102.
- Degrand, T., Jaffe, R.L., Johnson, K., Kiskis, J., 1975. Masses and other parameters of the light hadrons. *PhRvD* 12 (7), 2060–2076.
- Deibel, A., Cumming, A., Brown, E.F., Reddy, S., 2017. Late-time cooling of neutron star transients and the physics of the inner crust. *ApJ* 839 (2), 95.
- Demorest, P.B., Pennucci, T., Ransom, S.M., Roberts, M.S.E., Hessels, J.W.T., 2010. A two-solar-mass neutron star measured using Shapiro delay. *Natur* 467 (7319), 1081–1083.
- Deng, Z.-L., Gao, Z.-F., Li, X.-D., Shao, Y., 2020. On the formation of PSR J1640+2224: a neutron star born massive? *ApJ* 892 (1), 4.
- Dessart, L., Ott, C.D., Burrows, A., Rosswog, S., Livne, E., 2009. Neutrino signatures and the neutrino-driven wind in binary neutron star mergers. *ApJ* 690 (2), 1681–1705.
- Dietrich, T., Coughlin, M.W., Pang, P.T.H., Bulla, M., Heinzl, J., Issa, L., Tews, I., Antier, S., 2020. New constraints on the supranuclear equation of state and the Hubble constant from nuclear physics – multi-messenger astronomy. Preprint. arXiv:2002.11355.
- Dong, J.M., Lombardo, U., Zhang, H.F., Zuo, W., 2016. Role of nucleonic Fermi surface depletion in neutron star cooling. *ApJ* 817 (1), 6.
- Douchin, F., Haensel, P., 2001. A unified equation of state of dense matter and neutron star structure. *A&A* 380, 151–167.
- Drago, A., Pagliara, G., 2018. Merger of two neutron stars: predictions from the two-families scenario. *ApJ* 852 (2), L32.
- Drago, A., Lavagno, A., Pagliara, G., 2014. Can very compact and very massive neutron stars both exist? *PhRvD* 89 (4), 043014.
- Drago, A., Lavagno, A., Metzger, B.D., Pagliara, G., 2016. Quark deconfinement and the duration of short gamma-ray bursts. *PhRvD* 93 (10), 103001.
- Dutra, M., Lourenço, O., Sá Martins, J.S., Delfino, A., Stone, J.R., Stevenson, P.D., 2012. Skyrmion interaction and nuclear matter constraints. *PhRvC* 85 (3), 035201.
- Dutra, M., Lourenço, O., Avancini, S.S., Carlson, B.V., Delfino, A., Menezes, D.P., Providência, C., Typel, S., Stone, J.R., 2014. Relativistic mean-field hadronic models under nuclear matter constraints. *PhRvC* 90 (5), 055203.
- Eichler, D., Livio, M., Piran, T., Schramm, D.N., 1989. Nucleosynthesis, neutrino bursts and  $\gamma$ -rays from coalescing neutron stars. *Natur* 340 (6229), 126–128.
- Espinoza, C.M., Lyne, A.G., Stappers, B.W., Kramer, M., 2011. A study of 315 glitches in the rotation of 102 pulsars. *MNRAS* 414 (2), 1679–1704.
- Essick, R., Landry, P., Holz, D.E., 2020. Nonparametric inference of neutron star composition, equation of state, and maximum mass with GW170817. *PhRvD* 101 (6), 063007.
- Fantina, A.F., Chamel, N., Pearson, J.M., Goriely, S., 2013. Neutron star properties with unified equations of state of dense matter. *A&A* 559, A128.
- Farr, W.M., Sravan, N., Cantrell, A., Kreidberg, L., Bailyn, C.D., Mandel, I., Kalogera, V., 2011. The mass distribution of stellar-mass black holes. *ApJ* 741 (2), 103.
- Fattoyev, F.J., Piekarewicz, J., Horowitz, C.J., 2018. Neutron skins and neutron stars in the multimessenger era. *PhRvL* 120 (17), 172702.
- Feliciello, A., Nagae, T., 2015. Experimental review of hypernuclear physics: recent achievements and future perspectives. *RPPH* 78 (9), 096301.
- Fernández, R., Metzger, B.D., 2013. Delayed outflows from black hole accretion tori following neutron star binary coalescence. *MNRAS* 435 (1), 502–517.
- Ferreira, M., Fortin, M., Malik, T., Agrawal, B.K., Providência, C., 2020. Empirical constraints on the high-density equation of state from multimessenger observables. *PhRvD* 101 (4), 043021.
- Fischer, T., Wu, M.-R., Wehmeyer, B., Bastian, N.-U.F., Martínez-Pinedo, G., Thielemann, F.-K., 2020. Core-collapse supernova explosions driven by the hadron-quark phase transition as rare  $r$  process site. *ApJ* 894 (1), 9.
- Flanagan, É.É., Hinderer, T., 2008. Constraining neutron-star tidal Love numbers with gravitational-wave detectors. *PhRvD* 77 (2), 021502.
- Fonseca, E., et al., 2016. The NANOGrav nine-year data set: mass and geometric measurements of binary millisecond pulsars. *ApJ* 832 (2), 167.
- Fortin, M., Providência, C., Raduta, A.R., Gulminelli, F., Zdunik, J.L., Haensel, P., Bejger, M., 2016. Neutron star radii and crusts: uncertainties and unified equations of state. *PhRvC* 94 (3), 035804.
- Fortin, M., Taranto, G., Burgio, G.F., Haensel, P., Schulze, H.J., Zdunik, J.L., 2018. Thermal states of neutron stars with a consistent model of interior. *MNRAS* 475 (4), 5010–5022.
- Fraga, E.S., Romatschke, P., 2005. Role of quark mass in cold and dense perturbative QCD. *PhRvD* 71 (10), 105014.
- Fraga, E.S., Piasarowski, R.D., Schaffner-Bielich, J., 2001. Small, dense quark stars from perturbative QCD. *PhRvD* 63 (12), 121702.
- Gal, A., Hungerford, E.V., Millener, D.J., 2016. Strangeness in nuclear physics. *RvMP* 88 (3), 035004.
- Gandolfi, S., Lonardonì, D., Lovato, A., Piarulli, M., 2020. Atomic nuclei from quantum Monte Carlo calculations with chiral EFT interactions. *FrPhy* 8, 117.
- Gao, H., Zhang, B., Lü, H.-J., 2016. Constraints on binary neutron star merger product from short GRB observations. *PhRvD* 93 (4), 044065.
- Gao, H., Ai, S.-K., Cao, Z.-J., Zhang, B., Zhu, Z.-Y., Li, A., Zhang, N.-B., Bauswein, A., 2020. Relation between gravitational mass and baryonic mass for non-rotating and rapidly rotating neutron stars. *FrPhy* 15 (2), 24603.
- Ge, M.Y., Lu, F.J., Yan, L.L., Weng, S.S., Zhang, S.N., Wang, Q.D., Wang, L.J., Li, Z.J., Zhang, W., 2019. The brightening of the pulsar wind nebula of PSR B0540–69 after its spin-down-rate transition. *NatAs* 3, 1122–1127.
- Glendenning, N.K., 1990. Fast pulsars, strange stars: AN opportunity in radio astronomy. *MPLA* 5 (27), 2197–2207.
- Glendenning, N.K., 1992. First-order phase transitions with more than one conserved charge: consequences for neutron stars. *PhRvD* 46 (4), 1274–1287.
- Glendenning, N.K., Moszkowski, S.A., 1991. Reconciliation of neutron-star masses and binding of the Lambda in hypernuclei. *PhRvL* 67, 2414–2417.
- Gomes, R.O., Char, P., Schramm, S., 2019. Constraining strangeness in dense matter with GW170817. *ApJ* 877 (2), 139.
- Gondek-Rosińska, D., Bulik, T., Zdunik, L., Gourgoulhon, E., Ray, S., Dey, J., Dey, M., 2000. Rapidly rotating compact strange stars. *A&A* 363, 1005–1012.
- Graber, V., Andersson, N., Hogg, M., 2017. Neutron stars in the laboratory. *IJMPD* 26 (8), 1730015.
- Guichon, P.A.M., 1988. A possible quark mechanism for the saturation of nuclear matter. *PhLB* 200 (3), 235–240.
- Guichon, P.A.M., Stone, J.R., Thomas, A.W., 2018. Quark-Meson-Coupling (QMC) model for finite nuclei, nuclear matter and beyond. *PrPNP* 100, 262–297.
- Güven, H., Bozkurt, K., Khan, E., Margueron, J., 2020. Multi-messenger and multi-physics Bayesian inference for GW170817 binary neutron star merger. *PhRvC* 102 (1), 015805.
- Haensel, P., Zdunik, J.L., 2008. Models of crustal heating in accreting neutron stars. *A&A* 480 (2), 459–464.
- Haensel, P., Zdunik, J.L., Schaefer, R., 1986. Strange quark stars. *A&A* 160 (1), 121–128.

- Haensel, P., Paczynski, B., Amsterdamski, P., 1991. Gamma-ray bursts from colliding strange stars. *ApJ* 375, 209.
- Haensel, P., Zdunik, J.L., Bejger, M., Lattimer, J.M., 2009. Keplerian frequency of uniformly rotating neutron stars and strange stars. *A&A* 502 (2), 605–610.
- Haidenbauer, J., Meißner, U.G., Kaiser, N., Weise, W., 2017. Lambda-nuclear interactions and hyperon puzzle in neutron stars. *EPJA* 53 (6), 121.
- Han, S., Steiner, A.W., 2019. Tidal deformability with sharp phase transitions in binary neutron stars. *PhRvD* 99 (8), 083014.
- Han, S., Mamun, M.A.A., Lalit, S., Constantinou, C., Prakash, M., 2019. Treating quarks within neutron stars. *PhRvD* 100 (10), 103022.
- Haskell, B., Melatos, A., 2015. Models of pulsar glitches. *IJMPD* 24 (3), 1530008.
- Haskell, B., Ciolfi, R., Pannarale, F., Rezzolla, L., 2014. On the universality of I-Love-Q relations in magnetized neutron stars. *MNRAS* 438 (1), L71–L75.
- Hebeler, K., Lattimer, J.M., Pethick, C.J., Schwenk, A., 2013. Equation of state and neutron star properties constrained by nuclear physics and observation. *ApJ* 773 (1), 11.
- Hessels, J.W.T., Ransom, S.M., Stairs, I.H., Freire, P.C.C., Kaspi, V.M., Camilo, F., 2006. A radio pulsar spinning at 716 Hz. *Sci* 311 (5769), 1901–1904.
- Hinderer, T., 2008. Tidal Love numbers of neutron stars. *ApJ* 677 (2), 1216–1220.
- Ho, W.C.G., Espinoza, C.M., Antonopoulou, D., Andersson, N., 2015. Pinning down the superfluid and measuring masses using pulsar glitches. *SciA* 1 (9), e1500578.
- Hornick, N., Tolos, L., Zacchi, A., Christian, J.-E., Schaffner-Bielich, J., 2018. Relativistic parameterizations of neutron matter and implications for neutron stars. *PhRvC* 98 (6), 065804.
- Horowitz, C.J., Piekarewicz, J., 2001. Neutron star structure and the neutron radius of  $^{208}\text{Pb}$ . *PhRvL* 86 (25), 5647–5650.
- Hotokezaka, K., Kiuchi, K., Kyutoku, K., Okawa, H., Sekiguchi, Y.-i., Shibata, M., Taniguchi, K., 2013. Mass ejection from the merger of binary neutron stars. *PhRvD* 87 (2), 024001.
- Hu, J., Shen, H., 2017. Single- $\Xi^-$  hypernuclei within a quark mean-field model. *PhRvC* 96 (5), 054304.
- Hu, J.N., Li, A., Shen, H., Toki, H., 2014a. Quark mean-field model for single and double  $\Lambda$  and  $\Xi$  hypernuclei. *PTEP* 2014 (1), 013D02.
- Hu, J.N., Li, A., Toki, H., Zuo, W., 2014b. Extended quark mean-field model for neutron stars. *PhRvC* 89 (2), 025802.
- Isgur, N., Karl, G., 1978. P-wave baryons in the quark model. *PhRvD* 18 (11), 4187–4205.
- Kalogera, V., Baym, G., 1996. The maximum mass of a neutron star. *ApJ* 470, L61.
- Kasen, D., Metzger, B., Barnes, J., Quataert, E., Ramirez-Ruiz, E., 2017. Origin of the heavy elements in binary neutron-star mergers from a gravitational-wave event. *Natur* 551 (7678), 80–84.
- Khaustov, P., et al., 2000. Evidence of  $\Xi$  hypernuclear production in the  $^{12}\text{C}(K^-, K^+)^{12}_{\Xi}\text{Be}$  reaction. *PhRvC* 61 (5), 054603.
- Kiuchi, K., Kyutoku, K., Shibata, M., Taniguchi, K., 2019. Revisiting the lower bound on tidal deformability derived by AT 2017gfo. *ApJ* 876 (2), L31.
- Komatsu, H., Eriguchi, Y., Hachisu, I., 1989. Rapidly rotating general relativistic stars. I - Numerical method and its application to uniformly rotating polytropes. *MNRAS* 237, 355–379.
- Kreidberg, L., Bailyn, C.D., Farr, W.M., Kalogera, V., 2012. Mass measurements of black holes in X-ray transients: is there a mass gap? *ApJ* 757 (1), 36.
- Kurkela, A., Romatschke, P., Vuorinen, A., 2010. Cold quark matter. *PhRvD* 81 (10), 105021.
- Kurkela, A., Fraga, E.S., Schaffner-Bielich, J., Vuorinen, A., 2014. Constraining neutron star matter with quantum chromodynamics. *ApJ* 789 (2), 127.
- Lai, X., Zhou, E., Xu, R., 2019. Strangeons constitute bulk strong matter: test using GW 170817. *EPJA* 55 (4), 60.
- Lai, X.-Y., Yu, Y.-W., Zhou, E.-P., Li, Y.-Y., Xu, R.-X., 2018a. Merging strangeon stars. *RAA* 18 (2), 024.
- Lai, X.-Y., Yun, C.A., Lu, J.G., Lü, G.L., Wang, Z.J., Xu, R.X., 2018b. Pulsar glitches in a strangeon star model. *MNRAS* 476 (3), 3303–3309.
- Lattimer, J.M., 2012. The nuclear equation of state and neutron star masses. *ARNPS* 62 (1), 485–515.
- Lattimer, J.M., Prakash, M., 2004. The physics of neutron stars. *Sci* 304 (5670), 536–542.
- Lattimer, J.M., Prakash, M., 2007. Neutron star observations: prognosis for equation of state constraints. *PhR* 442 (1–6), 109–165.
- Lau, S.Y., Leung, P.T., Lin, L.M., 2019. Two-layer compact stars with crystalline quark matter: screening effect on the tidal deformability. *PhRvD* 99 (2), 023018.
- Lawrence, S., Tervala, J.G., Bedaque, P.F., Miller, M.C., 2015. An upper bound on neutron star masses from models of short gamma-ray bursts. *ApJ* 808 (2), 186.
- Li, A., 2015. Glitch crisis or not: a microscopic study. *ChPhL* 32 (7), 079701.
- Li, A., Liu, T., 2013. Revisiting the hot matter in the center of gamma-ray bursts and supernovae. *A&A* 555, A129.
- Li, A., Wang, R., 2018. Pulsar glitch and nuclear EoS: applicability of superfluid model. In: *Weltvrede, P., Perera, B.B.P., Preston, L.L., Sanidas, S. (Eds.), IAU, vol. 337, p. 360.*
- Li, A., Burgio, G.F., Lombardo, U., Zuo, W., 2006. Microscopic three-body forces and kaon condensation in cold neutrino-trapped matter. *PhRvC* 74 (5), 055801.
- Li, A., Zuo, W., Mi, A.-J., Burgio, G., 2007. Hyperon-hyperon interaction in relativistic mean field model. *ChPhL* 16 (7), 1934–1940.
- Li, A., Burgio, G.F., Lombardo, U., Peng, G.X., 2008a. Exotic phases in neutron stars. *IJMPD* 17 (9), 1635–1647.
- Li, A., Jiang, J.L., Tang, S.P., Miao, Z.Q., Zhou, E.P., Xu, R.X., 2020. Constraints from LIGO/Virgo and NICER on quark star equation of state. Preprint. arXiv:2009.12571.
- Li, A., Zuo, W., Schulze, J.H., Lombardo, U., 2008b. Hot nuclear matter equation of state and finite temperature kaon condensation. *ChPhL* 25 (12), 4233–4236.
- Li, A., Peng, G.-X., Lombardo, U., 2009. Deconfinement phase transition in neutron star matter. *ChPhC* 33 (S1), 61–63.
- Li, A., Xu, R.-X., Lu, J.-F., 2010a. Strange stars with different quark mass scalings. *MNRAS* 402 (4), 2715–2719.
- Li, A., Zhou, X.R., Burgio, G.F., Schulze, H.J., 2010b. Protoneutron stars in the Brueckner-Hartree-Fock approach and finite-temperature kaon condensation. *PhRvC* 81 (2), 025806.
- Li, A., Peng, G.-X., Lu, J.-F., 2011. Strange star candidates revised within a quark model with chiral mass scaling. *RAA* 11 (4), 482–490.
- Li, A., Huang, F., Xu, R.-X., 2012. Too massive neutron stars: the role of dark matter? *Aph* 37, 70–74.
- Li, A., Liu, T., Gubler, P., Xu, R.-X., 2015a. Revisiting the boiling of primordial quark nuggets at nonzero chemical potential. *Aph* 62, 115–121.
- Li, A., Zuo, W., Peng, G.X., 2015b. Massive hybrid stars with a first-order phase transition. *PhRvC* 91 (3), 035803.
- Li, A., Dong, J.M., Wang, J.B., Xu, R.X., 2016a. Structures of the vela pulsar and the glitch crisis from the Brueckner theory. *ApJS* 223 (1), 16.
- Li, A., Hu, J.N., Shang, X.L., Zuo, W., 2016b. Nonrelativistic nucleon effective masses in nuclear matter: Brueckner-Hartree-Fock model versus relativistic Hartree-Fock model. *PhRvC* 93 (1), 015803.
- Li, A., Zhang, B., Zhang, N.-B., Gao, H., Qi, B., Liu, T., 2016c. Internal x-ray plateau in short GRBs: signature of supramassive fast-rotating quark stars? *PhRvD* 94 (8), 083010.
- Li, A., Zhu, Z.-Y., Zhou, X., 2017. New equations of state for postmerger supramassive quark stars. *ApJ* 844 (1), 41.
- Li, B.-A., Chen, L.-W., Ko, C.M., 2008. Recent progress and new challenges in isospin physics with heavy-ion reactions. *PhR* 464 (4–6), 113–281.
- Li, B.-A., Ramos, A., Verde, G., Vidiña, I., 2014. Topical issue on nuclear symmetry energy. *EPJA* 50.
- Li, L.-X., Paczyński, B., 1998. Transient events from neutron star mergers. *ApJ* 507 (1), L59–L62.
- Li, D., et al., 2018a. FAST in space: considerations for a multibeam, multipurpose survey using China's 500-m aperture spherical radio telescope (FAST). *IMMag* 19 (3), 112–119.
- Li, S.-Z., Liu, L.-D., Yu, Y.-W., Zhang, B., 2018b. What powered the optical transient AT2017gfo associated with GW170817? *ApJ* 861 (2), L12.
- Li, T., et al., 2018c. Insight-HXMT observations of the first binary neutron star merger GW170817. *SCPMA* 61 (3), 31011.
- Lim, Y., Holt, J.W., 2018. Neutron star tidal deformabilities constrained by nuclear theory and experiment. *PhRvL* 121 (6), 062701.
- Link, B., Epstein, R.I., Lattimer, J.M., 1999. Pulsar constraints on neutron star structure and equation of state. *PhRvL* 83 (17), 3362–3365.
- Liu, T., Lin, C.-Y., Song, C.-Y., Li, A., 2017. A comparison of gravitational waves from central engines of gamma-ray bursts: neutrino-dominated accretion flows, Blandford-Znajek mechanisms, and millisecond magnetars. *ApJ* 850 (1), 30.
- Logoteta, D., Vidiña, I., Bombaci, I., 2019. Impact of chiral hyperonic three-body forces on neutron stars. *EPJA* 55 (11), 207.
- Lonardonì, D., Lovato, A., Gandolfi, S., Pederiva, F., 2015. Hyperon puzzle: hints from quantum Monte Carlo calculations. *PhRvL* 114 (9), 092301.
- Lourenço, O., Bhuyan, M., Lenzi, C.H., Dutra, M., Gonzalez-Boquera, C., Centelles, M., Viñas, X., 2020a. GW170817 constraints analyzed with Gogny forces and momentum-dependent interactions. *PhLB* 803, 135306.
- Lourenço, O., Dutra, M., Lenzi, C.H., Biswal, S.K., Bhuyan, M., Menezes, D.P., 2020b. Consistent Skyrme parametrizations constrained by GW170817. *EPJA* 56 (2), 32.
- Ma, P.-X., Jiang, J.-L., Wang, H., Jin, Z.-P., Fan, Y.-Z., Wei, D.-M., 2018. GW170817 and the prospect of forming supramassive remnants in neutron star mergers. *ApJ* 858 (2), 74.
- Madsen, J., Heiselberg, H., Riisager, K., 1986. Does strange matter evaporate in the early Universe? *PhRvD* 34 (10), 2947–2955.
- Maieron, C., Baldo, M., Burgio, G.F., Schulze, H.J., 2004. Hybrid stars with the color dielectric and the MIT bag models. *PhRvD* 70 (4), 043010.
- Malik, T., Alam, N., Fortin, M., Providência, C., Agrawal, B.K., Jha, T.K., Kumar, B., Patra, S.K., 2018. GW170817: constraining the nuclear matter equation of state from the neutron star tidal deformability. *PhRvC* 98 (3), 035804.
- Manchester, R.N., 2018. Pulsar glitches and their impact on neutron-star astrophysics. Preprint. arXiv:1801.04332.
- Margalit, B., Metzger, B.D., 2017. Constraining the maximum mass of neutron stars from multi-messenger observations of GW170817. *ApJ* 850 (2), L19.
- Martin, D., Perego, A., Arcones, A., Thielemann, F.K., Korobkin, O., Rosswog, S., 2015. Neutrino-driven winds in the aftermath of a neutron star merger: nucleosynthesis and electromagnetic transients. *ApJ* 813 (1), 2.
- Maruyama, T., Chiba, S., Schulze, H.-J., Tatsumi, T., 2007. Hadron-quark mixed phase in hyperon stars. *PhRvD* 76 (12), 123015.

- McLerran, L., Reddy, S., 2019. Quarkyonic matter and neutron stars. *PhRvL* 122 (12), 122701.
- Metzger, B.D., Fernández, R., 2014. Red or blue? A potential kilonova imprint of the delay until black hole formation following a neutron star merger. *MNRAS* 441 (4), 3444–3453.
- Metzger, B.D., Piro, A.L., Quataert, E., 2008a. Time-dependent models of accretion discs formed from compact object mergers. *MNRAS* 390 (2), 781–797.
- Metzger, B.D., Quataert, E., Thompson, T.A., 2008b. Short-duration gamma-ray bursts with extended emission from protomagnetar spin-down. *MNRAS* 385 (3), 1455–1460.
- Metzger, B.D., et al., 2010. Electromagnetic counterparts of compact object mergers powered by the radioactive decay of r-process nuclei. *MNRAS* 406 (4), 2650–2662.
- Miao, Z.Q., Li, A., Zhu, Z.Y., Han, S., 2020. Constraining hadron-quark phase transition parameters within the quark-mean-field model using multi-messenger observations of neutron stars. Preprint. arXiv:2006.00839.
- Miller, M.C., et al., 2019. PSR J0030+0451 mass and radius from NICER data and implications for the properties of neutron star matter. *ApJ* 887 (1), L24.
- Mohr, P.J., Newell, D.B., Taylor, B.N., 2016. CODATA recommended values of the fundamental physical constants: 2014. *RvMP* 88 (3), 035009.
- Montaña, G., Tolós, L., Hanauske, M., Rezzolla, L., 2019. Constraining twin stars with GW170817. *PhRvD* 99 (10), 103009.
- Most, E.R., Weih, L.R., Rezzolla, L., Schaffner-Bielich, J., 2018. New constraints on radii and tidal deformabilities of neutron stars from GW170817. *PhRvL* 120 (26), 261103.
- Most, E.R., Papenfort, L.J., Dexheimer, V., Hanauske, M., Schramm, S., Stöcker, H., Rezzolla, L., 2019. Signatures of quark-hadron phase transitions in general-relativistic neutron-star mergers. *PhRvL* 122 (6), 061101.
- Motta, T.F., Kalaitzis, A.M., Antić, S., Guichon, P.A.M., Stone, J.R., Thomas, A.W., 2019. Isovector effects in neutron stars, radii, and the GW170817 constraint. *ApJ* 878 (2), 159.
- Motta, T.F., Thomas, A.W., Guichon, P.A.M., 2020. Do Delta baryons play a role in neutron stars? *PhLB* 802, 135266.
- Murguía-Berthier, A., Montes, G., Ramirez-Ruiz, E., De Colle, F., Lee, W.H., 2014. Necessary conditions for short gamma-ray burst production in binary neutron star mergers. *ApJ* 788 (1), L8.
- Nandi, R., Char, P., 2018. Hybrid stars in the light of GW170817. *ApJ* 857 (1), 12.
- Narayan, R., Paczynski, B., Piran, T., 1992. Gamma-ray bursts as the death throes of massive binary stars. *ApJ* 395, L83.
- Negele, J.W., Vautherin, D., 1973. Neutron star matter at sub-nuclear densities. *NuPhA* 207 (2), 298–320.
- Nikšić, T., Vretenar, D., Ring, P., 2011. Relativistic nuclear energy density functionals: mean-field and beyond. *PrPNP* 66 (3), 519–548.
- Nunna, K.P., Banik, S., Chatterjee, D., 2020. Signatures of strangeness in neutron star merger remnants. *ApJ* 896 (2), 109.
- Oechslin, R., Janka, H.T., Marek, A., 2007. Relativistic neutron star merger simulations with non-zero temperature equations of state. I. Variation of binary parameters and equation of state. *A&A* 467 (2), 395–409.
- Oertel, M., Hempel, M., Klähn, T., Typel, S., 2017. Equations of state for supernovae and compact stars. *RvMP* 89 (1), 015007.
- Olive, K.A., Particle Data Group, 2014. Review of particle physics. *ChPhC* 38 (9), 090001.
- Oppenheimer, J.R., Volkoff, G.M., 1939. On massive neutron cores. *PhRv* 55 (4), 374–381.
- Özel, F., Freire, P., 2016. Masses, radii, and the equation of state of neutron stars. *ARA&A* 54, 401–440.
- Özel, F., Psaltis, D., Narayan, R., McClintock, J.E., 2010. The black hole mass distribution in the galaxy. *ApJ* 725 (2), 1918–1927.
- Özel, F., Psaltis, D., Arzoumanian, Z., Morsink, S., Bauböck, M., 2016. Measuring neutron star radii via pulse profile modeling with NICER. *ApJ* 832 (1), 92.
- Page, D., Reddy, S., 2006. Dense matter in compact stars: theoretical developments and observational constraints. *ARNPS* 56 (1), 327–374.
- Page, D., Lattimer, J.M., Prakash, M., Steiner, A.W., 2004. Minimal cooling of neutron stars: a new paradigm. *ApJS* 155 (2), 623–650.
- Page, D., Geppert, U., Weber, F., 2006. The cooling of compact stars. *NuPhA* 777, 497–530.
- Pappas, G., Apostolatos, T.A., 2014. Effectively universal behavior of rotating neutron stars in general relativity makes them even simpler than their Newtonian counterparts. *PhRvL* 112 (12), 121101.
- Paschalidis, V., Yagi, K., Alvarez-Castillo, D., Blaschke, D.B., Sedrakian, A., 2018. Implications from GW170817 and I-Love-Q relations for relativistic hybrid stars. *PhRvD* 97 (8), 084038.
- Paulucci, L., Horvath, J.E., Benvenuto, O., 2017. Nucleosynthesis in strange star mergers. *IJMPs* 45, 1760042.
- Peng, G.X., Li, A., Lombardo, U., 2008. Deconfinement phase transition in hybrid neutron stars from the Brueckner theory with three-body forces and a quark model with chiral mass scaling. *PhRvC* 77 (6), 065807.
- Perego, A., Rosswog, S., Cabezon, R.M., Korobkin, O., Käppeli, R., Arcones, A., Liebendörfer, M., 2014. Neutrino-driven winds from neutron star merger remnants. *MNRAS* 443 (4), 3134–3156.
- Perego, A., Radice, D., Bernuzzi, S., 2017. AT 2017gfo: an anisotropic and three-component kilonova counterpart of GW170817. *ApJ* 850 (2), L37.
- Piekarewicz, J., Fattoyev, F.J., Horowitz, C.J., 2014. Pulsar glitches: the crust may be enough. *PhRvC* 90 (1), 015803.
- Piro, L., et al., 2019. A long-lived neutron star merger remnant in GW170817: constraints and clues from X-ray observations. *MNRAS* 483 (2), 1912–1921.
- Pizzochero, P.M., Antonelli, M., Haskell, B., Seveso, S., 2017. Constraints on pulsar masses from the maximum observed glitch. *NatAs* 1, 0134.
- Pohl, R., et al., 2010. The size of the proton. *Natur* 466 (7303), 213–216.
- Postnikov, S., Prakash, M., Lattimer, J.M., 2010. Tidal Love numbers of neutron and self-bound quark stars. *PhRvD* 82 (2), 024016.
- Potekhin, A.Y., Fantina, A.F., Chamel, N., Pearson, J.M., Goriely, S., 2013. Analytical representations of unified equations of state for neutron-star matter. *A&A* 560, A48.
- Potekhin, A.Y., Pons, J.A., Page, D., 2015. Neutron stars—cooling and transport. *SSRv* 191 (1–4), 239–291.
- Prakash, M., Lattimer, J.M., Pons, J.A., Steiner, A.W., Reddy, S., 2001. Evolution of a neutron star from its birth to old age. *LNP* 578, 364.
- Radhakrishnan, V., Manchester, R.N., 1969. Detection of a change of state in the pulsar PSR 0833–45. *Natur* 222 (5190), 228–229.
- Radice, D., Perego, A., Hotokezaka, K., Fromm, S.A., Bernuzzi, S., Roberts, L.F., 2018a. Binary neutron star mergers: mass ejection, electromagnetic counterparts, and nucleosynthesis. *ApJ* 869 (2), 130.
- Radice, D., Perego, A., Zappa, F., Bernuzzi, S., 2018b. GW170817: joint constraint on the neutron star equation of state from multimessenger observations. *ApJ* 852 (2), L29.
- Raithel, C.A., Özel, F., Psaltis, D., 2018. Tidal deformability from GW170817 as a direct probe of the neutron star radius. *ApJ* 857 (2), L23.
- Ranea-Sandoval, I.F., Han, S., Orsaria, M.G., Contrera, G.A., Weber, F., Alford, M.G., 2016. Constant-sound-speed parametrization for Nambu-Jona-Lasinio models of quark matter in hybrid stars. *PhRvC* 93 (4), 045812.
- Ray, P.S., et al., 2019. STROBE-X: X-ray timing and spectroscopy on dynamical timescales from microseconds to years. Preprint. arXiv:1903.03035.
- Read, J.S., et al., 2013. Matter effects on binary neutron star waveforms. *PhRvD* 88 (4), 044042.
- Rezzolla, L., Most, E.R., Weih, L.R., 2018. Using gravitational-wave observations and quasi-universal relations to constrain the maximum mass of neutron stars. *ApJ* 852 (2), L25.
- Rhoades, C.E., Ruffini, R., 1974. Maximum mass of a neutron star. *PhRvL* 32 (6), 324–327.
- Rijken, T.A., Schulze, H.J., 2016. Hyperon-hyperon interactions with the Nijmegen ESC08 model. *EPJA* 52, 21.
- Riley, T.E., et al., 2019. A NICER view of PSR J0030+0451: millisecond pulsar parameter estimation. *ApJ* 887 (1), L21.
- Rosswog, S., Liebendörfer, M., Thielemann, F.K., Davies, M.B., Benz, W., Piran, T., 1999. Mass ejection in neutron star mergers. *A&A* 341, 499–526.
- Ruffert, M., Janka, H.T., Takahashi, K., Schaefer, G., 1997. Coalescing neutron stars - a step towards physical models. II. Neutrino emission, neutron tori, and gamma-ray bursts. *A&A* 319, 122–153.
- Ruiz, M., Shapiro, S.L., Tsokaros, A., 2018. GW170817, general relativistic magnetohydrodynamic simulations, and the neutron star maximum mass. *PhRvD* 97 (2), 021501.
- Saito, K., Tsushima, K., Thomas, A.W., 2007. Nucleon and hadron structure changes in the nuclear medium and the impact on observables. *PrPNP* 58 (1), 1–167.
- Sekiguchi, Y., Kiuchi, K., Kyutoku, K., Shibata, M., Taniguchi, K., 2016. Dynamical mass ejection from the merger of asymmetric binary neutron stars: radiation-hydrodynamics study in general relativity. *PhRvD* 93 (12), 124046.
- Shang, X.L., Li, A., Miao, Z.Q., Burgio, G.F., Schulze, H.J., 2020. Nucleon effective mass in hot dense matter. *PhRvC* 101 (6), 065801.
- Shapiro, S.L., Teukolsky, S.A., 1983. Black Holes, White Dwarfs, and Neutron Stars: The Physics of Compact Objects.
- Sharma, B.K., Centelles, M., Viñas, X., Baldo, M., Burgio, G.F., 2015. Unified equation of state for neutron stars on a microscopic basis. *A&A* 584, A103.
- Shen, H., Toki, H., 2000. Quark mean field model for nuclear matter and finite nuclei. *PhRvC* 61 (4), 045205.
- Shen, H., Toki, H., 2002. Study of  $\Lambda$  hypernuclei in the quark mean-field model. *NuPhA* 707 (3), 469–476.
- Shen, H., Toki, H., Oyamatsu, K., Sumiyoshi, K., 1998. Relativistic equation of state of nuclear matter for supernova and neutron star. *NuPhA* 637 (3), 435–450.
- Shen, H., Ji, F., Hu, J., Sumiyoshi, K., 2020. Effects of symmetry energy on the equation of state for simulations of core-collapse supernovae and neutron-star mergers. *ApJ* 891 (2), 148.
- Shibata, M., Fujibayashi, S., Hotokezaka, K., Kiuchi, K., Kyutoku, K., Sekiguchi, Y., Tanaka, M., 2017. Modeling GW170817 based on numerical relativity and its implications. *PhRvD* 96 (12), 123012.
- Shibata, M., Zhou, E., Kiuchi, K., Fujibayashi, S., 2019. Constraint on the maximum mass of neutron stars using GW170817 event. *PhRvD* 100 (2), 023015.
- Shlomo, S., Kolomietz, V.M., Colò, G., 2006. Deducing the nuclear-matter incompressibility coefficient from data on isoscalar compression modes. *EPJA* 30 (1), 23–30.

- Stergioulas, N., 2003. Rotating stars in relativity. *LRR* 6 (1), 3.
- Stergioulas, N., Friedman, J.L., 1995. Comparing models of rapidly rotating relativistic stars constructed by two numerical methods. *ApJ* 444, 306.
- Stone, J.R., Dexheimer, V., Guichon, P.A.M., Thomas, A.W., 2019. Equation of state of hot dense hyperonic matter in the quark-meson-coupling (QMC-A) model. Preprint. arXiv:1906.11100.
- Stone, J., Guichon, P.A.M., Matevosyan, H.H., Thomas, A.W., 2007. Cold uniform matter and neutron stars in the quark meson-coupling model. *NuPhA* 792 (3–4), 341–369.
- Stone, J.R., Guichon, P.A.M., Reinhard, P.G., Thomas, A.W., 2016. Finite nuclei in the quark-meson coupling model. *PhRvL* 116 (9), 092501.
- Tagami, S., Yasutake, N., Fukuda, M., Yahiro, M., 2020. Determination of symmetry energy from experimental and observational constraints; prediction on CREX. Preprint. arXiv:2003.06168.
- Takátsy, J., Kovács, P., 2020. Comment on “Tidal Love numbers of neutron and self-bound quark stars”. *PhRvD* 102 (2), 028501.
- Tanaka, M., et al., 2017. Kilonova from post-merger ejecta as an optical and near-infrared counterpart of GW170817. *PASJ* 69 (6), 102.
- Tews, I., Carlson, J., Gandolfi, S., Reddy, S., 2018. Constraining the speed of sound inside neutron stars with chiral effective field theory interactions and observations. *ApJ* 860 (2), 149.
- Tews, I., Margueron, J., Reddy, S., 2019. Confronting gravitational-wave observations with modern nuclear physics constraints. *EPJA* 55 (6), 97.
- Toki, H., Meyer, U., Faessler, A., Brockmann, R., 1998. Quark mean field model for nucleons in nuclei. *PhRvC* 58 (6), 3749–3752.
- Tolman, R.C., 1939. Static solutions of Einstein's field equations for spheres of fluid. *PhRv* 55 (4), 364–373.
- Tolos, L., Fabbietti, L., 2020. Strangeness in nuclei and neutron stars. *PrPNP* 112, 103770.
- Tonetto, L., Lugones, G., 2020. Discontinuity gravity modes in hybrid stars: assessing the role of rapid and slow phase conversions. *PhRvD* 101 (12), 123029.
- Traversi, S., Char, P., Pagliara, G., 2020. Bayesian inference of dense matter equation of state within relativistic mean field models using astrophysical measurements. *ApJ* 897 (2), 165.
- Tsang, C.Y., Tsang, M.B., Danielewicz, P., Fattoyev, F.J., Lynch, W.G., 2019. Insights on Skyrme parameters from GW170817. *PhLB* 796, 1–5.
- Tsokaros, A., Ruiz, M., Shapiro, S.L., Sun, L., Uryū, K., 2020. Great impostors: extremely compact, merging binary neutron stars in the mass gap posing as binary black holes. *PhRvL* 124 (7), 071101.
- Urbanec, M., Miller, J.C., Stuchlík, Z., 2013. Quadrupole moments of rotating neutron stars and strange stars. *MNRAS* 433 (3), 1903–1909.
- Vermaseren, J.A.M., Larin, S.A., van Ritbergen, T., 1997. The 4-loop quark mass anomalous dimension and the invariant quark mass. *PhLB* 405, 327–333.
- Wanajo, S., Sekiguchi, Y., Nishimura, N., Kiuchi, K., Kyutoku, K., Shibata, M., 2014. Production of all the r-process nuclides in the dynamical ejecta of neutron star mergers. *ApJ* 789 (2), L39.
- Wang, M., Audi, G., Wapstra, A.H., Kondev, F.G., MacCormick, M., Xu, X., Pfeiffer, B., 2012. The Ame2012 atomic mass evaluation. *ChPhC* 36 (12), 003.
- Wang, Q., Shi, C., Yan, Y., Zong, H.-S., 2019. Crossover hadron-quark transition with a modified interpolation method and constraints from tidal deformability of GW170817. Preprint. arXiv:1912.02312.
- Watanabe, G., Pethick, C.J., 2017. Superfluid density of neutrons in the inner crust of neutron stars: new life for pulsar glitch models. *PhRvL* 119 (6), 062701.
- Watts, A.L., et al., 2019. Dense matter with eXTP. *SCPMA* 62 (2), 29503.
- Weber, F., 2005. Strange quark matter and compact stars. *PrPNP* 54 (1), 193–288.
- Wei, J.B., Chen, H., Burgio, G.F., Schulze, H.J., 2017. Rotating hybrid stars with the Dyson-Schwinger quark model. *PhRvD* 96 (4), 043008.
- Wei, J.Y., et al., 2016. The deep and transient universe in the SVOM era: new challenges and opportunities - scientific prospects of the SVOM mission. Preprint. arXiv:1610.06892.
- Wei, W., Irving, B., Salinas, M., Klähn, T., Jaikumar, P., 2019. Camouflage of the phase transition to quark matter in neutron stars. *ApJ* 887 (2), 151.
- Weih, L.R., Hanauske, M., Rezzolla, L., 2020. Postmerger gravitational-wave signatures of phase transitions in binary mergers. *PhRvL* 124 (17), 171103.
- Wiktorowicz, G., Drago, A., Pagliara, G., Popov, S.B., 2017. Strange quark stars in binaries: formation rates, mergers, and explosive phenomena. *ApJ* 846 (2), 163.
- Witten, E., 1984. Cosmic separation of phases. *PhRvD* 30 (2), 272–285.
- Wyrzykowski, Ł., Mandel, I., 2020. Constraining the masses of microlensing black holes and the mass gap with Gaia DR2. *A&A* 636, A20.
- Xia, C., Zhu, Z., Zhou, X., Li, A., 2019a. Sound velocity in dense stellar matter with strangeness and compact stars. Preprint. arXiv:1906.00826.
- Xia, C.-J., Maruyama, T., Yasutake, N., Tatsumi, T., 2019b. Constraining quark-hadron interface tension in the multimessenger era. *PhRvD* 99 (10), 103017.
- Xing, X., Hu, J., Shen, H., 2016. Quark mean field model with pion and gluon corrections. *PhRvC* 94 (4), 044308.
- Xing, X., Hu, J., Shen, H., 2017. Quark mean field model with pion and gluon corrections for  $\Lambda$  and  $\Xi^0$  hypernuclei and neutron stars. *PhRvC* 95 (5), 054310.
- Yagi, K., Yunes, N., 2013a. I-Love-Q relations in neutron stars and their applications to astrophysics, gravitational waves, and fundamental physics. *PhRvD* 88 (2), 023009.
- Yagi, K., Yunes, N., 2013b. I-Love-Q: unexpected universal relations for neutron stars and quark stars. *Sci* 341 (6144), 365–368.
- Yakovlev, D.G., Kaminker, A.D., Gnedin, O.Y., Haensel, P., 2001. Neutrino emission from neutron stars. *PhR* 354 (1–2), 1–155.
- Yakovlev, D.G., Levenfish, K.P., Haensel, P., 2003. Thermal state of transiently accreting neutron stars. *A&A* 407, 265–271.
- Yamamoto, Y., Furumoto, T., Yasutake, N., Rijken, T.A., 2014. Hyperon mixing and universal many-body repulsion in neutron stars. *PhRvC* 90 (4), 045805.
- Yasin, H., Schäfer, S., Arcones, A., Schwenk, A., 2018. Equation of state effects in core-collapse supernovae. Preprint. arXiv:1812.02002.
- Yu, M., Manchester, R.N., Hobbs, G., Johnston, S., Kaspi, V.M., Keith, M., Lyne, A.G., Qiao, G.J., Ravi, V., Sarkissian, J.M., Shannon, R., Xu, R.X., 2013. Detection of 107 glitches in 36 southern pulsars. *MNRAS* 429 (1), 688–724.
- Zdunik, J.L., Haensel, P., 2013. Maximum mass of neutron stars and strange neutron-star cores. *A&A* 551, A61.
- Zhang, Y., Liu, M., Xia, C.-J., Li, Z., Biswal, S.K., 2020. Constraints on the symmetry energy and its associated parameters from nuclei to neutron stars. Preprint. arXiv:2002.10884.
- Zhang, N.-B., Li, B.-A., 2019a. Extracting nuclear symmetry energies at high densities from observations of neutron stars and gravitational waves. *EPJA* 55 (3), 39.
- Zhang, N.-B., Li, B.-A., 2019b. Implications of the mass  $M=[2.17]_{-0.10}^{+0.11} M_{\odot}$  of PSR J0740+6620 on the equation of state of super-dense neutron-rich nuclear matter. *ApJ* 879 (2), 99.
- Zhang, N.-B., Li, B.-A., Xu, J., 2018. Combined constraints on the equation of state of dense neutron-rich matter from terrestrial nuclear experiments and observations of neutron stars. *ApJ* 859 (2), 90.
- Zhao, T., Lattimer, J.M., 2018. Tidal deformabilities and neutron star mergers. *PhRvD* 98 (6), 063020.
- Zhou, E., Tsokaros, A., Rezzolla, L., Xu, R., Uryū, K., 2018a. Uniformly rotating, axisymmetric, and triaxial quark stars in general relativity. *PhRvD* 97 (2), 023013.
- Zhou, E.-P., Zhou, X., Li, A., 2018b. Constraints on interquark interaction parameters with GW170817 in a binary strange star scenario. *PhRvD* 97 (8), 083015.
- Zhou, E., Tsokaros, A., Uryū, K., Xu, R., Shibata, M., 2019. Differentially rotating strange star in general relativity. *PhRvD* 100 (4), 043015.
- Zhou, E.P., Lu, J.G., Tong, H., Xu, R.X., 2014. Two types of glitches in a solid quark star model. *MNRAS* 443 (3), 2705–2710.
- Zhou, X., Tong, H., Zhu, C., Wang, N., 2017. Dependence of pulsar death line on the equation of state. *MNRAS* 472 (2), 2403–2409.
- Zhou, Y., Chen, L.-W., 2019. Ruling out the supersoft high-density symmetry energy from the discovery of PSR J0740+6620 with mass  $2.14_{-0.09}^{+0.10} M_{\odot}$ . *ApJ* 886 (1), 52.
- Zhu, Z.-Y., Li, A., 2018. Effects of the nucleon radius on neutron stars in a quark mean field model. *PhRvC* 97 (3), 035805.
- Zhu, Z.-Y., Li, A., Hu, J.-N., Sagawa, H., 2016.  $\Delta$  (1232) effects in density-dependent relativistic Hartree-Fock theory and neutron stars. *PhRvC* 94 (4), 045803.
- Zhu, Z.-Y., Zhou, E.-P., Li, A., 2018. Neutron star equation of state from the quark level in light of GW170817. *ApJ* 862 (2), 98.
- Zhu, Z.-Y., Li, A., Hu, J.-N., Shen, H., 2019. Quark mean-field model for nuclear matter with or without bag. *PhRvC* 99 (2), 025804.
- Zimmerman, J., Carson, Z., Schumacher, K., Steiner, A.W., Yagi, K., 2020. Measuring nuclear matter parameters with NICER and LIGO/Virgo. Preprint. arXiv:2002.03210.
- Zuo, W., Li, A., Li, Z.H., Lombardo, U., 2004. Nuclear three-body force effect on a kaon condensate in neutron star matter. *PhRvC* 70 (5), 055802.